Ab initio modeling of primary processes in photosynthesis : protein induced activation of bacteriochlorophylls for efficient light harvesting and charge separation

Wawrzyniak, P.K.

Ab initio modeling of primary processes in photosynthesis

Protein induced activation of bacteriochlorophylls for efficient light harvesting and charge separation

Piotr K. Wawrzyniak

Piotr K. Wawrzyniak
Ab initio modeling of primary processes in photosynthesis: Protein induced activation of bacteriochlorophylls for efficient light harvesting and charge separation
Ph.D. Thesis, Leiden University, 26th January 2011

ISBN 978-90-816603-1-0 (Print)
ISBN 978-90-816603-2-7 (PDF)

Printing and cover design by Smart Printing Solutions, www.sps-print.eu

Ab initio modeling of primary processes in photosynthesis

Protein induced activation of bacteriochlorophylls for efficient light harvesting and charge separation

PROEFSCHRIFT

ter verkrijging van
de graad van Doctor aan de Universiteit Leiden,
op gezag van Rector Magnificus Prof. Mr. P.F. van der Heijden,
volgens besluit van het College voor Promoties
te verdedigen op woensdag 26 januari 2011
klokke 13.45 uur

door

Piotr K. Wawrzyniak

geboren te Wałbrzych, Polen
in 1980

Promotiecommissie

Promotor:
Prof. dr. Huub de Groot

Copromotor:
Dr. Francesco Buda

Overige leden:
Prof. dr. Jaap Brouwer
Prof. dr. Marc van Hemert
Prof. dr. Rienk van Grondelle
Dr. Johannes Neugebauer

This work was supported by the Netherlandse Organisatie voor Wetenschappelijk Onderzoek (NWO) through a TOP Grant on 'Ultrahigh field solid-state NMR of photosynthesis and artificial photosynthetic energy conversion systems'.

The use of supercomputer facilities was sponsored by the Stichting Nationale Computerfaciliteiten (NCF), with financial support from the Netherlandse Organisatie voor Wetenschappelijk Onderzoek.

For Marzena and Julia

Contents

List of Abbreviations **vii**

Notation **ix**

Preface **1**

1 Introduction **3**
1.1 Photosynthesis 3
1.2 Histidine 4
1.3 The Light-Harvesting Complex II of *Rps. acidophila* 8
1.4 Bacterial Reaction Center of *Rb. sphaeroides* 11
1.5 Scope of the Thesis 15

2 Theoretical Methods **17**
2.1 Introduction 17
2.2 Born-Oppenheimer Approximation 17
2.3 Density Functional Theory 19
2.4 Basis Set Approximation 22
2.5 Exchange-Correlation Functionals 23
2.6 Time-dependent Density Functional Theory 24
2.7 Chemical Models 26

3 Protein-induced Effects in BChl *a*–His Complexes of LH2 **27**
3.1 Introduction 27
3.2 Models and Methods 28
3.3 Results and Discussion 30

3.3.1 Chemical shifts calculations for histidine in vacuum . . 30
3.3.2 Protonation state of histidines in the LH2 complex . . . 34
3.4 Conclusions . . . 40

4 Electronic Structure of His in Bacterial Reaction Center 41
4.1 Introduction . . . 41
4.2 Models and Methods . . . 42
4.3 Results and Discussion . . . 44
4.3.1 Axial histidines . . . 46
4.3.2 Non-axial histidines . . . 49
4.4 Conclusions . . . 51

5 Origin of Asymmetry in Bacterial Reaction Center 53
5.1 Introduction . . . 53
5.2 Models and Methods . . . 55
5.3 Results and Discussion . . . 57
5.3.1 Asymmetry of the special pair . . . 57
5.3.2 Absorption properties . . . 63
5.4 Conclusions . . . 69

6 General Discussion and Future Prospects 71

Appendix A Basis Set and Functional Tests 75

Summaries 79
Summary . . . 79
Samenvatting . . . 81
Streszczenie . . . 84

Curriculum Vitae 89

List of Publications 91

Afterword 95

Bibliography 99

List of Abbreviations

2D	Two-dimensional
ADF	Amsterdam Density Functional program
axial His	Histidine coordinated to Mg^{2+} ion of bacteriochlorophyll *a*
anionic His	Histidine with N_π and N_τ atoms deprotonated
B	Accessory bacteriochlorophyll *a*
B3LYP	Becke 3-Parameter, Lee–Yang–Parr exchange-correlation functional
B800	BChl *a* system in LH2 absorbing at wavelength of 800 nm
B850	BChl *a* system in LH2 absorbing at wavelength of 850 nm
BChl *a*	Bacteriochlorophyll *a*
BChl *a*–His	Bacteriochlorophyll *a*-histidine complex
BLYP	Becke–Lee–Yang–Parr exchange-correlation functional
(B)RC	(Bacterial) Reaction Center
C	Carotenoid
cationic His	Histidine with N_π and N_τ atoms protonated
CIDNP	Chemically Induced Dynamic Nuclear Polarization
CT	Charge Transfer
DFT	Density Funcional Theory
ENDOR	Electron–Nuclear DOuble Resonance
EPR	Electron paramagnetic resonance
φ	Bacteriopheophytin *a*
FT	Fourier Transform
GGA	Generalized Gradient Approximation
GIAO	Gauge-Independent Atomic Orbital
GTF	Gaussian-type Function

H	HOMO
His	Histidine
KS	Kohn-Sham
L	LUMO
LDA	Local Density Approximation
LH1	Light-Harvesting complex I (antenna complex)
LH2	Light-Harvesting complex II (antenna complex)
MeIm	Methylimidazole
neutral$_\tau$ His	Histidine with protonated N_τ and deprotonated N_π
neutral$_\pi$ His	Histidine with protonated N_π and deprotonated N_τ
NICS	Nucleus Independent Chemical Shift
NMR	Nuclear Magnetic Resonance
P	Special Pair
PCET	Proton-Coupled Electron Transfer
PDB	Protein Data Bank
PES	Potential Energy Surface
ppm	parts per million
Q	Ubiquinone-10
QH_2	Ubiquinol
QM/MM	Quantum Mechanics/Molecular Mechanics
Rb.	*Rhodobacter*
RMSD	Root Mean Square Displacement
Rps.	*Rhodopseudomonas*
SOAP	Statistical Averaging of Orbital Potentials potential
SSNMR	Solid-state NMR
STF	Slater-type Function
TMS	Tetramethylsilane
TZP	Triple-Zeta basis set with one set of Polarization functions

Notation

$\widehat{\mathrm{A}}$	Operator A
χ,χ_s	Response function
χ_μ	Basis set function
χ_p	Primitive basis function
δ	Chemical shift [ppm], Chemical Shift Tensor Anisotropy [kHz]
Δ	Laplacian
∇	Nabla
ε_0	Permittivity of vacuum
$\epsilon_{xc}^{uniform}$	Exchange-correlation energy per electron of uniform electron gas
η	Chemical Shift Tensor Asymmetry
e	Electron charge, exponent
E	Energy
$\hbar = \frac{h}{2\pi}$	Planck constant
$\widehat{\mathrm{H}}$	Hamiltonian
J	Coulomb electron–electron repulsion
m	Electron mass
M	Nuclear mass
n	When used in a sum indicates the number of electrons
N	When used in a sum indicates the number of nuclei
ϕ	Kohn-Sham orbital
Ψ	Wavefunction of a system

Q_x	Less intense absorption band of BChl *a* in the region of 550–600 nm
Q_y	Intense absorption band of BChl *a* in the region of 750–800 nm
ρ	Electron density
r	Distance
$\mathbf{r}$	Position of the all electrons, vector position is space
$\mathbf{r_i}$	Position of electron i
r_{ij}	Distance between electrons i and j
$\mathbf{R}$	Position of the all nuclei
$\mathbf{R_I}$	Position of nucleus I
R_{IJ}	Distance between nuclei I and J
t	Time
T	Kinetic energy
υ	Potential
V	Potential energy
Y	Spherical harmonic function
Z	Atomic number

Preface

Everything started in 1780 [1] when Joseph Priestley, an English chemist, enclosed a mint plant and a burning candle in a glass jar. Surprisingly, the candle burned without interruption, even though in earlier experiments it was extinguished quickly when no plant was present in the jar. After several more tests he concluded that plants could "restore air which has been injured by the burning of candles" and that "the air would neither extinguish a candle, nor was it all inconvenient to a mouse which I put into it". His experiments reached a Dutch physician Jan Ingenhousz who then spent a summer near London performing over 500 experiments. He found that only green parts of a plant and only under the sunlight can "correct the bad air" and they make it in a matter of a few hours. Very soon after Jean Senebier, a Swiss pastor and botanist working in Geneva, demonstrated that carbon dioxide is taken up during photosynthesis and a Swiss chemist, Nicolas-Théodore de Saussure, discovered that the other necessary reactant is water. Finally, a German surgeon Julius Robert Mayer completed the basic equation of photosynthesis with the statement that plants convert elusive solar energy into a more rigid form — the chemical energy. It then became evident that in the course of photosynthesis carbon dioxide and water are converted with the use of solar light into glucose and a waste product, oxygen. The "waste" we are highly dependent on...

$$6CO_2 + 6H_2O \xrightarrow{h\nu} C_6H_{12}O_6 + 6O_2$$

Chapter 1

Introduction

1.1 Photosynthesis

Photosynthesis on Earth can be traced 3.5 billion years back in time when algae species developed a photosynthetic apparatus similar to present plant photosystems. [2, 3] Since then, all the food, oxygen for respiration and energy produced through the molecular respiration, are directly or indirectly related to the photosynthetic activities. It is believed that phototrophic organisms converted the composition of Earth's atmosphere over the history of our planet from the anoxic state to the oxic state by production of oxygen. However, only plants, algae and cyanobacteria are capable of performing oxygenic photosynthesis. [4] The other types of photosynthetic bacteria, *i.e.* purple sulphur bacteria, purple non-sulphur bacteria, green sulphur bacteria, green non-sulphur bacteria and heliobacteria, are not able to oxidize water and thus do not produce oxygen. [5] Instead, they use reduced sulphur compounds, molecular hydrogen or simple organic molecules as an electron donor to obtain reductive power. There are two essential steps in photosynthesis: absorption of light and conversion of excitation energy into chemical energy for convenient energy storage. The course of events in photosynthesis starts with an absorption of a photon by one of the pigment molecules in the photosynthetic membrane. Then the excitation is transferred through an array of antenna pigments, otherwise known as light-harvesting complexes,

to the reaction center, which acts as a photochemical trap to convert the excitations into chemical energy. Before the components of the photosynthetic apparatus will be discussed in more details, an overview of histidine protonation states will be presented, as this aminoacid occupies crucial positions in photosynthetic complexes.

1.2 Histidine

Histidine is one of the 20 naturally occurring amino acids and plays an important role in many biochemical processes. Histidine can act as a catalyst in the active site of enzymes [6] and as a ligand to metals. [7–12] It can undergo tautomeric changes and is able to form hydrogen bonds, acting both as a proton donor and acceptor, and thus playing the role of a mediator in proton transfer processes in various proteins. [13, 14] Four different protonation forms of the imidazole ring are possible: a formally anionic imidazolate form, denoted as anionic in this thesis, two neutral tautomers and a doubly protonated imidazolium form, named cationic here. The neutral tautomers will be denoted throughout this dissertation as neutral$_\pi$ and neutral$_\tau$, with N_π or N_τ protonated respectively (see Figure 1.1). In the literature N_π is sometimes

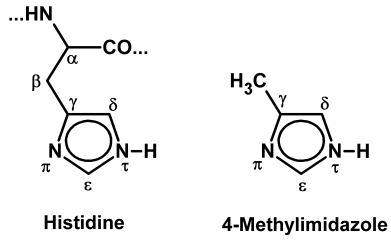

Figure 1.1: The neutral$_\tau$ form of histidine and 4-methylimidazole with the atom labeling used throughout the thesis.

referred to as N^δ or N_3 and N_τ is indicated as N^ε or N_1. The neutral$_\tau$ histidine is the most frequently found in nature, especially in proteins and smaller compounds. [15–20] The other neutral tautomer is difficult to crystallize and we are aware of only one crystalline sample of glutaric acid–histidine complex where it has been observed. [21] Moreover, it is only occasionally found

in proteins where it is stabilized by a hydrogen bond and is believed to be reserved for special tasks. [22–24] These two tautomers can be distinguished in a NMR spectrum by their C_δ chemical shifts. [25] Specifically, values of C_δ chemical shift above 122 ppm were assigned to the neutral$_\pi$ tautomer, while values below 122 ppm indicate the presence of the neutral$_\tau$. The two nitrogens in the neutral tautomers have substantially different character. The pyrrole-type nitrogen, denoted often as >N–H, gives experimentally a NMR resonance at 170 ppm and its chemical shift anisotropy in histidine is estimated to be $\delta \approx 4.5$ kHz with $\eta \approx 1$. [18, 26, 27] In contrast, the pyridine-type nitrogen, denoted usually as $\geqslant$N|, gives a NMR signal around 250 ppm, with anisotropy parameters δ and η of about 8.7 kHz and 0.4, respectively. [18, 26, 27]

The existence of the two neutral tautomeric forms is described by the equilibrium constant, which for different imidazoles depends on the nature of the ring substituent group [28] and equals 1 for imidazole itself. Since for the imidazole (no ring substituents) both nitrogen atoms are chemically equivalent and the tautomeric exchange is fast in aqueous solution, only one average signal is observed for ^{15}N NMR [23], while two resonances separated by 72 ppm are reported for polycrystalline imidazole, suggesting that the tautomeric exchange is very slow or not existing in a crystal phase. [29] The NMR signal in solution is observed to shift upfield with decreasing pH, producing a smooth titrating curve and thus indicating that the ionic equilibrium is also fast on the NMR time scale.

For histidine in solution, due to the presence of α-amino group ionization and due to the fact that the ring nitrogens are not equivalent, the situation is more complex. Therefore, five possible species must be considered, as depicted in Fig. 1.2. At low pH only the positively charged form I is present and the π and τ nitrogens give signals separated by 2.4 ppm. [30] With increasing the pH a deprotonation of the imidazole ring of histidine occurs and the neutral forms IIa and IIb are produced, but until pH 8.0 is reached all the three species yield an averaged ^{15}N chemical shift due to rapid chemical exchange. At pH 8.0 the cationic form is not present anymore. At this point, the N_π signal is shifted downfield by 56 ppm when compared to the positively charged histidine, while N_τ is shifted only by 5 ppm, indicating that the de-

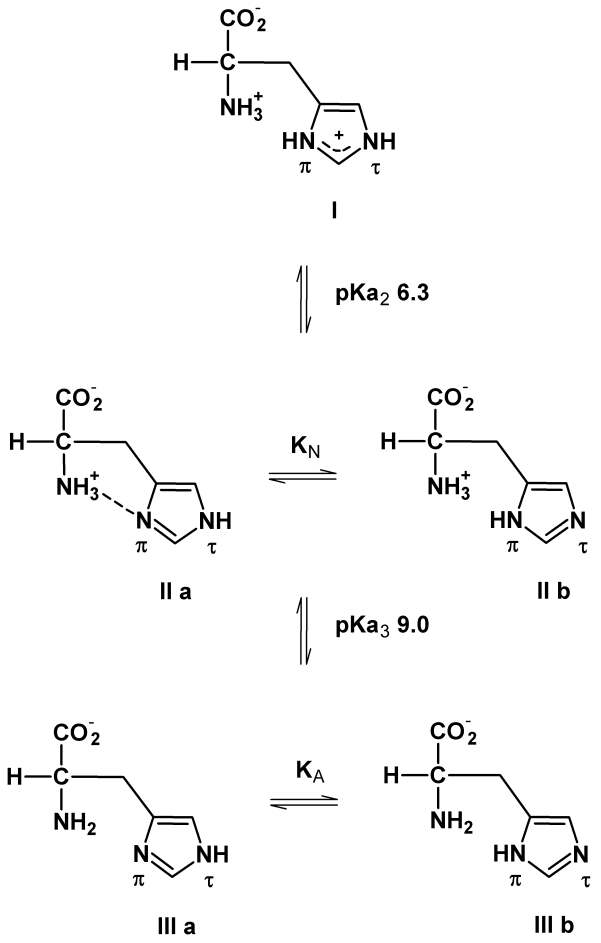

Figure 1.2: Possible ionic and tautomeric forms of histidine from pH 2 to 12.5. Redrawn from [29].

protonation occurs mainly at the π position. To support this observation, the molar fraction of IIa was estimated, resulting in a value of 0.88, and thus confirming that this tautomer exists in a predominant quantity. Nevertheless, a significant amount of the other tautomer is present, giving rise to average ^{15}N chemical shift values. The reason that the IIa form is predominant may be, at least partially, attributed to a hydrogen bond between unprotonated N_π and the α-amino group, which cannot be formed in the tautomer IIb due to steric hindrance. [31] Further deprotonation, occurring at the amino group, removes the possibility for hydrogen bond formation, resulting in a redistribution of the tautomers: the N_π peak shifts upfield by 15 ppm and the N_τ peak shifts downfield by the same amount. Now the IIIa form is not so strongly favored over IIIb as for the neutral form, however the calculated molar fraction (0.76) indicates that the tautomer with the proton attached to N_τ is still the predominant one.

According to solid-state studies [29], in samples lyophilized at low pH, the N_π and N_τ signals are very close to the corresponding cationic chemical shifts in solution. When the pH increases to 8.4 the positively charged histidine is replaced by a neutral one, however, contrary to the liquid studies a separate resonance for each species is observed because the exchange between the cationic and neutral forms is very slow. In addition, only the neutral$_\tau$ tautomer is present, as revealed by 11 ppm downfield shift compared to the N_π response in solution and 5 ppm upfield shift of the N_τ signal. The midpoint for that transition was calculated to occur at pH 6.3. Further increase of the pH leads to a negatively charged form and the conversion is complete at pH 12.3. The midpoint of this transition occurs around pH 9.5 and the deprotonation results in a 6 ppm downfield shift of the π resonance with little change of the τ frequency. This is an evidence that the neutral$_\tau$ tautomer is still the only one observed, even though the stabilization provided by the hydrogen bond in the neutral form is now absent due to the deprotonation of the α-amino group.

Since histidine activity depends on the nitrogen atoms in the imidazole ring, many biochemical mechanisms may be understood only if histidine protonation states can be established. However, many histidine protonation states

reported in Protein Data Bank structures are still tentative. [32] In principle such information can be obtained from NMR studies. [22, 25, 33–35] The problem is that even if NMR spectra are available, a precise assignment of the spectral lines to a specific residue is often difficult. Quantum chemical calculations can then provide a complementary tool to assist in assigning the NMR spectra.

1.3 The Light-Harvesting Complex II of *Rhodopseudomonas acidophila*

Light-harvesting complexes absorb photons and transport the excitation energy through LH1 complexes to photosynthetic reaction centers, where a series of electron transfer reactions across the membrane leads to charge separation. In this way, LH2 complexes accomplish the first step of photosynthesis, *i.e.* the absorption of light. The optical absorption happens much faster and over a much larger area, compared to the charge separation in the RC, which is a relatively slow and local process. The structure of LH2 from *Rhodopseudomonas acidophila* has been described in detail before. [36–38] Experimentally [36], it has been found that this antenna system possesses a 9-fold symmetry, as depicted in Fig. 1.3. It contains a ring of 9 bacteriochlorophyll *a* molecules constituting the B800 system, named after its characteristic absorption at 800 nm. In addition another 18 BChl *a* molecules are arranged in pairs of α and β molecules with partial macrocycle overlap, which form the B850 ring system. The planes of the B800 macrocycles are aligned parallel to the membrane, while the macrocycle planes of the BChls *a* in the B850 ring are perpendicular to the membrane. [36] The distance between two Mg atoms in B800 is 20.8–21.1 Å, while it is 9.2–9.4 Å within an (α,β)-B850 dimer and 8.8–9.0 Å between two following B850 dimers.

In the LH2 complex, helical protein subunits form two concentric cylinders, an inner ring of α-protein subunits and an outer ring of β-protein subunits. An α-subunit monomer consists of 53 residues and the β-subunit monomer consists of 41 residues. The magnesium atoms of each B850 (α,β)-BChl *a* dimer ligate N_τ atoms from α-His 31 or β-His 30 residues, respec-

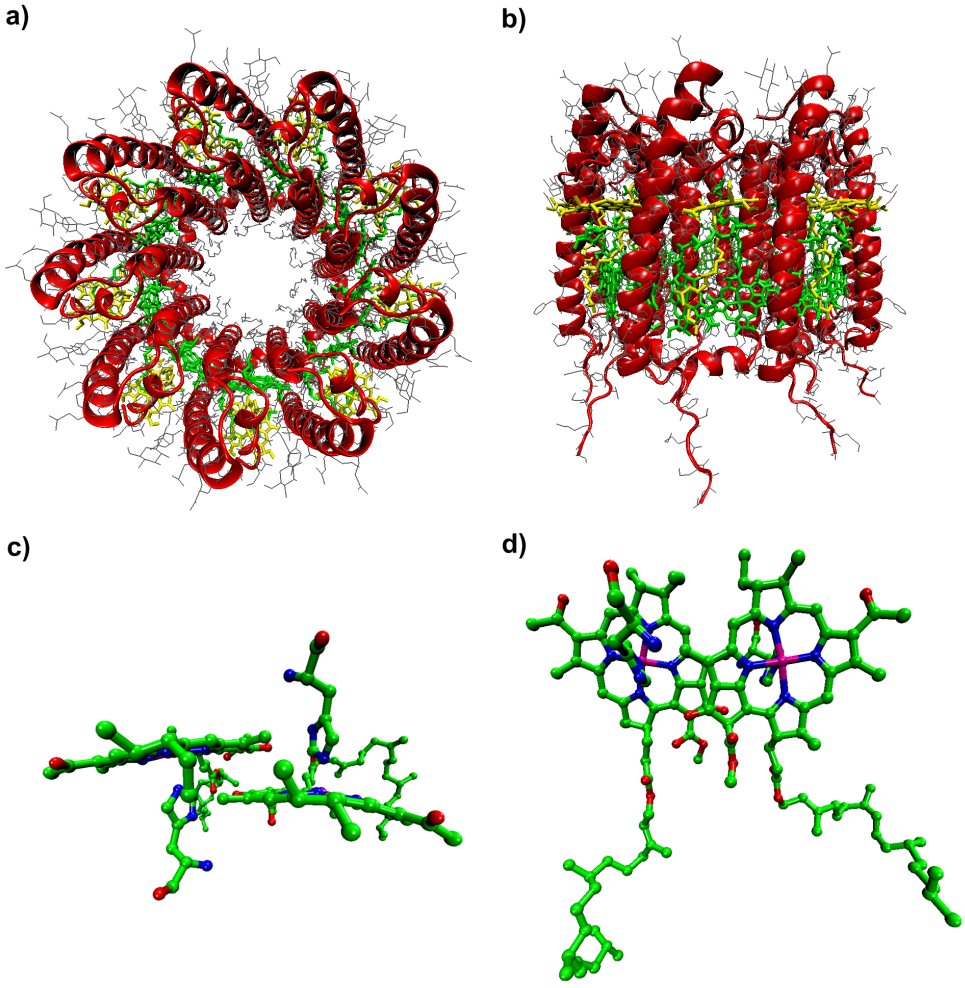

Figure 1.3: a) Top view and b) side view of LH2 complex from the 2FKW crystal structure of *Rps. acidophila*. [36] The B850 and B800 BChl *a* are shown in green and in yellow, respectively. c) Top view and d) side view of a B850 dimer and coordinated histidines.

tively. [26, 39] The α and β histidines alternate when moving along the ring of B850. Three other histidines, α-His 37, β-His 12 and β-His 41, are not coordinated to BChls. A complete assignment of the histidine residues in the LH2 complex of *Rps. acidophila* has been recently obtained by solid-state NMR. [26, 39] It was found that the five histidines in the LH2 complex can be classified in two types. The first type, including α-His 37 and β-His 12, has chemical shifts corresponding to neutral$_\tau$ histidines, while the α-His 31, β-His 30 and β-His 41 have been classified as positively charged histidines and all three display identical ^{13}C chemical shifts. [26, 39] However, while the β-His 41 has both nitrogens in the ring protonated, the α-His 31 and β-His 30 are coordinated by the N_τ nitrogen to the Mg^{2+} ion of the bacteriochlorophyll *a* molecules. Therefore, the residues α-His 31 and β-His 30 are formally neutral$_\pi$ tautomers, which is consistent with the experimentally measured anisotropy parameters for N_τ, indicating a pyridine-like chemical character of this atom. [26, 39] Other metal-coordinated histidines maintain their neutral character and show chemical shifts similar to the uncoordinated neutral histidines. [40] Thus, the experimental observation of ^{13}C chemical shifts for the Mg-coordinated histidines that are very similar to the shifts for the cationic β-His 41 [26, 39] is surprising and in contrast with the anisotropy parameters δ and η.

The two BChl *a*-coordinated histidines stabilize the B850 ring assembly and mediate the coupling between the ring components, playing not only structurally but also electronically an important role. [41] The ring itself acts, through the overlapping assembly, as an energy storage system that preserves excitation energy until it is forwarded to other rings and ultimately to the RC. [42, 43] For the B800, the excitations are localized on one BChl *a* before jumping to the next one, while the B850 system is strongly exciton-coupled and excitations are effectively delocalized over the entire B850 ring. [44, 45] Since, the exact mechanism of the energy storage and the color shift is not yet fully elucidated, knowledge of the electronic structure of the BChl *a*–His complex can be important for understanding the exciton transfer process over the LH2 B850 ring.

1.4 Bacterial Reaction Center of *Rhodobacter sphaeroides*

The primary photosynthetic energy conversion occurs in pigment–protein complexes known as reaction centers. Two types of RCs are known. [46, 47] Type-I possesses iron–sulphur clusters as terminal electron acceptors, while in type-II this function is performed by quinones. All the anoxygenic photosynthetic organisms contain either type-I RCs, in green sulphur bacteria and heliobacteria, or type-II RCs in purple bacteria and green non-sulphur bacteria. In contrast, in oxygenic organisms both types are present and work in series: the type-I RC or Photosystem I reduces carbon dioxide via the Calvin cycle, while the type-II RC, Photosystem II, is involved in oxidization of water.

The reaction center of *Rb. sphaeroides*, belonging to the class of type-II RCs, is surrounded by light-harvesting complexes LH1 and LH2. Together they form the photosynthetic unit located in vesicles of the cytoplasmic membrane. The RCs consist of three single polypeptide chains, forming L, M and H subunits. [48–50] The first two subunits consist of 281 and 307 aminoacids, respectively. They exhibit mainly α-helical structure and both have five long hydrophobic α-helices that span the bacterial membrane. The H chain, formed by 260 residues, is more globular in shape and is almost entirely positioned in the cytoplasmic region with only one transmembrane helix. Apart from the three polypeptide chains, ten non-covalently bound prosthetic groups, usually referred to as cofactors, are present: Four bacteriochlorophylls *a*, two bacteriopheophytins *a* and two ubiquinones-10 form two branches **A** and **B** with a non-heme iron ion (Fe^{2+}) in between, while the tenth cofactor, the carotenoid spheroidene, is located on the side of branch **B** (Fig. 1.4). The structures of cofactors directly involved in the electron transfer are presented in Fig. 1.5.

Two of the four bacteriochlorophylls *a* (P_L from the **A** branch and P_M from the **B** branch) have mutual overlap with their pyrrole ring *I* (see Fig. 1.5) with a minimum intermolecular distance of approximately 3.3 Å, and they connect the two cofactor branches. [50] Since they are electronically coupled and the primary electron transfer originates from these two species, they are

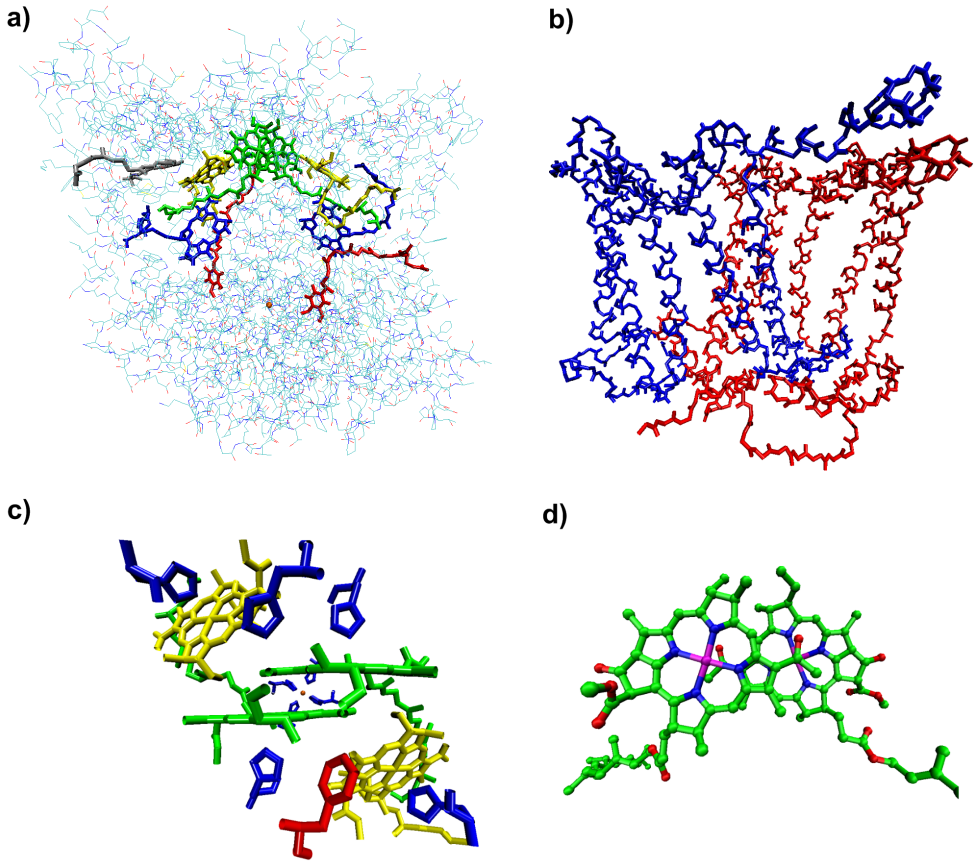

Figure 1.4: a) Structure of the bacterial reaction center and arrangement of cofactors in the 1PCR crystal structure of *Rb. sphaeroides* [49]: *P* (green), *B* (yellow), φ (blue), *Q* (red), *Fe* (orange) and *C* (grey). The active branch is on the right side. b) Symmetry of L (blue) and M (red) protein backbones. c) Overview of the special pair: P (green), histidines (blue) and phenylalanine (red). d) Structure and overlap of the special pair.

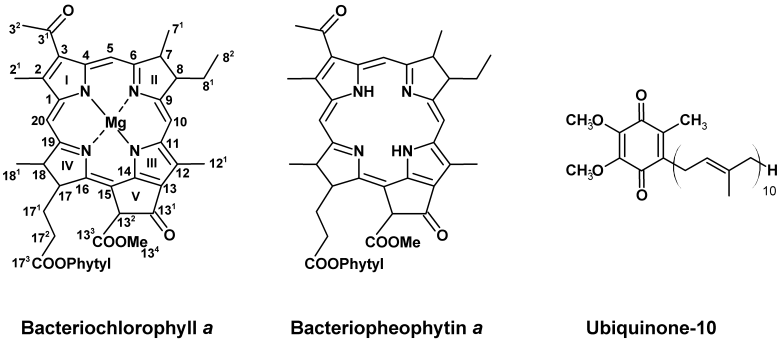

Figure 1.5: Structure of cofactors directly involved in electron transfer. The left panel shows the IUPAC numbering of carbon atoms for the BChl *a* which is used throughout the thesis.

usually called the 'Special Pair'. A monomeric accessory BChl *a* molecule is located on either side of the special pair and two bacteriopheophytin *a* species reside about 18 Å away from P (Fig. 1.4). The magnesium atoms of P_L and P_M ligate His L173 and His M202, respectively. Two other histidine residues, His L153 and His M182, coordinate to the two accessory bacteriochlorophylls *a*. These histidines are within about the same distance (2.68 ± 0.07 Å) from the corresponding BChl *a* and should experience similar ring current shifts. The ring current shift is a change of the nuclear resonance frequency due to the field-induced circulation of delocalized π electrons in proximity. Interestingly, the two histidines interacting with the special pair are within hydrogen-bonding distance to a water molecule with their N_π atoms. [50] In addition, His L168 is located at hydrogen-bonding distance from the acetyl bonded to the P_L C3 atom, while the symmetrical position for the P_M is occupied by Phe M197. Contrary to LH2, protonation states of these and remaining histidines of the BRC have not yet been clearly established.

The two cofactor branches, together with polypeptide backbones of protein subunits L and M, display a nearly perfect local two-fold symmetry (Fig. 1.4), with the symmetry axis oriented perpendicular to the membrane plane. [2] Also the overlap of the special pair appears to be rather symmetric. Despite this structural symmetry, the functioning of the reaction center is asymmet-

ric and in the wild type bacteria electron transfer takes place through the "active branch" **A**. [51] It is not known if and how the protein initiates the charge transfer across the active branch. In the primary electron transfer event, the special pair is excited by the energy transferred from the light-harvesting complexes. Within 3 ps an electron is transferred from the first excited singlet state of P to φ_A forming the radical pair $P^{+\bullet}\varphi_A^{-\bullet}$. [2,52] There is converging and convincing evidence that the accessory B_A is an intermediate of this process. [2,3,53–57] In the next step, the electron is transferred down a chain of acceptor molecules to Q_A and subsequently to Q_B of the **B** branch, reducing it once. These secondary electron transfers are considerably slower, with reported kinetics of 200 ps and 100 μs for the two steps, respectively. [3] As a consequence of those primary and secondary electron transfers, a long-lived, spatially well-separated radical pair is formed. Meanwhile, after about 1 μs, the oxidized primary electron donor $P^{+\bullet}$ is reduced by an electron from cytochrome c located at the periplasmic side of the protein. It takes an additional electron and two protons to create ubiquinol QH_2, which leaves the RC and is replaced by ubiquinone-10 from the quinone pool in the organism. [58] QH_2 is used to facilitate the creation of a proton gradient across the membrane that drives the synthesis of the energy-rich ATP. [59]

This strong contrast between symmetry in structure and asymmetry in function has triggered investigations in the direction of electron transfer for many years [2,3] and a considerable amount of studies have focused on the special pair. [53,60–66] It has been proposed from Stark experiments that the excited state P* is electronically asymmetric and more electron density is concentrated on P_M. [63] For the cation radical $P^{+\bullet}$, EPR and ENDOR studies have shown a disproportion in spin density distribution in favor of P_L. [64,67,68] It has been also reported that the two bacteriochlorophylls *a* of the special pair have different electronic structure already in the ground state and that excess negative charge is located on P_L. [53,65,66,69–71] Therefore, the functional asymmetry in the RC is introduced in the dark ground state, although the origin of the symmetry breaking remains unclear.

1.5 Scope of the Thesis

Although the structure and the kinetics of the electron transfer in bacterial reaction centers are known, how the functional asymmetry in this protein triggers the charge separation may be considered one of the central questions for the conversion of solar energy into chemical energy in photosynthetic organisms. With a detailed understanding of the origin for the special pair symmetry breaking and its influence on the electron transfer, it would be possible to gain an insight into the generic mechanism underpinning the principles of an efficient charge separation process. This may prove beneficial for the development of artificial photosynthetic devices, which would not only offer a great potential for solving the global energy problem but also would assist in mitigating climate change.

Specifically, the immediate protein environment of the special pair, particularly histidine residues, may perturb the electronic structure of P_L and P_M in the ground and excited states, facilitating thereby the electron transfer along the **A** branch. Since histidine activity depends on the nitrogen atoms in the imidazole ring, it is crucial to know the protonation states of the imidazole side chains. However, presently no detailed knowledge of histidine protonation states in bacterial reaction centers exists and X-ray crystallography cannot provide a clear answer about the specific protonation state of residues such as His. [32] NMR, combined with quantum mechanical calculations, provides a complementary method in structure determination and structure-function studies for the histidines.

As discussed in the previous sections, Mg-coordinated histidines in the LH2 complex are not only structurally but also electronically important for stabilization and coupling between the B850 bacteriochlorophylls *a*. Therefore, a detailed knowledge of the electronic structure of the BChl *a*–His complex is essential to understand the exact mechanism of energy storage and exciton transfer over the B850 ring. Recent experimental data reveal a rather unusual behavior for those histidines. [26,39] Despite their formal neutral$_\pi$ form, they surprisingly exhibit chemical shifts identical to the doubly protonated histidines. This issue can be addressed only by means of quantum mechanical calculations.

The specific aim of this thesis is to investigate interactions between histidine and bacteriochlorophylls *a* in LH2 and BRC systems, and address the open questions posed by experimental data as to the nature of BChl *a*–His complexes and asymmetry of special pair. The theoretical work presented here describes the study of photosynthetic processes in purple non-sulphur bacteria *Rhodobacter sphaeroides* and *Rhodopseudomonas acidophila* and is closely related to recent experimental work in the field of photosynthesis.

In chapter **2**, a general overview of theoretical methods and approximations used in this work is presented. Chapter **3** describes accuracy assessments for DFT-computed chemical shifts and presents the chemical shift characterization of neutral$_\pi$ histidine, for which a very limited set of data exists. Next, protonation states of uncoordinated histidines are discussed, and finally the BChl *a*–His complex in the LH2 protein is addressed with its peculiar properties. It is established that Mg-coordinated histidines are in a protein-induced frustrated state due to steric and electrostatic stress exerted by the LH2 protein environment. In chapter **4** an assignment of histidine protonation states in the reaction center is presented, both for axial and non-axial histidines. It is found that one of the four Mg-coordinated histidines has a substantially different electronic structure compared to the other three, possibly contributing to the differences between P_L and P_M in the ground and excited state. A more detailed discussion on asymmetry of the special pair is presented in chapter **5**, where an extended model including explicitly the special pair and the closest residues is studied with DFT. It is proposed that the asymmetry of the special pair is an intrinsic property of the bacteriochlorophyll *a* dimer resulting from a particular orientation of the P_L 3^1 acetyl group. This orientation is forced by the hydrogen bond from His L168 and by inducing conformational changes to the acetyl the biophysical properties of the special pair can be tuned. Finally, chapter **6** provides a general discussion and presents some future prospects.

Chapter 2

Theoretical Methods

2.1 Introduction

This chapter provides a short description of theoretical approximations and methods used in this work. First, the Born-Oppenheimer approximation will be reviewed, followed by a brief overview of Density Functional Theory. Next, the basis set approximation will be discussed together with Pople's notation, followed by a discussion on the exchange-correlation functionals. Finally, the perturbative derivative of DFT, the time-dependent DFT, will be presented.

2.2 Born-Oppenheimer Approximation

The time-dependent Schrödinger Equation

$$\widehat{\mathrm{H}}\Psi(\mathbf{r},\mathbf{R},t) = i\hbar\frac{\partial\Psi(\mathbf{r},\mathbf{R},t)}{\partial t} \tag{2.1}$$

is a non-relativistic description of the system and it is valid when particle velocities are small compared to the speed of light. Since $\widehat{\mathrm{H}}$ does not depend on time the equation 2.1 can be simplified to the time-independent Schrödinger Equation:

$$\widehat{\mathrm{H}}\Psi(\mathbf{r},\mathbf{R}) = E\Psi(\mathbf{r},\mathbf{R}) \tag{2.2}$$

Following the Born interpretation of the wavefunction, Ψ has to be normalized:

$$\langle \Psi | \Psi \rangle = 1 \tag{2.3}$$

The Hamiltonian consists of kinetic and potential energy terms:

$$\widehat{\mathrm{H}} = \widehat{\mathrm{T}}_n(\mathbf{R}) + \widehat{\mathrm{T}}_e(\mathbf{r}) + \widehat{\mathrm{V}}_{n-n}(\mathbf{R}) + \widehat{\mathrm{V}}_{e-e}(\mathbf{r}) + \widehat{\mathrm{V}}_{e-n}(\mathbf{r}, \mathbf{R}) \tag{2.4}$$

The kinetic energy operators for nuclei and electrons are written as

$$\widehat{\mathrm{T}}_n = -\frac{\hbar^2}{2} \sum_I^N \frac{1}{M_I} \left(\frac{\partial^2}{\partial x_I^2} + \frac{\partial^2}{\partial y_I^2} + \frac{\partial^2}{\partial z_I^2} \right) \tag{2.5}$$

and

$$\widehat{\mathrm{T}}_e = -\frac{\hbar^2}{2} \sum_i^n \frac{1}{m_i} \left(\frac{\partial^2}{\partial x_i^2} + \frac{\partial^2}{\partial y_i^2} + \frac{\partial^2}{\partial z_i^2} \right) \tag{2.6}$$

The potential energy contains three parts: nuclear–nuclear repulsion, electron–electron repulsion and electron–nuclear attraction, represented as

$$\begin{aligned} \widehat{\mathrm{V}}_{n-n} =& \frac{1}{4\pi\varepsilon_0} \sum_I^N \sum_{J>I}^N \frac{Z_I Z_J e^2}{R_{IJ}}, \\ \widehat{\mathrm{V}}_{e-e} =& \frac{1}{4\pi\varepsilon_0} \sum_i^n \sum_{j>i}^n \frac{e_i e_j}{r_{ij}}, \\ \widehat{\mathrm{V}}_{e-n} =& -\frac{1}{4\pi\varepsilon_0} \sum_i^n \sum_I^N \frac{Z_I e_i^2}{r_{iI}} \end{aligned} \tag{2.7}$$

Since the nuclear mass is much larger than the mass of an electron, it is reasonable to assume that the electronic distribution in a molecule depends mainly on nuclear positions and not on their velocities, and will adapt immediately to any changes in nuclear coordinates. The Born-Oppenheimer approximation introduces therefore the electronic Hamiltonian

$$\begin{aligned} \widehat{\mathrm{H}}_e =& -\frac{\hbar^2}{2} \sum_i^n \frac{1}{m_i} \left(\frac{\partial^2}{\partial x_i^2} + \frac{\partial^2}{\partial y_i^2} + \frac{\partial^2}{\partial z_i^2} \right) + \frac{1}{4\pi\varepsilon_0} \sum_I^N \sum_{J>I}^N \frac{Z_I Z_J e^2}{R_{IJ}} \\ &+ \frac{1}{4\pi\varepsilon_0} \sum_i^n \sum_{j>i}^n \frac{e_i e_j}{r_{ij}} - \frac{1}{4\pi\varepsilon_0} \sum_i^n \sum_I^N \frac{Z_I e_i^2}{r_{iI}}, \end{aligned} \tag{2.8}$$

which describes the electron motion in the field of fixed nuclei. By introducing atomic units ($e = m = \hbar = 1$) and the Laplacian operator

$$\Delta \equiv \nabla^2 \equiv \left(\frac{\partial^2}{\partial x^2} + \frac{\partial^2}{\partial y^2} + \frac{\partial^2}{\partial z^2} \right) \tag{2.9}$$

equation (2.8) can be rewritten as

$$\widehat{\mathrm{H}}_e = -\frac{1}{2} \sum_i^n \Delta_i + \sum_I^N \sum_{J>I}^N \frac{Z_I Z_J}{R_{IJ}} + \sum_i^n \sum_{j>i}^n \frac{1}{r_{ij}} - \sum_i^n \sum_I^N \frac{Z_I}{r_{iI}} \tag{2.10}$$

Solving the electronic Schrödinger equation for fixed nuclear coordinates

$$\widehat{\mathrm{H}}_e \Psi_e(\mathbf{r}; \mathbf{R}) = E_{eff}(\mathbf{R}) \Psi_e(\mathbf{r}; \mathbf{R}) \tag{2.11}$$

leads to an effective nuclear potential E_{eff} that describes the potential energy surface of the system and characterize the nuclear Hamiltonian:

$$\widehat{\mathrm{H}}_n = \widehat{\mathrm{T}}_n(\mathbf{R}) + E_{eff}(\mathbf{R}) \tag{2.12}$$

2.3 Density Functional Theory

The well-known wave function *ab initio* approach to solving the Schrödinger equation forms a well defined hierarchy offering systematic improvement towards the exact solution of the equation. However, a wavefunction for a closed-shell system, which contains all information about a given state of a system of electrons, is defined in 3N dimensional space. Hence the complexity of the problem increases with the size of the system. An alternative approach is offered by density functional theory where only the electron density is considered. This significantly reduces the complexity of the problem, as the electron density is a function of only three coordinates, independently of the number of electrons:

$$\rho(r) = \int \cdots \int |\Psi(\mathbf{r_1}, \mathbf{r_2}, \ldots, \mathbf{r_n}|^2 d\mathbf{r_2} \ldots d\mathbf{r_n} \tag{2.13}$$

The concept of DFT[†] has been mathematically proven by Hohenberg and Kohn by showing that a one-to-one mapping between the ground-state electron density ρ_0 and the external potential υ_{ext} exists. In the case of molecules,

[†]For overview see ref. [72]

the external potential is given by the nuclear Coulomb potential υ_{nuc}. This relation implies that the external potential and hence the Hamiltonian can be determined from a given ground-state electron density. By definition, also all the properties derivable from the Hamiltonian, such as the ground-state wavefunction and energy, excited-state wavefunctions and energies, can in principle be determined from the electron density.

Therefore, for a given external potential υ_{ext} a density functional exists, which provides an energy for any trial electron density in this potential

$$E \equiv E_\upsilon[\rho(\mathbf{r})] \equiv \int \upsilon_{ext}(\mathbf{r})\rho(\mathbf{r})d\mathbf{r} + F[\rho(\mathbf{r})] \tag{2.14}$$

where the integration variable $\mathbf{r}$ runs over all space. The theorem proves also a variational principle for the electron density. For any density $\rho(\mathbf{r})$, the corresponding energy functional $E_\upsilon[\rho]$ gives an energy that is larger than or equal to the ground-state energy, *i.e.*

$$E_\upsilon[\rho] \geqslant E_0 \qquad \forall\rho, \tag{2.15}$$

and the ground-state energy $E_\upsilon[\rho] = E_0$ is obtained only with the ground-state electron density ρ_0. Thus, for a given external potential the total energy is at a minimum for the ground-state electron density and if the functional $F[\rho(\mathbf{r})]$ is known, the ground-state energy and density for any electronic system can be determined, independent of the number of electrons.

The total energy functional can be decomposed into different contributions:

$$E_\upsilon[\rho] = T[\rho] + V_{ne}[\rho] + V_{ee}[\rho] \tag{2.16}$$

where $T[\rho]$ is the electronic kinetic energy, $V_{ne}[\rho]$ is the electrostatic attraction of the electrons and the nuclei and $V_{ee}[\rho]$ is the electron–electron repulsion energy, which can be decomposed into classical Coulomb and nonclassical terms:

$$V_{ee}[\rho] = J[\rho] + V_{ee}^{nc}[\rho] \tag{2.17}$$

While the $V_{ne}[\rho]$ and $J[\rho]$ can be calculated explicitly in terms of the electron

density:

$$\begin{aligned} V_{ne}[\rho] &= \int \upsilon_{nuc}(\mathbf{r})\rho(\mathbf{r})d\mathbf{r} \\ J[\rho] &= \int \frac{\rho(\mathbf{r})\rho(\mathbf{r}')}{|\mathbf{r}-\mathbf{r}'|}d\mathbf{r}d\mathbf{r}' \end{aligned} \tag{2.18}$$

the explicit form of the density functionals of the interacting kinetic energy and the nonclassical electron–electron repulsion energy are not known. To simplify calculations of the kinetic energy functional, Kohn and Sham proposed to separate the kinetic energy of non-interacting electrons of density $\rho(\mathbf{r})$, according to

$$T[\rho] = T_c[\rho] + T_s[\rho] \tag{2.19}$$

and to combine the remaining $T_c[\rho]$ contribution, together with the nonclassical electron–electron repulsion term, as the exchange and correlation functional:

$$E_{xc}[\rho] = T_c[\rho] + V_{ee}^{nc}[\rho] \tag{2.20}$$

The total energy functional can now be written as:

$$E_v[\rho] = T_s[\rho] + V_{ne}[\rho] + J[\rho] + E_{xc}[\rho] \tag{2.21}$$

By applying the variational principle (eq. 2.15) a set of one-electron self-consistent equations, called Kohn-Sham equations, can be derived:

$$\left[-\frac{\nabla^2}{2} + \upsilon_{nuc} + \int \frac{\rho(\mathbf{r}')}{|\mathbf{r}-\mathbf{r}'|}d\mathbf{r}' + \upsilon_{xc}(\mathbf{r})\right]\phi_i(\mathbf{r}) = \varepsilon_i\phi_i(\mathbf{r}) \tag{2.22}$$

where i runs over the number of electrons. The first term is the single-particle kinetic operator, the second term is the external potential, the integral corresponds to the classical electrostatic potential and the last term is the exchange-correlation potential defined as:

$$\upsilon_{xc}(\mathbf{r}) \equiv \frac{\partial E_{xc}[\rho(\mathbf{r})]}{\partial\rho(\mathbf{r})} \tag{2.23}$$

The auxiliary single particle wavefunctions $\phi_i(\mathbf{r})$ in Kohn-Sham orbitals give the electron density:

$$\rho(\mathbf{r}) = \sum_{i=1}^{n} |\phi_i(\mathbf{r})|^2 \tag{2.24}$$

2.4 Basis Set Approximation

To solve the KS equations in practice, the Kohn-Sham orbitals are expanded in a linear combination of known functions called the basis set, according to:

$$\phi_i = \sum_{\mu=1}^{k} c_{\mu i}\chi_\mu \tag{2.25}$$

where k is the number of basis functions. The choice of the χ functions depends on the application and for molecular systems typically atom-centered functions similar to atomic orbitals are used, such as Slater-type functions

$$\chi^{STF}_{\zeta,n,l,m}(r,\theta,\varphi) = NY_{l,m}(\theta,\varphi)r^{n-1}e^{-\zeta r} \tag{2.26}$$

or Gaussian-type functions

$$\chi^{GTF}_{\zeta,n,l,m}(r,\theta,\varphi) = NY_{l,m}(\theta,\varphi)r^{(2n-l-2)}e^{-\zeta r^2} \tag{2.27}$$

There are two major differences in the shape of Slater-type and Gaussian-type functions, as may be seen in Fig. 2.1. For $x = 0$ the GTF exhibits a zero

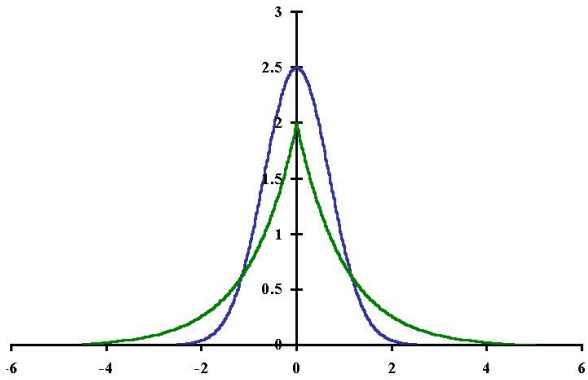

Figure 2.1: Unit exponent normalized GTF (blue line) and STF (green line). The functions are centered at the nucleus.

slope, while the STF has a discontinuous derivative. The other difference is that a GTF has problems in representing the near-nucleus region and falls

off too rapidly in comparison with STF. Therefore, a relatively large number of GTFs is necessary to describe energetically important but chemically unimportant core electrons. To reduce the computational cost, those functions (called *primitive GTFs*) are combined into a smaller set of *contracted GTFs* by forming a fixed linear combination:

$$\chi_\mu = \sum_p^l d_{\mu p} \chi_p \tag{2.28}$$

The smallest possible basis set, using one function for each occupied atomic orbital, is called a minimum basis set. This means that for elements from the second row of periodic table two s-functions (1s, 2s) and one set of p-functions ($2p_x$, $2p_y$, $2p_z$) are used. The so-called *Double Zeta* (DZ) basis set doubles the minimum basis set, assigning twice as many functions for each orbital — 1s, 1s', 2s, 2s', 2p, 2p'. As a compromise between accuracy and efficiency, *Split Valence Basis Sets* have been proposed, which double only the functions for valence orbitals. Similarly *Triple Zeta* (TZ), *Quadruple Zeta* (QZ), *Quintuple Zeta* (5Z) and higher sets have been developed, also in the valence split version.

In most cases, higher angular momentum functions, known also as *polarization functions*, are required to properly describe polarization of orbitals when a chemical bond is formed. Although not populated in the atomic ground state, they can be safely used both for hydrogens and heavy atoms. Also *diffuse functions*, *i.e.* s- and p-type functions with very small exponents, can be used for all the elements. Those functions improve standard basis sets, which are optimized mainly to reproduce energies with high accuracy, by a more detailed description of regions far away from nuclei. They should be in use whenever long-distance interactions, anions, excited states, molecules with electron lone pairs or properties such as polarizability are studied.

2.5 Exchange-Correlation Functionals

The exact form of the exchange-correlation functional $E_{xc}[\rho]$ is not known and there are no prescriptions how to approximate and systematically improve this functional. One of the earliest approximations is the local density

approximation in which the system is treated as a uniform electron gas:

$$E_{xc}^{\mathrm{LDA}}[\rho] = \int \epsilon_{xc}^{uniform}(\rho(\mathbf{r}))\rho(\mathbf{r})d\mathbf{r} \tag{2.29}$$

where $\epsilon_{xc}^{uniform}$ is the exchange-correlation energy per electron of a uniform electron gas of density ρ, derived from Quantum Monte-Carlo calculations. This functional is by definition exact for a homogeneous electron gas but works also surprisingly well for metals, failing however in applications for molecules, especially in predicting binding energies. The more accurate generalized gradient approximation

$$E_{xc}^{\mathrm{GGA}}[\rho, \nabla\rho] = \int f(\rho(\mathbf{r}), \nabla\rho(\mathbf{r}))d\mathbf{r} \tag{2.30}$$

considers also the gradient of the density. New generations of meta-GGA functionals include also the Laplacian of the density or the kinetic energy density, according to

$$E_{xc}^{\mathrm{mGGA}}[\rho, \nabla\rho, \nabla^2\rho] = \int f(\rho(\mathbf{r}), \nabla\rho(\mathbf{r}), \nabla^2\rho(\mathbf{r}))d\mathbf{r} \tag{2.31}$$

The most popular GGA functionals are the BP (Becke, Perdew) [73, 74] and BLYP [73, 75], combining the exchange functional of Becke with the correlation functional of Lee, Yang and Parr.

A separate family is the family of hybrid functionals. They mix a portion of exact exchange energy derived from Hartree-Fock method with the exchange and correlation GGA functional:

$$E_{xc}^{\mathrm{hybrid}}[\rho] = E_{xc}^{\mathrm{GGA}}[\rho, \nabla\rho] + c_x(E_x^{HF}[\rho] - E_x^{GGA}[\rho]) \tag{2.32}$$

The c_x coefficient controls the mixing between the Hartree-Fock and GGA exchanges. One of the remarkably successful hybrid functionals is the B3LYP functional. [75–77]

2.6 Time-dependent Density Functional Theory

The Time-dependent DFT[‡] originates from the Runge-Gross theorem, which is a time-dependent version of the Hohenberg-Kohn theorem, it follows that

[‡]For overview see ref. [78]

the time-dependent electron density $\rho(\mathbf{r},t)$ uniquely determines the external time-dependent potential $v_{ext}(\mathbf{r},t)$. Therefore, it is possible to formulate a set of time-dependent Kohn-Sham equations:

$$\left[-\frac{\nabla^2}{2}+v_{ext}(\mathbf{r},t)+\int\frac{\rho(\mathbf{r}',t)}{|\mathbf{r}-\mathbf{r}'|}d\mathbf{r}'+v_{xc}(\mathbf{r},t)\right]\phi_i(\mathbf{r},t)=i\frac{\partial}{\partial t}\phi_i(\mathbf{r},t) \quad (2.33)$$

where $v_{xc}(\mathbf{r},t)$ is the unknown time-dependent exchange-correlation potential. Similar to ground-state DFT, the density is obtained from the noninteracting orbitals:

$$\rho(\mathbf{r},t)=\sum_{i=1}^{n}|\phi_i(\mathbf{r},t)|^2 \quad (2.34)$$

For the determination of properties like excitation energies and polarizabilities, only the knowledge of the linear density response of the system to the perturbation of the potential (v_1) is required:

$$v_{ext}(\mathbf{r},t)=\begin{cases} v_0(\mathbf{r}) & ;\ t\leqslant t_0 \\ v_0(\mathbf{r})+v_1(\mathbf{r},t) & ;\ t>t_0 \end{cases} \quad (2.35)$$

Using the perturbation theory, it is possible to expand the density $\rho(\mathbf{r},t)$ as a functional of the external potential v_{ext} in a Taylor series:

$$\rho(\mathbf{r},t)=\rho_0(\mathbf{r})+\rho_1(\mathbf{r},t)+\rho_2(\mathbf{r},t)+\ldots \quad (2.36)$$

The first term corresponds to the unperturbed density at $t<t_0$, which can be obtained from the ground-state KS equations in the potential $v_0(\mathbf{r})$.

The first-order time-dependent density can be calculated therefore from the exact linear response function χ, evaluated at the ground-state potential v_0:

$$\chi(\mathbf{r},t;\mathbf{r}',t')=\frac{\delta\rho[v_{ext}](\mathbf{r},t)}{\delta v_{ext}(\mathbf{r}',t')}\bigg|v_0 \quad (2.37)$$

as

$$\rho_1(\mathbf{r},t)=\int d\mathbf{r}'\int\chi(\mathbf{r},t;\mathbf{r}',t')v_1(\mathbf{r}',t')dt' \quad (2.38)$$

The unknown response function can be obtained from the unperturbed KS orbitals, their occupation numbers f_j and their orbital energies ε_j through:

$$\chi_s(\mathbf{r},\mathbf{r}';\omega)=\sum_{j,k}(f_k-f_j)\frac{\phi_j(\mathbf{r})\phi_k^*(\mathbf{r})\phi_j^*(\mathbf{r}')\phi_k(\mathbf{r}')}{\omega-(\varepsilon_j-\varepsilon_k)+i\eta} \quad (2.39)$$

where η is a positive infinitesimal. In this way absorption energies ω are accessible directly from the ground-state electron density. For the real density response of a molecule in an electric field, real Kohn-Sham orbitals ϕ_j and $\eta = 0$ can be used.

2.7 Chemical Models

The accuracy of a theoretical study depends both on computational method and chemical models chosen to represent the studied system. Proteins, due to their size, are in general beyond the current capabilities of full quantum theoretical description and therefore either a combined quantum mechanics/molecular mechanics (QM/MM) treatment or a model approach must be used. In the first methodology, the most crucial parts of proteins are described quantum mechanically, while the remaining part is considered on the MM level. The second approach, used in this thesis, is based on studying a model for the functional core of a protein under consideration. Usually the model is built with a reference to the protein's X-ray structure and contains residues essential for the investigated mechanism. In order to reproduce the missing protein environment, specific geometrical constraints may be additionally introduced. In this thesis, all the models were systematically refined in an evidence-based preparation procedure, *i.e.* until a satisfactionary agreement with available NMR data was achieved.

Chapter 3

Protein-induced Geometric Constraints and Charge Transfer in BChl *a*–His Complexes of LH2

3.1 Introduction

In this chapter a systematic DFT study of the NMR chemical shifts for histidine and for bacteriochlorophyll *a*–histidine complexes in the light-harvesting complex II is performed. The investigated protonation states of the imidazole side chain include also neutral$_\pi$ and the anionic cases, which, although not much studied in the literature, appear to play an important function in biological systems. Recently it has been argued that the negatively charged histidine may play a role in the electron transfer process in Photosystem II. [79]

The computed chemical shift patterns are consistent with available experimental data for cationic and neutral$_\tau$ crystalline histidines. The results for the bacteriochlorophyll *a*–histidine complexes in LH2 strongly suggest that the protein environment in LH2 exerts a stress on the histidine coordinated to the bacteriochlorophyll *a* resulting in a large charge transfer and a com-

bined structural change. Due to this protein induced geometric constraint, the Mg-coordinated histidine in LH2 appears to be in a frustrated state very different from the formal neutral$_\pi$ form. Finally, the pyridine character of the Mg-bound nitrogen in the LH2 complex is addressed, together with discussion on the effect of hydrogen bonds on the histidine chemical shifts.

The results and discussion section contains first the calculations for histidine in vacuum in comparison with available experimental data for lyophilized crystalline samples of histidine and a discussion on the accuracy of DFT chemical shifts. The following subsections address the problem of protonation state assignment in non-coordinated and Mg-coordinated histidines in LH2.

3.2 Models and Methods

All calculations for His and BChl *a*–His complexes were performed in vacuum within the DFT framework with the Gaussian 03 package. [80] The applied BLYP [73, 75, 76] exchange-correlation functional has been already shown to produce accurate chemical shifts for similar systems. [81] Additionally the B3LYP hybrid functional [75–77] was tested (Table A.2 in the appendix) and it has a marginal effect on the chemical shifts when compared to BLYP.

Basis set tests were performed for the reference compounds (TMS, NH_3) and histidine in all four possible protonation states of its imidazole ring. The discussion is presented in the appendix, together with the results collected in the appendix Tables A.1 and A.3. Based on these tests, the 6-311++G(d,p) basis set was chosen for the remaining part of the study, except for the geometry optimization of the BChl *a*–His complexes (Fig. 3.1) where the 6-31++G(d,p) basis set was used.

The initial structure for the BChl *a*–His complex in LH2 was extracted from one of the B850 BChl dimer units in the 2FKW PDB crystallographic structure of *Rps. acidophila*. [36] According to the crystal structure the two BChl *a* molecules in the dimer are slightly asymmetric, but the two histidines coordinated to them appear to be equivalent according to the NMR spectra. [26, 39] Therefore only one subunit of the dimer was included, namely β-His 30 and BChl 1601, since the characterization of the histidine chemical

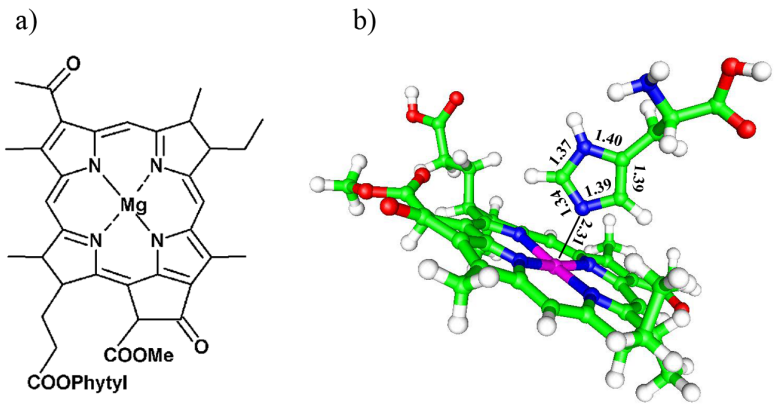

Figure 3.1: a) Schematic representation of the bacteriochlorophyll *a* structure. b) DFT-optimized structure of the neutral BChl *a*–His complex. The phytyl tail was truncated at the esther group and substituted by a hydrogen atom. The bond lengths in the imidazole ring and the Mg–N_τ distance (Å) are also shown.

shifts is the primary aim. To model histidines in a protein environment a neutral amino acid termination (COOH–NH_2) was used to saturate the broken peptide bond. Other protonation states of the amino acid termination that can occur in solution are not of interest for this work. The phytyl tail of the bacteriochlorophyll *a* was truncated at the esther group and saturated by a hydrogen atom in the model (see Fig. 3.1). This truncation does not affect the electronic structure of the porphyrin ring.

The geometries were fully optimized and the NMR chemical shieldings were calculated using the GIAO method. [82–85] The calculated ^{1}H and ^{13}C chemical shieldings were referred to the TMS chemical shifts scale, while the computed ^{15}N chemical shieldings were referred to the value of $^{15}NH_3$. The experimental chemical shifts referred to $(^{15}NH_4)_2SO_4$ powder were converted to the $^{15}NH_3$ scale by adding 20 ppm, as suggested in ref. [86].

The ADF program [87–89] was used to calculate the electron charge difference map between the BChl *a*–His complex and its two fragments, histidine and bacteriochlorophyll *a*. The BLYP functional with the TZP Slater-type basis set was used for this calculation.

3.3 Results and Discussion

3.3.1 Chemical shifts calculations for histidine in vacuum

Geometry

Figure 3.2 shows a comparison of the imidazole ring bond lengths in the DFT-optimized histidine with available crystal structures. Several crystal

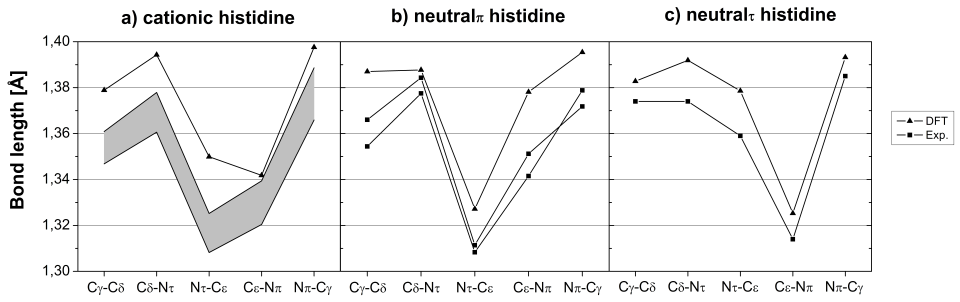

Figure 3.2: Comparison between experimental and DFT bond lengths in the imidazole ring of histidine. a) Cationic histidine. The experimental values are from ref. [21,90,91]. The grey area represents the experimental range of bond lengths from different crystal structures. b) Neutral$_\pi$ and c) neutral$_\tau$ histidines. The experimental values are from ref. [21] and [92], respectively.

structures available in the Cambridge Structural Database were analyzed, namely ADAVOQ [21], ADAVUW [21], CAMWOD [90], CAMWUJ [90], ZOZWAM [91], as well as the structure determined by Edington *et al.* [92]. Interestingly, the ADAVUW structure contains two cationic and two neutral$_\pi$ histidines in the unit cell and, according to our knowledge, it is the only evidence of the neutral$_\pi$ tautomer in a simple crystal compound. A very good agreement in the bond lengths is observed for all the available histidine forms, with only a small systematic overestimation of around 2%. This is a typical DFT accuracy for the geometrical parameters, especially taking into account that the specific crystalline environments are neglected. It is worth pointing out that the optimized geometries of the cationic and neutral$_\pi$ histidines show an intra-molecular hydrogen bond between N$_\pi$ and the C=O group of the histidine tail.

Chemical shifts

Table 3.1 and Figure 3.3 present a comparison of the calculated histidine chemical shifts with NMR measurements on crystal samples [26, 29] available only for histidines with a cationic and neutral$_\tau$ imidazole ring. [29] The com-

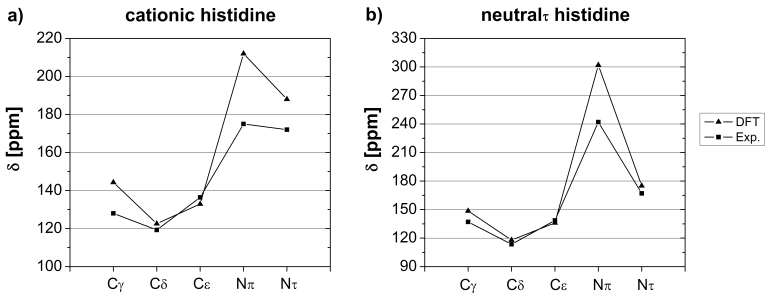

Figure 3.3: Comparison between experimental and DFT chemical shifts [ppm] for a) cationic histidine and b) neutral$_\tau$ histidine. The experimental values are from ref. [26, 29] for histidine crystal samples.

parison shows a good agreement for C_δ and C_ε (≈4 ppm error on average, 3%) and for N_τ (≈12 ppm error on average, 7%). The largest deviations are observed for C_γ (16 ppm, 13%) and N_π (60 ppm, 25%). Unfortunately, for the neutral$_\pi$ tautomer only selected chemical shifts within various protein environments have been reported. [25] However, this tautomer has been already observed in a simple compound [21] and could be used in the future as a generic model for chemical shifts of neutral$_\pi$ histidine. Interestingly, DFT predicts that the three ^{13}C signals in neutral$_\pi$ histidine should appear very close to each other, contrary to the other three forms (Table 3.1). Moreover, the condition mentioned in the introduction to distinguish between the two neutral tautomers [25] is satisfied by the computed C_δ chemical shifts.

A direct comparison for the doubly deprotonated histidine is also not possible as it has never been clearly observed experimentally. According to the calculations the most peculiar feature of the anionic form is the remarkably large C_ε chemical shift value of 154 ppm, which is about 20 ppm downfield compared to the other three cases. This supports the suggestion that a doubly deprotonated histidine may be present in the Photosystem II. [79]

	Histidine (exp.)[a)]		Histidine (DFT)					4-Methylimidazole (DFT)		
	cationic	neutral$_\tau$	cationic	neutral$_\tau$	neutral$_\tau$...x	neutral$_\pi$	anionic	neutral$_\tau$	neutral$_\pi$	neutral$_\pi$...x
C$_\gamma$	128.0	137.0	144.3	148.5	147.7	131.6	137.7	147.3	129.8	130.7
C$_\delta$	119.3	113.5	122.6	117.9	118.0	134.5	133.4	113.9	133.6	133.4
C$_\varepsilon$	136.4	138.6	132.9	136.0	137.1	137.3	154.0	136.3	136.8	137.0
N$_\pi$	175	242	212	302	301	190	293	306	183	192
N$_\tau$	172	167	188	175	186	303	295	174	304	302
H$_\delta$			7.2	6.9	6.9	7.0	7.0	6.7	6.9	6.8
H$_\varepsilon$			8.0	7.4	7.5	7.3	7.4	7.3	7.3	7.4

[a)] ^{13}C chemical shifts from ref. [26], ^{15}N chemical shifts from ref. [29].

Table 3.1: Calculated histidine and 4-methylimidazole chemical shifts [ppm] for different protonation states in comparison with available experimental data for crystal histidine. The experimental values for ^{15}N are converted to NH_3 as a reference compound (see section on computational details). 'x' denotes an inter-molecular hydrogen bond with a water molecule at the pyrrole nitrogen.

Table 3.1 contains also the chemical shifts computed for two neutral tautomers of the 4-methylimidazole. These chemical shifts are very similar to those of neutral histidines, except for N_π in the neutral$_\pi$ tautomer where a difference of 7 ppm is observed. When adding a water molecule forming an inter-molecular hydrogen bond to 4-MeIm at the π position, the N_π chemical shift has almost the same value as in neutral$_\pi$ histidine. This result shows that the inter-molecular and the intra-molecular H-bond have the same effect on the N_π chemical shift. It can be also noticed that the chemical shifts of C_ε are almost equal in the two neutral tautomers due to the symmetry of the ring.

Apart from comparing absolute values, it is also useful to compare the chemical shift changes upon protonation or deprotonation of the imidazole ring. In this way systematic DFT errors are partially canceled and it is easier to identify trends that may help in the assignment of histidine protonation states. Figure 3.4a presents the experimental, denoted as 'Exp. Crystal', and DFT chemical shift differences between cationic and neutral$_\tau$ histidines defined as $\Delta\delta = \delta_{\mathrm{form1}} - \delta_{\mathrm{form2}}$. The pattern in $\Delta\delta$ is correctly reproduced by the calculation. The largest deviations from experiment are found for the N_τ (7.7 ppm) and N_π (23 ppm) nitrogens.

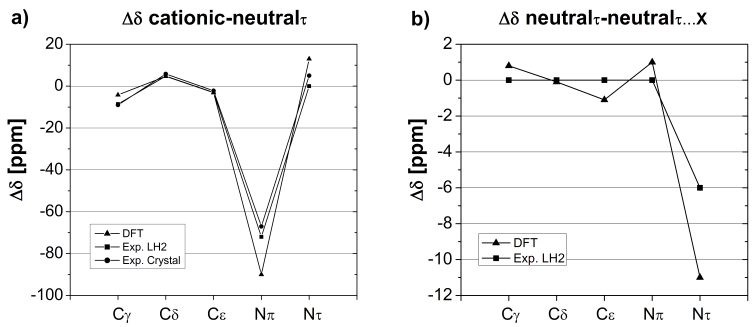

Figure 3.4: a) Chemical shift difference $\Delta\delta = \delta_{\mathrm{cationic}} - \delta_{\mathrm{neutral}\tau}$ [ppm] derived for DFT calculations, histidine crystal samples [26,29] and β-His 41, α-His 37 in LH2 [26,39]. b) Chemical shift difference $\Delta\delta$ [ppm] between neutral$_\tau$ tautomer and neutral$_\tau$ with H-bond on the N_τ atom derived for DFT calculations and α-His 37, β-His 12 in LH2 [26,39].

Source of error for chemical shifts

The comparison between theoretical and experimental chemical shifts exhibits an overall good agreement for the carbon atoms. The largest deviation is observed for C_γ, possibly due to the large effect of the environment on this particular carbon, related to the tail orientation. Indeed C_γ is known to be sensitive to the protein environment and for that reason is not used for discriminating between the two neutral tautomers. [25]

Although the pyrrole and pyridine character of the nitrogens in the different protonation states is correctly reproduced by the calculation, significant differences with the experimental values are observed for ^{15}N chemical shifts. Due to the high polarizability of the nitrogen atom, hydrogen bonding and other intermolecular interactions strongly affect the ^{15}N chemical shieldings. [27, 93–96] By neglecting those effects, the standard deviation between experimental and DFT ^{15}N chemical shifts may be as large as 30 ppm [97], which is 18% of the protonated ^{15}N chemical shift value. Moreover, even if those intermolecular interactions are included, an error of 17 ppm (10%) is still observed. [97] These previous findings are in line with the errors observed in the present calculations. A considerable effort is under way in finding efficient ways of including the environmental effects in the chemical shift calculations through embedding schemes at various levels of accuracy. [98–100] An explicit inclusion of the crystal environment is outside the scope of the present work. In conclusion, some care should be taken when comparing DFT absolute chemical shifts with experimental data, especially for nitrogen atoms. The comparison of relative chemical shifts is more reliable since the error is partially canceled out, as may be seen in Figure 3.4.

3.3.2 Protonation state of histidines in the LH2 complex

Non-coordinated histidines (α-His 37, β-His 12, β-His 41)

Experimentally resolved NMR chemical shifts for histidines in LH2 are shown in Table 3.2. The proposed assignment was based on the experimental values for crystal samples of histidine. [26, 39] It was also suggested, based on the nitrogen chemical shifts, that some of the histidines in LH2 are involved in

	Experiment LH2 [a]				DFT				
	β-His 12	α-His 37	β-His 41	α-His 31, β-His 30	**1**	**2**	**3**	**4**	**5**
	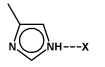		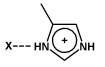	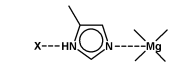	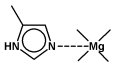	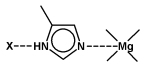	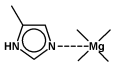	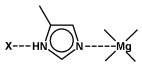	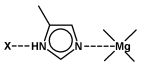
C_γ	133.7	133.7	125.1	125.1	133.6	134.1	129.5	130.0	128.8
C_δ	113.5	113.5	118.3	118.3	129.7	128.6	124.5	123.7	125.2
C_ε	136.5	136.5	133.5	133.5	135.6	136.5	132.2	131.4	134.3
N_π	250	250	178	178	188	196	175	183	196
N_τ	176	170	170	225	277	277	281	278	273
H_δ	6.2	6.2	6.5	2.6	3.0	2.9	4.6	4.4	3.8
H_ε	7.4	7.4	7.9	4.2	3.1	3.2	3.3	3.6	4.7

[a] from ref. [26,39]

Table 3.2: Calculated and experimental chemical shifts for histidines in the LH2 complex. In the schematic representation of the model, the histidine tail and the remaining part of the BChl *a* molecule were omitted for clarity. The indicated charge of histidine is the formal charge. 'X' denotes a hydrogen bond. The structure of the complexes **1** and **2** was fully optimized, the complexes **3** and **4** corresponds to the X-ray structure of LH2 [36], while the complex **5** was partially optimized (see text for details).

hydrogen bond interactions. [26,39] The chemical shift difference $\Delta\delta$ between cationic β-His 41 and the neutral α-His 37 is shown in Figure 3.4a (Exp. LH2) together with the DFT-predicted $\Delta\delta$ between cationic and neutral$_\tau$ histidine in vacuum. The experimental pattern is correctly reproduced: The $\Delta\delta$ for C_γ and C_ε is predicted to be -4.2 ppm ($\Delta\delta^{exp} = -8.6$ ppm) and -3.1 ppm ($\Delta\delta^{exp} = -3.0$ ppm), respectively, while for C_δ it is $+4.7$ ppm ($\Delta\delta^{exp} = +4.8$ ppm). Finally, a large chemical shift difference of 72 ppm is observed experimentally for N_π, while no change occurs for N_τ. The theoretical results also show a large difference of 90 ppm for N_π, while N_τ is predicted to shift by 13 ppm. The ^{1}H signals are reproduced very well, both in absolute and relative values (see Tables 3.1 and 3.2).

Figure 3.4b presents the experimental chemical shift differences $\Delta\delta$ between α-His 37 andβ-His 12 (Table 3.2) compared with the theoretical $\Delta\delta$ between neutral$_\tau$ and neutral$_\tau$ including a hydrogen bonded water at the N_τ site (Table 3.1). This comparison reveals that the presence of a hydrogen bond affects mainly the N_τ chemical shift and confirms the experimental suggestion that β-His 12 is involved in a hydrogen bond. [26,39]

Mg-coordinated histidines (α-His 31, β-His 30)

The DFT results for various BChl *a*–His complex models are collected in Table 3.2. It has been suggested that these Mg-coordinated histidines may be involved in hydrogen bonding on the N_π side with the C13^1-keto carbonyl of the adjacent bacteriochlorophyll *a* molecule. [26,39] Therefore complexes **2**, **4** and **5** were studied, which include an inter-molecular hydrogen bond between N_π and a water molecule. The structure of the BChl *a*–His complexes **1** and **2** was fully optimized, while the complexes **3** and **4** were kept fixed according to the crystallographic data. [36] The complex **5** was partially optimized in the presence of some geometrical constraints, as explained below.

By comparing the chemical shifts for the complexes with and without the hydrogen bond, it is seen that the main effect is a change of 8 ppm in the chemical shift of the pyrrole-type nitrogen. Since this type of nitrogen gives a NMR resonance at 170 ppm, the observed chemical shift value of 178 ppm for N_π in Mg-coordinated histidine can be indeed attributed to the presence

of a hydrogen bond. However, a careful analysis of the X-ray structure in the vicinity of the β-His 30 leads to the conclusion that the hydrogen bond partner is the alanine β-Ala 26 and not the carbonyl group of the adjacent BChl *a* molecule suggested earlier. [26, 39]. Thus, the Ala 26 C=O forms two hydrogen bonds with His 30: one with the backbone NH and one with the side chain N_π. A similar situation occurs for the α-His 31 and α-Ala 27.

The computed chemical shifts for the imidazole protons H_δ and H_ε in the BChl *a*–His complexes (Table 3.2) clearly show a ring current effect of about 4 ppm when compared with the values for the non-coordinated histidines (Table 3.1), which is in very good agreement with the experiment.

The ^{13}C experimental data for the Mg-coordinated histidines are the same as those of the cationic histidine, suggesting that a charge transfer is taking place from the histidine to the bacteriochlorophyll. [26, 39] The DFT ^{13}C chemical shifts are in much better agreement with the experimental values when the X-ray structure is considered without performing a geometry optimization (Table 3.2, complexes **2** and **4**). This result pinpoints that the constraints due to the protein environment have a significant effect on the electronic structure of the BChl *a*–His complex. The comparison between the crystallographic data and the optimized geometry shows that in the course of geometry optimization (i) the Mg–N_τ distance increases from 2.12 Å to 2.31 Å in the DFT-optimized structure; (ii) the dihedral angle φ defined by N4, Mg, N_τ and C_ε, which represents the rotation of histidine around the Mg–N_τ axis, increases from 32° to 48°; and (iii) the BChl *a* ring becomes more flat. These changes in the geometry correspond to a change in the total imidazole ring charge from 0.2 for the optimized complex **2** to 0.5 for the non-optimized complex **4**, clarifying why the formally neutral$_\pi$ Mg-coordinated histidine in LH2 behaves as cationic histidine.

According to the X-ray data the imidazole ring of β-His 30 shows bond lengths typical for doubly protonated histidines. However, the RMSD on the bond lengths in the LH2 X-ray data is 0.03 Å, which is about the bond length difference between cationic and neutral$_\pi$ histidines. Therefore a constrained geometry optimization of the BChl *a*–His complex was additionally performed, in which only the imidazole ring was relaxed, while the Mg–N_τ

distance and the dihedral angle φ defined above were kept fixed. It was found that: (i) the charge transfer is essentially the same as obtained using the non-optimized crystal structure; (ii) a RMSD of 4.5 ppm for the ^{13}C chemical shifts resulting from this partially optimized structure is the same as for the crystal structure (see Table 3.2, complexes **4** and **5**); (iii) the bond lengths in the imidazole ring are now systematically shorter by 0.01–0.02 Å with respect to the fully optimized structure, as presented in Figure 3.5. It can be con-

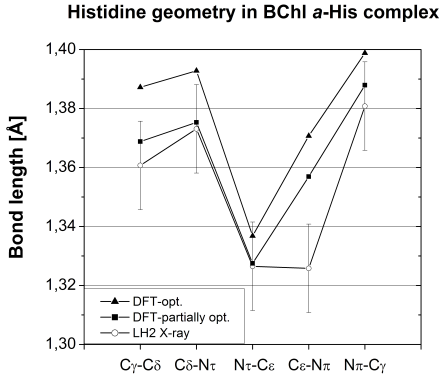

Figure 3.5: Bond lengths of the histidine imidazole ring in BChl *a*–His complex: DFT-optimized structure (triangles), DFT-partially optimized structure (squares) and X-ray structure of LH2 [36] (open circles).

cluded that the charge transfer depends crucially on the relative distance and orientation of the BChl *a*–His complex. This charge transfer can be clearly visualized by computing the charge density difference between the BChl *a*–His complex and the two fragments, His and BChl *a*, separately (Figure 3.6). The DFT results strongly suggest that the protein environment is forcing the histidine to stay close to the BChl *a*, thereby inducing a combined structural change and a large charge transfer. When the constraints from the protein are removed, the structure relaxes and histidine moves away from its close position to the bacteriochlorophyll *a*.

Although the ^{13}C data show the character of cationic histidine, the Mg-coordinated N_τ still maintains its pyridine character. [26] This is also con-

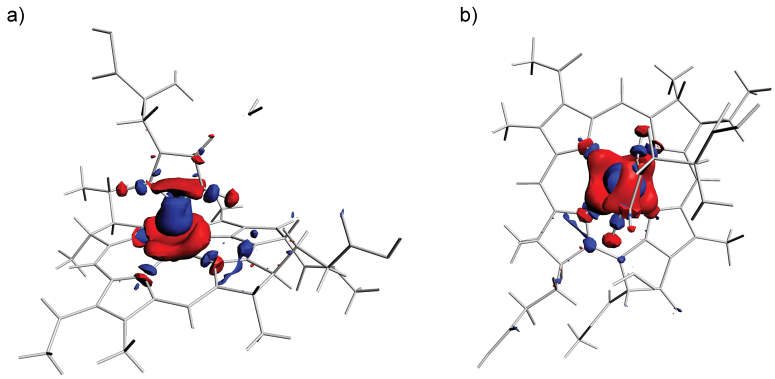

Figure 3.6: Change in the electronic density upon BChl *a*–His complex formation, calculated for the partially optimized structure (see text for details). The isosurface value is 0.0012 e/Å^3. Red corresponds to an increase of the density in the complex, as compared to the separated BChl *a* and His fragments, while blue denotes a decrease in the electronic density. a) Side view and b) top view.

firmed by the calculated anisotropy parameters for N_τ in the complex **5**: The computed δ and η are 8.9 kHz and 0.5, respectively, *vs.* 8.4 kHz and 0.4 estimated from NMR measurements [26] and agree well with the values expected for pyridine-type nitrogen. These results emphasize the state of frustration, especially for the N_τ and may indicate that histidine is in a protein-induced frustrated state between the neutral and the cationic electronic structure.

This finding of a protein induced charge transfer in the BChl *a*–His complex may have important effects on the absorption spectra and excitation energy transfer processes observed in LH2. Not only the excitation site energies and transition dipole moments of the BChl *a*–His complex, but also the long-range electrostatic interactions with the protein environment may change significantly. Preliminary time-dependent DFT calculations performed on the BChl *a*–His model and presented in Table 3.3 show a significant effect mainly on the Q_x absorption band when compared to the isolated BChl *a*. This result appears to be in line with absorption spectroscopy studies of BChl *a* in solvents. [101] In a recent DFT study, Neugebauer [102] has addressed the issue of the environmental effects on the excitation energies and photophysical properties of LH2 complexes. However, in that study the histidine has been

	Q_x			Q_y		
	E_{exc}	f	type	E_{exc}	f	type
BChl *a*	1.94	0.10	H-1 → L 83%	1.56	0.31	H → L 94%
BChl *a*–His	1.87	0.08	H-1 → L 85%	1.56	0.28	H → L 94%

Table 3.3: Calculated (SAOP/TZP) excitation energies (eV) and oscillatory strengths for BChl *a* and BChl *a*–His models. 'H' corresponds to HOMO and 'L' corresponds to LUMO.

modeled by a frozen density embedding approach, which may be inappropriate when charge transfer is taking place.

3.4 Conclusions

A comprehensive DFT analysis of the chemical shifts for different protonation states of the histidine imidazole ring was presented. The comparison with experimental data for crystal samples shows that trends can be predicted with good accuracy and that the largest errors are observed for pyridine type nitrogen atoms that may be strongly affected by the specific environment.

The DFT chemical shifts support the recently proposed assignment of the histidines protonation state in LH2 and confirm that all the histidines except α-His 37 participate in a hydrogen bond. Moreover, the results put forward the idea that the protein environment in LH2 exerts a stress on the Mg-coordinated histidines that induces a considerable electron charge transfer to the bacteriochlorophylls *a*, what explains why these histidines behave as cationic and not as neutral$_\pi$ histidines. This result has already stimulated more thorough investigation of protein local frustrations, with NMR chemical shifts used as markers. [103] The observed charge transfer may have far-reaching consequences on the absorption properties and photophysics of the BChl *a* macrocycle in the LH2 dimeric B850 complex. The understanding of these basic functional mechanisms will guide the design of future artificial photosynthesis devices.

Chapter 4

Electronic Structure of Histidines in Bacterial Reaction Center

4.1 Introduction

This chapter presents an assignment of protonation states and interpretation of NMR spectra for histidines in *Rhodobacter sphaeroides* bacterial reaction centers. As discussed in the general introduction, the asymmetry of the special pair both in the ground state and in the excited state may facilitate the asymmetric electron transfer along the cofactor branches. Although a number of studies on the role of the protein environment in the electron transfer do exist [104, 105], a precise indication of the effects induced by the neighboring residues is still missing. [106, 107] Solid-state NMR combined with quantum chemical calculations is a powerful technique able to resolve electronic structure of residues, even in large membrane proteins like for instance the LH2 complex. [26, 39, 108] Here an interpretation of SSNMR spectra for the four Mg-coordinated and twelve other histidines in the BRC is proposed, based on the theoretical prediction of chemical shifts. It is established that all the axial BChl *a*-ligating histidines exist in the neutral$_\pi$ form. Interestingly, one of

them has a special electronic structure, different from the other three, which is attributed to the presence of a hydrogen-bonded water at the N_π nitrogen, effectively breaking the overall symmetry of those four histidines. [50] According to the calculations such interaction causes a reorganization of electronic density within the imidazole ring, affecting all the atoms. That, in turn, brings the coordinated histidine and bacteriochlorophyll *a* closer together. This structure modification may have a significant effect on the electron transfer properties. Also chemical shifts of non-axial histidines are investigated. It is proposed that in addition to several neutral$_\tau$ histidines, two groups of cationic histidines exist: doubly protonated and doubly protonated with hydrogen bonds at N_π and N_τ. The last group is characterized by a downfield shifted C_δ resonance.

4.2 Models and Methods

The Density Functional Theory calculations were performed using the Gaussian 03 package [80] and the BLYP [73,75,76] exchange-correlation functional in combination with the 6-311++G(d,p) basis set. This approach has been found to be an optimal trade-off between computational cost and accuracy in order to be accurate enough to confirm and validate experimental findings for light-harvesting complex II. [108] It was established that DFT calculations can predict accurately chemical shift differences between different histidine protonation states, although the deviation from the experiment in the absolute values may be large, especially for ^{15}N chemical shifts. Histidine in various protonation states of the imidazole ring were considered and their geometry was fully optimized, yielding cationic and neutral$_\pi$ histidine with an internal hydrogen bond between N_π and the carbonyl group of the tail.

To model the axial histidines the BChl *a*–His complex was extracted from the 1M3X crystal structure of the *Rhodobacter sphaeroides* reaction center. [50] The model incorporates P_L, His L173 and the water 1007 molecule to study the effect of the hydrogen bond at the N_π nitrogen of histidine. To model histidines in a protein environment, a neutral amino acid termination (COOH–NH_2) was used to saturate the broken peptide bond. The phytyl tail of the bacteriochlorophyll *a* was truncated at the esther group and saturated

by a hydrogen atom in the model. Neither the electronic structure of histidine side chain, nor the electronic structure of the porphyrin ring is affected by these truncations.

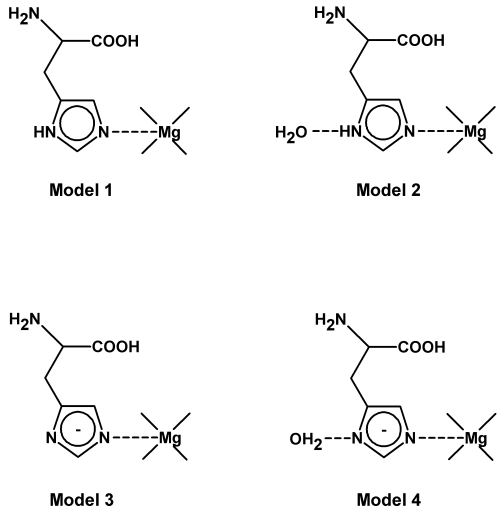

Figure 4.1: The models of BChl *a*–His complexes in various protonation states. In the schematic representation of the model, the remaining part of the BChl *a* molecule was omitted for clarity. The indicated charge of histidine is the formal charge.

Four models were considered, as shown in Fig 4.1, accounting for possible protonation states of the histidine side-chain and presence or absence of the hydrogen bond: Model **1** including BChl *a* and His in the neutral$_\pi$ form; Model **2** obtained by adding to model **1** the water molecule hydrogen bonded to His L173; Model **3** and **4** similarly to model **1** and **2**, respectively, but with the histidine ring deprotonated (formally anionic). The geometries of all the models were partially optimized by relaxing the atomic positions of the imidazole ring, the Mg atom and the two hydrogens of the water molecule, while keeping all the other atomic coordinates fixed to the crystallographic data. These constraints were introduced in order to maintain the geometric shape of the complex induced by the protein environment.

Chemical shifts were calculated using the GIAO method for all the models. [82–85] The ^{1}H and ^{13}C chemical shifts were referred to TMS, while the

^{15}N chemical shifts were referred to $^{15}NH_3$ and are all reported in ppm. The ADF program [87–89] was used to calculate the electron density difference map between the BChl *a*-His-H2O complex (**2**) and the two fragments: BChl *a*-His and water, in order to characterize the electron density perturbation induced by the presence of the hydrogen bond. The BLYP functional with the TZP basis set was used for this calculation.

4.3 Results and Discussion

The recorded 2D ^{1}H-^{13}C dipolar correlation spectrum of [^{13}C,^{15}N]-histidine labeled reaction centers is presented in Figure 4.2 and the experimental chemical shifts are collected in Table 4.1, together with theoretically predicted chemical shifts for various BChl *a*–His complexes. The four BChl *a*-coordinated histidines are clearly separated from the non-axial ones by the upfield shift of H_δ and H_ε signals due to ring current effects experienced by the atoms close to the conjugated porphyrin system of BChl *a*. The non-axial residues

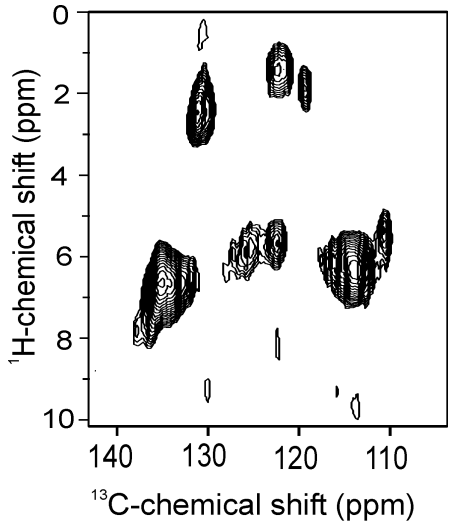

Figure 4.2: Contour plot sections of 2D heteronuclear ^{1}H-^{13}C dipolar correlation spectrum of [^{13}C,^{15}N]-histidine labeled bacterial reaction centers collected in a magnetic field strength of 17.6 T. Courtesy of A. Alia

resonate in the range of ≃5–8 ppm, while the signals from the axial histidines

	Experiment			DFT				
	Type 1	Type 2	$\Delta\delta_{type1-type2}$	**1** 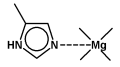	**2** 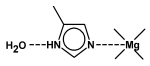	$\Delta\delta_{1-2}$	**3** 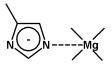	**4** 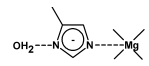
C_γ				131.6	131.7	−0.1	139.5	138.2
C_δ	121.9	119.1	2.8	128.6	127.6	1.0	120.1	120.4
C_ε	130.9	129.9	1.0	135.8	136.0	−0.2	145.3	144.3
C_ε -C_δ	9.0	10.8	−1.8	7.2	8.4	−1.2	25.2	23.9
N_π				189	200	−11	303	284
N_τ	225	220	5	268	265	3	244	246
H_δ	1.5	1.9	−0.4	4.0	4.0	0.0	3.8	3.7
H_ε	2.5	2.4	0.1	3.4	3.2	0.2	3.4	3.3

Table 4.1: Comparison between experimental chemical shifts [ppm] of axial histidines in BRC with theoretically predicted values for the different BChl *a*–His complexes considered in this work. The difference between models **1** and **2** ($\Delta\delta_{1-2}$) and the difference between the experimental data for Type 1 and Type 2 histidines ($\Delta\delta_{type1-type2}$) are also reported. In the schematic representation of the model, the histidine tail and the remaining part of the BChl *a* molecule were omitted for clarity. The indicated charge of histidine is the formal charge.

appear between ≃1–3 ppm. This ring current shift is reproduced by the calculations, as may be noticed by comparing the ^{1}H chemical shifts for BChl *a*–His complex in Table 4.1 with the chemical shifts for uncoordinated histidines in Table 3.1. The signals around 120 ppm are assigned to C_{δ}, while those around 130 ppm to C_{ε}.

4.3.1 Axial histidines

The upper part of the 2D NMR correlation spectrum, which concerns the signals from the axial histidines, will be considered first. From the analysis of the experimental and DFT-computed C_{ε} - C_{δ} chemical shift differences presented in Table 4.1 it is immediately visible that the N_{π} atom is protonated in all the axial histidines. The presence of negatively charged histidine would produce C_{δ} and C_{ε} NMR signals separated by $\sim$ 25 ppm (models **3** and **4**), while in the BRC those signals are experimentally observed only $\sim$ 10 ppm apart, in good agreement with the prediction for the BChl *a*–His complex with formally neutral$_{\pi}$ histidine (models **1** and **2**). Therefore it may be concluded that the axial histidines in BRC are formally neutral$_{\pi}$. This conclusion is particularly relevant since it has been recently suggested that anionic histidines may be present in Photosystem II, where they may play an important functional role. [79] In spite of similarities between the two systems, in BRC there is no evidence of such unusual histidine charge state.

Interestingly, both C_{δ} and C_{ε} peaks appear clearly at two distinct positions in the ^{13}C dimension. In the ^{1}H dimension, the C_{δ} signals exhibit slightly different values as well. This suggests the existence of two types of axial histidines with slightly different electronic structure and they are labeled as Type 1 and Type 2, respectively, in the first two columns of Table 4.1. From the intensity integration it follows that the ratio between these two types is 3:1.

Figure 4.3 presents one-dimensional ^{15}N NMR spectrum of reaction centers with $^{15}N_{\tau}$– or uniformly ^{15}N– labeled histidines. The signals between 170 and 180 ppm are assigned to pyrrole-type nitrogens with or without a hydrogen bond, respectively; signals between 250 and 260 ppm are assigned to various pyridine-type nitrogens, and finally the signal at 225 ppm can be attributed to N_{τ} of the Mg-coordinated histidines. [26,39] Interestingly, an ad-

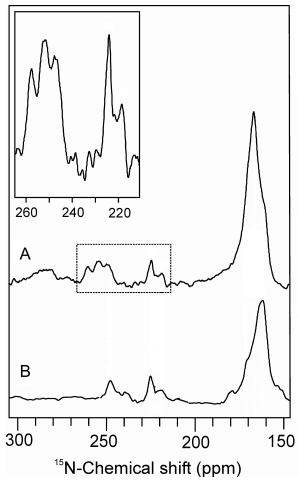

Figure 4.3: CP-MAS ^{15}N NMR spectra of uniformly ^{15}N– (A) and $^{15}N_{\tau}$– (B) histidine labeled reaction centers measured in a magnetic field of 17.6 T at 220 K. Detailed view of the region between 205 and 265 ppm is shown in the inset. Courtesy of A. Alia

ditional small peak from the Mg-coordinated N_{τ} atom is present at 220 ppm. Intensity fitting suggests, consistent with the ^{1}H-^{13}C correlation data, that there are two types of axial histidines: three resonate at 225 ppm, while the fourth one resonates with 220 ppm chemical shift. This indicates again the existence of one axial histidine with a special electronic structure different from the other three. A set of nucleus independent chemical shift (NICS) [109] calculations was performed to elucidate whether the ring current effect could be responsible for this difference. The used BChl *a* structure was the partially optimized DFT structure from model **2**, where the Mg–N_{τ} distance and Mg–N_{τ}–N1 angle are 2.184 Å and 97.70°, respectively. Additionally, several points in space with the Mg–N_{τ} distances ranging from 2.10 Å to 2.35 Å and Mg–N_{τ}–N1 angles between 90° and 105° were selected to sample various positions as the screening effect is expected to be highly anisotropic. These values correspond to typical values observed in X-ray data. [110] NICS calculations predict that the variation in the ring current shift between the different positions explored is within 0.4 ppm, therefore the observed 5 ppm upfield shift cannot be explained in terms of the ring current effect.

The DFT calculations for models **1** and **2** presented in Table 4.1 suggest

that the observed differences between Type 1 and Type 2 histidines can be explained by the presence of a strong hydrogen bond at the N_π nitrogen of the histidine. The formation of such a hydrogen bond results in polarization of the N_π–H bond towards the water molecule and higher electron density around the nitrogen. The 'excess' of electron density is then redistributed along the imidazole ring affecting all the atoms, as presented in Fig. 4.4. It can be especially seen that the ring bonds involving the N_π nitrogen are shorter. The N_τ signal is predicted to shift upfield by 3 ppm (experimentally

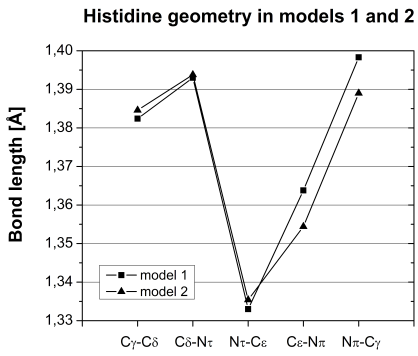

Figure 4.4: Selected bond lengths [Å] in the axial histidine models **1** and **2**.

5 ppm) and the C_δ and C_ε signal separation is slightly larger for the H-bound histidine (Table 4.1). The special histidine (Type 2) is also closer to the bacteriochlorophyll *a*, with the Mg–N_τ distance shorter by 0.034 Å compared to the other three histidines. Fig. 4.5 shows the change in the electronic density for complex **2** reflecting the polarization effects of the hydrogen-bonded water molecule. However, this does not take into account geometry changes upon hydrogen bond formation.

The results strongly suggest that the electronic structure of one of the axial histidines may be different due to the presence of a hydrogen bond at N_π. According to the crystal structure [50] two of the four axial histidines, His M202 and His L173, are within hydrogen-bonding distance to a water molecule with their N_π atoms, however, based on the data presented above

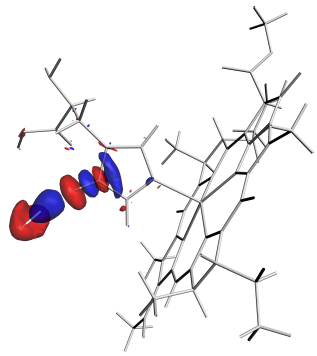

Figure 4.5: Change in electronic density reflecting the polarization effects of the hydrogen-bonding water molecule, calculated for model **2**. The isosurface value is 0.001 e/Å^3. Red corresponds to an increase of the density, as compared to the separated BChl *a*–His and water fragments, while blue denotes a decrease in the electronic density. Geometry changes upon hydrogen bond formation are not included.

it is not possible to say with certainty which of the two is the significantly different one.

4.3.2 Non-axial histidines

Apart from the four axial histidines, there are also 16 non-axial histidines present in the bacterial reaction center and 4 of them, namely His M219, His M266, His L190 and His L230, are located in the vicinity of Fe^{2+}. [50] Due to paramagnetic properties of iron, they are not visible on the spectrum in Figure 4.2. NMR signals of the remaining 12 histidines are present in the lower part of the spectrum. It is possible to partially assign the peaks using experimental data for crystalline histidines [26], however for a more complete assignment theoretical modeling is a crucial complementary tool. Therefore DFT calculations were performed for various protonation states of histidine imidazole ring and the results are presented in Table 4.2.

From the comparison with the experimental spectra it is evident that the presence of doubly deprotonated histidine can be ruled out because a very characteristic C_ε chemical shift, about 20 ppm downfield from the other forms, is not observed. Moreover, anionic histidine is energetically very unfavorable,

	C_δ	C_ε
cationic+2H_2O	124.9	130.9
cationic	122.6	132.9
neutral$_\tau$	117.9	136.0
neutral$_\pi$	134.5	137.3
anionic	133.4	154.0

Table 4.2: Calculated C_δ and C_ε chemical shifts for various protonation states of histidine.

which makes its existence highly improbable, unless some specific stabilization is provided by the protein environment, as proposed for Photosystem II. [79] The best correlation between experimental and calculated values (Fig. 4.7) shows that a large number of histidines occur in the neutral$_\tau$ form and give resonances at 113.6 (C_δ) and 134.9 (C_ε) ppm. A second group can be identified as doubly protonated histidines, which produce signals at 122.3 and 132.5 ppm for C_δ and C_ε, respectively. It is possible that some histidines are of the neutral$_\pi$ type which is predicted to resonate above 130 ppm with C_δ and C_ε signals separated by only $\sim$3 ppm. However, it is difficult to clearly distinguish them in the large group of signals visible on the spectrum in that range.

Interestingly, the calculations predict that if both N_τ and N_π nitrogens of cationic histidine are involved in hydrogen bonding, then a downfield shift of about 2.5 ppm is observed for C_δ. Thus, the peak at 125.7 ppm can be assigned to C_δ of this type of histidines with C_ε buried in the group of signals above 130 ppm. It is still a matter of debate whether the structural symmetry-breaking His L168, which is located in the close proximity of the active BChl *a*, could be attributed to the group of doubly hydrogen-bonded histidines. Mutation and FT Raman studies provided evidence that it is hydrogen bonded to Asn L166 on one side and to the 3^1 acetyl of P_L on the other side. [111,112] This, however, does not necessarily imply double protonation. To investigate this possibility, P_L, His L168 and Asn L166 were extracted from the 1M3X [50] crystal structure and two protonation models were tested. The first model contained His L168 in the neutral$_\tau$ form and the second one in the cationic form. Both of them were geometrically optimized, relaxing the histidine imidazole ring, asparagine amine and carbonyl groups, and the carbonyl group

of the bacteriochlorophyll *a* acetyl. The optimized model with His L168 in the neutral$_\tau$ form remains close to the geometry present in the crystal structure, while the orientation of Asn and His side chains changes considerably for doubly protonated His L168 (Fig. 4.6). Moreover, the X-ray data [50] displays

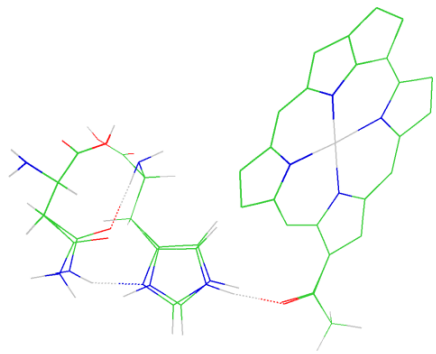

Figure 4.6: Comparison of partially optimized geometry for His L168 neutral and cationic. Relaxed atoms include histidine imidazole ring, asparagine amine and carbonyl groups and carbonyl group of the bacteriochlorophyll *a* acetyl. Representation of BChl *a* was simplified for clarity.

the asparagine amine group oriented towards the N_π nitrogen of the histidine, suggesting that His L168 is rather a hydrogen bond acceptor from the Asn L166 residue and a hydrogen bond donor to the P_L acetyl group. Therefore, this histidine can be classified to the group of neutral$_\tau$ histidines.

The shift of the remaining peak at 110.4 ppm is close to the calculated C_δ chemical shift of neutral$_\tau$ histidine, however the upfield shift cannot be explained by hydrogen bonds. Probably, a local electrostatic field of the protein is responsible for that unusual value. The overall correlation of the assignment is depicted in Figure 4.7 with a root mean square deviation of 3.6 ppm.

4.4 Conclusions

An assignment and interpretation of histidine NMR spectra in bacterial reaction centers was presented. It is established that all the axial histidines exist in the neutral$_\pi$ form and one of them has substantially different electronic

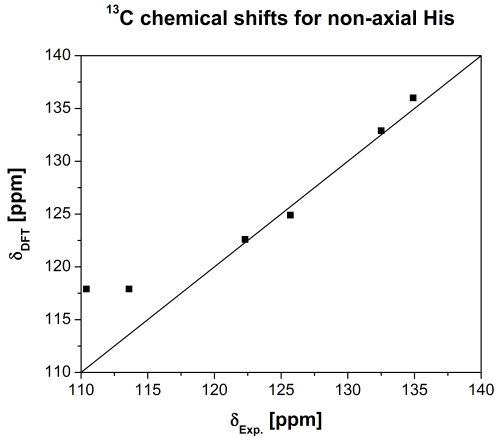

Figure 4.7: Correlation plot between calculated and experimental ^{13}C chemical shifts of non-axial histidines in bacterial reaction centers.

structure due to hydrogen-bonding with a water molecule at the N_π position. This effectively breaks the overall symmetry of those four histidines. From the presented data it is not possible to tell whether His L173 or His M202 is the distinct one but chapter **6** will revisit that problem providing further insight. The reorganization of the electronic density in the imidazole ring upon hydrogen bond formation affects all the ring atoms and is responsible for changes of their NMR chemical shifts. It is also predicted that such a special histidine is at closer distance to the Mg^{2+} than the other three. This special histidine may have a significant impact on the ground state asymmetry of the special pair, which can subsequently affect the excited state PES and thereby facilitate electron transfer and protein dynamics. This is important in view of recent progress revealing a strong role for the protein in the initial stages of the charge separation process. [113, 114] The DFT results are also used to propose an assignment of the non-axial histidines. In addition to the large number of neutral$_\tau$ histidines, two groups of cationic histidines are identified: doubly protonated and doubly protonated with hydrogen bonds at N_π and N_τ. It is not excluded that some neutral$_\pi$ histidines may be present as well. The structural symmetry-breaking histidine L168 is here identified as being of the neutral$_\tau$ type.

Chapter 5

Origin of Asymmetry in the Special Pair of Bacterial Reaction Center

5.1 Introduction

Electronic asymmetry in the special pair of BRC is believed to affect the directionality of the electron transfer process and has been therefore much studied. [53, 60–62, 104, 105] The EPR and ENDOR studies for the cation radical $P^{+\bullet}$ have shown a disproportion in spin density distribution in favor of P_L. [64,67,68,104] From the Stark experiments on the excited state P* on the other hand, it has been proposed that more electron density is concentrated on P_M. [63] It has been also reported that in the ground state there is an excess negative charge located on P_L. [53, 66]

Recently, a suggestion has been made from photo-CIDNP solid-state NMR experiments that the asymmetry, both in the electronic ground-state and in the radical cation state, is caused by an intrinsic property of the special pair supermolecule, which is attributable to a modification of the structure of P_L. [115] Moreover, differences in electronic density distribution between ground-state and radical state have been explained by polarization effects

due to the His L168 hydrogen bonded to the 3^1 acetyl group of P_L. [53, 115] However, the electrostatic interactions within the bacteriochlorophylls *a* in the special pair and with the protein environment can also play an important role in determining the structure and electronic distribution of P. This has been recently shown by Ganapathy and coworkers for the Zinc chlorin aggregates, where it was found that the self-assembly can be driven mostly by electrostatic interactions without hydrogen bonding. [116] Also recent theoretical investigations on the cation radical state of the special pair suggest that electronic asymmetry may be associated with different orientations of the phytyl tails and the methyl ester group on the $C13^2$ carbon atoms, and that the asymmetry of the spin density distribution is not caused by the distortions of the bacteriochlorophylls *a* planes. [61, 62]

Given that a detailed and consistent picture on the origin of the electronic asymmetry has not emerged yet, in this chapter it is investigated how the electronic density in the ground-state is influenced by different structural properties of the special pair bacteriochlorophylls *a*, and by their interaction with axial histidines and other neighboring residues. A particularly interesting aspect is the orientation of the P_L 3^1 acetyl group, which in the 1PCR [49] crystal structure is substantially different from all the other *Rb. sphaeroides* RC structures deposited in the Protein Structure Database. This orientation can be characterized by the C4–C3–$C3^1$–$O3^1$ dihedral angle (φ_{ac}) which equals 88° for the 1PCR structure and ranges between -2° and 21° for all the others. [111] This large difference makes the 1PCR crystal structure somewhat special and thus interesting to compare with other structures such as, for example, the 1QOV structure [117], where the dihedral angle is 13°, that is almost in the middle of the observed range. It turns out that the orientation of the 3^1 acetyl group of P_L BChl *a*, which depends on the hydrogen bond with His L168, is crucial for the electronic density distribution among the two P_L and P_M bacteriochlorophylls *a*. In this way the protein can tune the biophysical properties of the special pair by inducing conformational changes to the acetyl and therefore to the strength of conjugation with the porphyrin π system. Finally, the effects of the neighboring residues on the absorption properties of bacteriochlorophylls *a* are studied and it is shown how the lo-

calization of the molecular orbitals relevant for the Q_y excitations strongly depends on the structural properties of the BChls *a* in the special pair.

5.2 Models and Methods

Density Functional Theory calculations were performed using the ADF computational code [87–89] with the BLYP [73, 75, 76] functional and the TZP Slater-type basis set. The initial model, extracted from the 1PCR crystal structure of *Rhodobacter sphaeroides* bacterial reaction center [49], included the special pair, the two axial histidines (His L173 and His M202), two water molecules (HOH 1007 on the L-side and HOH 1051 on the M-side) and the aminoacid residues His L168, Asn L166 and Phe M197. The phytyl side chains of bacteriochlorophylls *a* were truncated to a methyl group and broken peptide bonds were saturated to a neutral amino acid termination (COOH–NH_2).

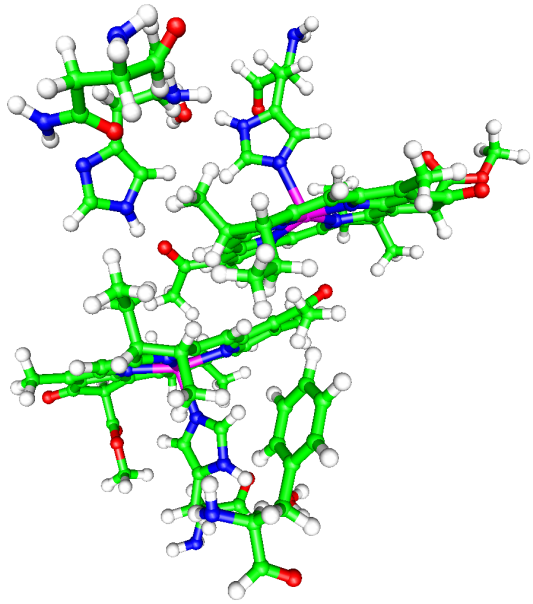

Figure 5.1: Ball and stick representation of Model **8**, the largest model considered in this study containing approximately 250 atoms.

In order to remove experimental uncertainties, the initial model was par-

tially optimized by relaxing carbons and nitrogens in the porphyrin ring, and all the hydrogen atoms (model **8**, see Fig. 5.1). In this way the x-ray crystallography errors and molecular modeling refinement artifacts were corrected by DFT, while preserving the supramolecular structure of the system due to the applied constraints. Subsequently, a series of models were built by cutting the partially optimized model into separate fragments. For an overview see Fig. 5.2. Additionally, the models **5** and **6** were partially optimized, relaxing in each of them the two imidazole rings and the two magnesium atoms.

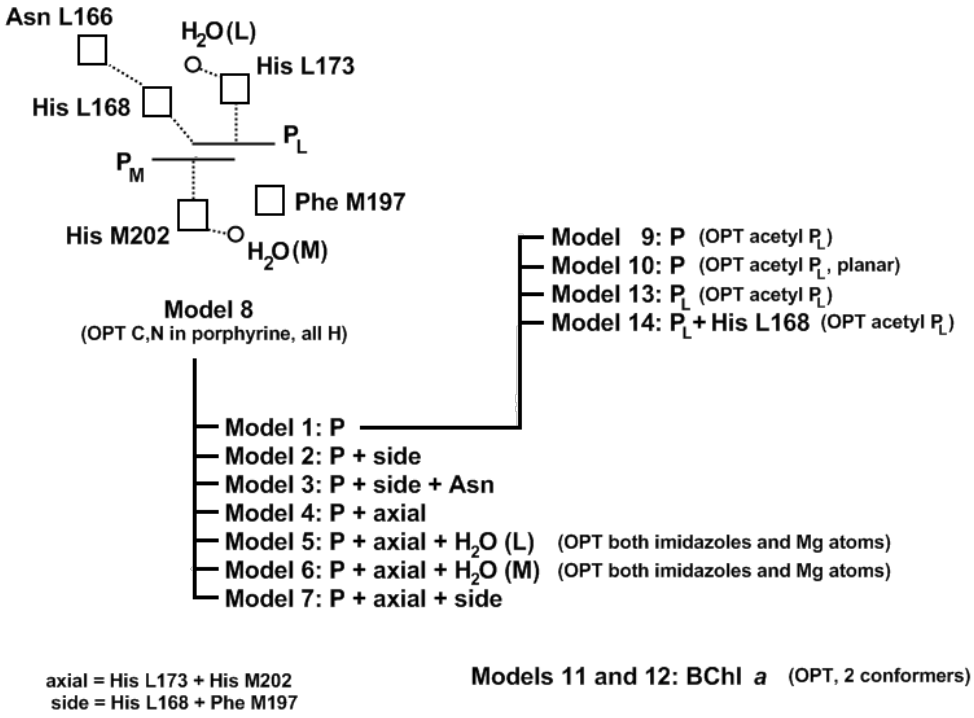

Figure 5.2: An overview of theoretical models used in this chapters. Model **8** is also shown schematically here.

To investigate the impact of the 3^1 acetyl group rotation, the special pair in model **1** was used as a starting point to create two models: **9** and **10**. In the model **10**, the P_L acetyl was additionally rotated to mimic the P_M acetyl orientation. Subsequently, the geometry of the P_L acetyl group was relaxed in both models **9** and **10**, by optimizing the positions of $C3^1$, $O3^1$ and the

$C3^2$ methyl group.

Finally, P_L and P_L+His L168 were extracted from model **1** to form models **13** and **14**, respectively. In both of these models the acetyl group of P_L was relaxed by optimizing geometrical positions of $C3^1$, $O3^1$ and the $C3^2$ methyl group. Additionally two fully optimized bacteriochlorophyll *a* molecules were constructed with different orientations of the acetyl group: one in which the $C3^2$ methyl group points towards the $C2^1$ methyl (model **11**) and one in which the acetyl carbonyl points towards the $C2^1$ methyl (model **12**).

The quadrupole derived charge analysis was performed as implemented in the ADF. [118] Electron density difference maps were calculated by subtracting from the electronic density of a model, the electronic densities of its fragments. The excitation energies were calculated using TDDFT/TZP with the "Statistical Averaging of Orbital Potentials" (SOAP) potential [119–121], which is well-suited for molecular response properties.

5.3 Results and Discussion

5.3.1 Asymmetry of the special pair

The total quadrupole derived charges for P_L and P_M in the various models described above are presented in Table 5.1. For the model **1** comprising the

Model	q^{P_L}	q^{P_M}
Model 1 – P	0.08	-0.08
Model 2 – P+side	0.06	-0.08
Model 3 – P+side+Asn	0.07	-0.08
Model 4 – P+axial	-0.02	-0.21
Model 5 – P+axial+H_2O(L)	-0.01	-0.23
Model 6 – P+axial+H_2O(M)	-0.01	-0.22
Model 7 – P+axial+side	-0.02	-0.18
Model 8 – P+axial+side+Asn+H_2O(L)+H_2O(M)	-0.02	-0.19

Table 5.1: Sum of quadrupole derived charges for P_L and P_M in various models.

special pair only, an electronic asymmetry of 0.16 electron charge between the

P_L and P_M bacteriochlorophylls *a* is found, indicating that the asymmetry is an intrinsic feature of P, at least within the model derived by the 1PCR structural data. Addition of the two side residues, His L168 and Phe M197 (model **2**) has only a minor effect on the electron density of P with a small decrease in the positive charge of P_L. One would expect that due to the hydrogen bond with the histidine His L168, the 3^1 acetyl would donate electron charge, thus making P_L more positively charged. However, as can be seen in Fig. 5.3, the hydrogen bonding induces only a small charge polarization with an increase in electronic density between N_τ and $O3^1$, but no clear net charge transfer. In Figure 5.3 the steric interaction with $C7^1$ methyl can be also observed, which can contribute to the asymmetric change.

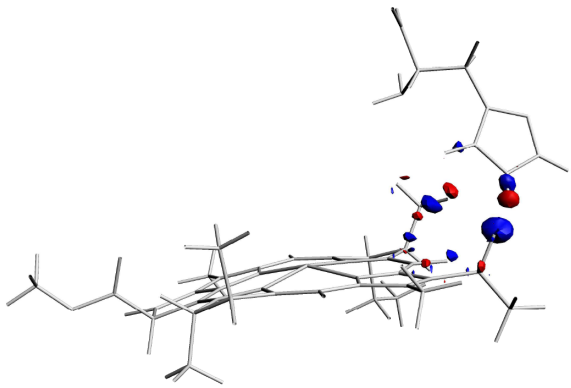

Figure 5.3: Change in the electronic density upon P_L -His L168 hydrogen bond formation. The isosurface value is 0.0012 e/Å^3. Red corresponds to an increase of the density, as compared to the separated BChl *a* and His fragments, while blue denotes a decrease in the electronic density.

Interestingly, axial histidines enhance the original asymmetry of the special pair and have a different effect on the two bacteriochlorophylls *a* (see model **4** in Table 5.1): His L173 donates a charge of 0.10 e to P_L, while His M202 donates to P_M a charge of 0.13 e. Since the charge transfer from those histidines is essentially of the same nature as for the LH2 complex (see Fig. 3.6), it also depends on the relative distance and orientation of His and BChl *a*, as described in Chapter 3, section 3.3.2. A closer look at the

orientation of the two histidines reveals that His M202 has its imidazole ring almost perpendicular to the bacteriochlorophyll *a* plane and slightly more tilted, contrary to His L173 (Table 5.2). Moreover the two histidines appear to be rotated differently around the Mg–N_τ axis.

	His L173	His M202
$\angle_{BH}$	78°	88°
C_δ –N_τ –Mg	122°	128°
N_I–Mg–N_τ –C_δ	-135°	-151°

Table 5.2: Orientation of axial histidines with the respect to ligated BChl *a* in the special pair. The $\angle_{BH}$ corresponds to the angle between C_γ –C_δ –N_τ and N_I–N_{II}–N_{III} planes. Consult Figures 1.1 and 1.5 for atom numbering.

The next two models in the Table 5.1, namely models **5** and **6**, contain a single water molecule hydrogen bonded to one of the axial histidines. It can be seen that the water has only a minor effect on the asymmetry of the special pair. It is also observed that a hydrogen bond between a water molecule and the N_π atom of axial histidine has a small effect on the histidine orientation with the respect to the bacteriochlorophyll *a* molecule. Therefore, it can be concluded that the distinct orientation of the two axial histidines is a consequence of geometrical and steric adjustments to optimize the hydrogen bonding network with the proximal protein environments, including the two water molecules. Finally, by looking at the total charges in the models **7** and **8** containing the special pair, axial and side residues, it is visible that the side residues have some polarization effect and in the largest model **8** the asymmetry between P_L and P_M is about 0.17 electron, very similar in the absolute value to the asymmetry of the special pair only. The axial histidines only shift the total charges for P_L and P_M by ≈0.1 e. The data presented in Table 5.1 show that P_M has more electron charge density than P_L in the ground state. The finding that the special pair carries a net negative charge of ≈0.2 e is consistent with SSNMR data in the ground state [53, 66, 115]. It can also be clearly concluded that this excess negative charge is mostly due to a charge transfer from the axial histidines and that the hydrogen bonded His L168 has only a minor effect. However the SSNMR data suggest

an accumulation of electron charge mostly on the pyrrole ring I of P_L and less on P_M. This appears to be in contrast with the results presented above, although one should take into account that here the total charge on the BChls *a* is calculated, while the NMR chemical shift data are available only for a limited set of carbon atoms. Therefore the experimental conclusions regarding ground state charge distribution of P_L and P_M should be taken with some care.

As discussed above, the special pair exhibits an intrinsic electronic asymmetry which must be then a feature of its geometry. Comparing P_L and P_M bacteriochlorophylls *a*, it is noticeable that the 3^1 acetyl group has substantially different orientation in the two molecules. Each of the 3^1 acetyl groups of the special pair may be oriented either with the oxygen facing outward and forming a hydrogen bond to the surrounding protein, or with the oxygen pointing inward and acting as a sixth ligand to the magnesium of the other BChl *a*. [122] There is a competition between a high conjugation with the porphyrin ring in a co-planar acetyl geometry and optimization of the electrostatic intermolecular interactions and steric repulsion in a more twisted acetyl orientation. For P_M the acetyl group is almost co-planar with the BChl *a* and thus highly conjugated with the porphyrin electronic structure, while for P_L the acetyl is out of plane and less conjugated. When the P_L acetyl group is forced almost in the plane of bacteriochlorophyll *a* (model **10**), then the electronic asymmetry of the special pair vanishes, as presented in Table 5.3.

Model	φ_{ac}	φ_{met}	q^{P_L}	q^{P_M}
Model 1	92°	-137°	0.08	-0.08
Model 9	40°	-138°	0.05	-0.05
Model 10	-173°	11°	0.00	0.00

Table 5.3: Sum of quadrupole derived charges for P_L and P_M in various models of the special pair. The φ_{ac} corresponds to the C4–C3–C3^1–O3^1 dihedral angle and the φ_{met} to the C4–C3–C3^1–C3^2 dihedral angle of P_L.

Figures 5.4 and 5.5 clearly show that when the acetyl of P_L bacteriochlorophyll *a* lies in plane, hardly any electron density difference is observed between the P_L and P_M, while when the acetyl is out of plane, the perturbation is large. The bulky $C3^2$ methyl group of the P_L acetyl penetrates the electronic cloud of the P_M bacteriochlorophyll *a* inducing a strong electronic polarization. This geometry is similar to the geometry observed for the Zinc chlorin aggregates, where it was found that the self-assembly can be driven mostly by electrostatic interactions without hydrogen bonding. [116]

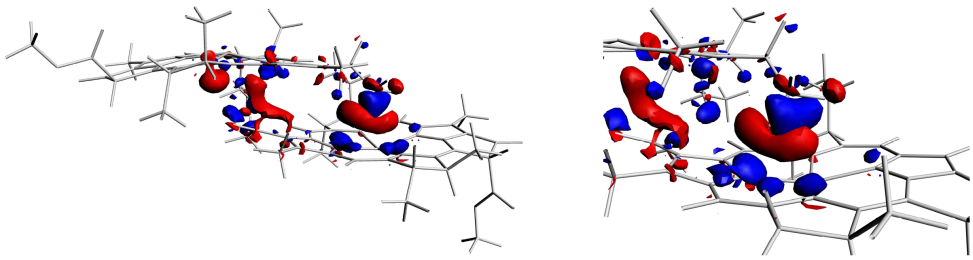

Figure 5.4: Change in the electronic density upon P_L -P_M dimer formation in model **1**. The isosurface value is 0.0012 e/Å^3. Red corresponds to an increase of the density in the complex, as compared to the separated BChl *a* fragments, while blue denotes a decrease in the electronic density. The right panel shows the P_L acetyl area in details.

This acetyl orientation may be influenced by the presence of the hydrogen-bonded His L168, as presented in Table 5.4. For the optimized bacteriochloro-

Model	φ_{ac}	φ_{met}
Model 11 – Optimized BChl *a*	0°	180°
Model 12 – Optimized BChl *a*	-179°	1°
Model 13 – P_L	27°	-151°
Model 14 – P_L+His L168	47°	-132°

Table 5.4: Orientation of the 3^1 acetyl group in single BChl *a* models. The φ_{ac} corresponds to the C4–C3–$C3^1$–$O3^1$ dihedral angle and the φ_{met} to the C4–C3–$C3^1$–$C3^2$ dihedral angle of P_L.

phyll *a* there are two in-plane acetyl conformations: In one conformer the acetyl oxygen is located on the side of the C4 atom, while in the other is

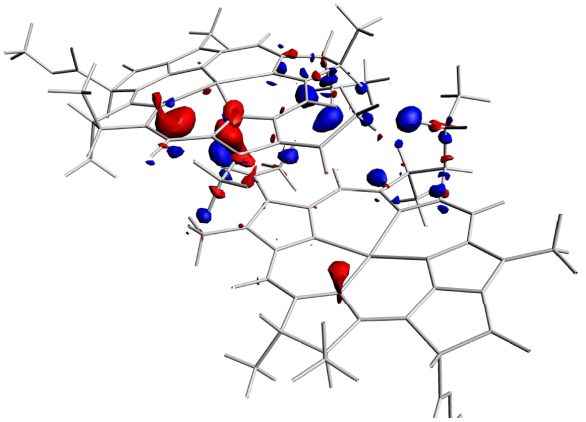

Figure 5.5: Change in the electronic density upon P_L -P_M dimer formation for model **10** (with planar P_L acetyl). The isosurface value is 0.0012 e/Å^3. Red corresponds to an increase of the density in the complex, as compared to the separated BChl *a* fragments, while blue denotes a decrease in the electronic density.

pointing towards the C2^1 methyl group. It was found that the first is lower in energy by 4 kcal/mol. When the P_L bacteriochlorophyll *a* is extracted from model **1** and its acetyl optimized, the φ_{ac} angle drops down to 27°, while if the same optimization is performed in the presence of His L168, the angle settles at 47°. Similar calculations performed for various special pair models do not provide a clear picture, as for the special pair the situation is more complex due to multiple steric, $\pi - \pi$, and electrostatic effects, particularly a competition between the P_L-His L168 hydrogen bond and Mg–O attraction. However, it is known that the formation of the hydrogen bond to His L168 forces the acetyl group of P_L to rotate out of the molecular plane. [123] Various X-ray crystallography structures report quite different values for the acetyl angle in the range between -2° and 21°. [111] Therefore at room temperature the acetyl group most likely samples a large range of orientations and first-principles molecular dynamics simulations would be more appropriate here to get a reliable statistical average of this parameter. When the hydrogen bond between His L168 and P_L is removed or its strength is altered by mutations, a change in the electron transfer kinetics is observed. [112, 124, 125]

5.3.2 Absorption properties

Bacteriochlorophyll *a* has two major absorption bands, usually referred to as Q_x and Q_y. [3]. The most intense Q_y band appears in the region 750–800 nm and the less intense Q_x band between 550 and 600 nm. Table 5.5 presents the computed TDDFT absorption spectra for the optimized BChl *a* monomer, P_L and P_M extracted from model **1**, P_L+His L173 and P_M+His M202 from model **4**, and for P_L with the 3^1 acetyl group in plane (model **10**).

Model	Q_x	Q_y
Opt BChl *a*	617	703
P_M Model **1**	612	712
P_M + His M202 Model **4**	633	716
P_L Model **1**	571	666
P_L + His L173 Model **4**	600	670
P_L Model **10**	594	695

Table 5.5: Main absorption peaks computed with TDDFT for several models including a single BChl *a*. Values are given in nm.

First of all it can be noted that the TDDFT calculated absorption bands for the optimized monomer (Opt BChl *a*) are in perfect agreement with recently published TDDFT calculations [102] but deviate from experimental values: Specifically the Q_y peak is overestimated by ≈0.15 eV while the Q_x peak is underestimated by ≈0.15 eV. These deviations are within the typical TDDFT error due to the approximation in the exchange-correlation functionals and are not of much concern since we are interested here mostly in trends and not in the exact values. The analysis of the TDDFT results shows that the dominant contribution to the Q_y absorption peak is the HOMO → LUMO transition, while the Q_x band has a strong HOMO-1 → LUMO character mixed with the HOMO → LUMO+1 to a less extent. This molecular orbitals analysis is consistent with earlier semi-empirical calculations. [126]

Figure 5.6 shows the energy of the most relevant molecular orbitals for a fully optimized bacteriochlorophyll *a*, as well as for P_L and P_M, extracted from model **1**. Interestingly, the HOMO is higher in energy in P_L than in

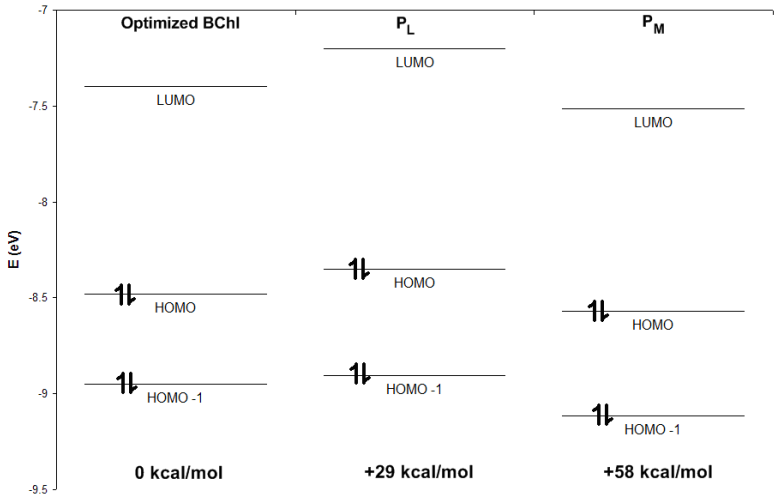

Figure 5.6: Energy levels and total bonding energies of P_L, P_M (from model **1**) and optimized bacteriochlorophyll *a*.

P_M, while the LUMO is lower in P_M than in P_L. The differences in molecular orbital energies and in the total binding energy compared with the optimized bacteriochlorophyll *a* indicate considerable distortions for the two BChls *a* in the special pair. For P_L+His L173 and P_M+His M202, both extracted from model **4**, the picture is similar (Fig. 5.7) with the HOMO being higher in energy in P_L and the LUMO being lower in P_M. These results already qualitatively indicate that a considerable charge transfer character should be expected in the excited state of P, with electronic charge moving from P_L to P_M. A $P_L{}^+P_M{}^-$ charge transfer state has been indeed suggested on the basis of absorption and Stark spectroscopy. [63, 127]

From the comparison of the main absorption peaks in Table 5.5 it can be seen how the geometrical distortions and the axial histidine affect the excitation energies, neglecting for the moment the effect of the coupling between P_L and P_M. The absorption spectrum of P_M is very similar to that of the optimized BChl *a*, while in the spectrum of P_L the two major bands Q_x and Q_y are strongly blue-shifted by about 35 nm. This shift can be rationalized on the basis of the strong out of plane orientation of the acetyl group. In fact, when the 3^1 acetyl group is rotated into the plane of P_L bacteriochlorophyll *a*

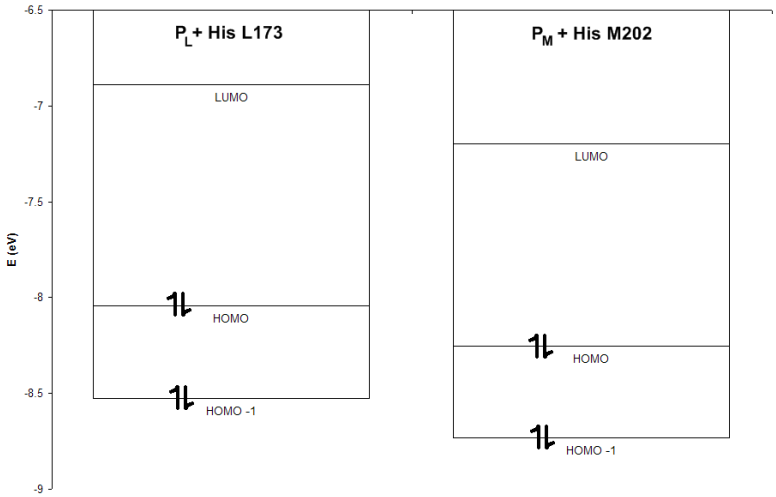

Figure 5.7: Energy levels of P_L+His L173 and P_M+His M202 from model **4**.

and optimized (model **10**), the spectrum bands shift closer to the positions of the optimized BChl *a*. The shift in Q_y band between P_L of model **1** and P_L of model **10** is consistent with ref. [126]. Therefore the orientation of the acetyl has a large influence on the electronic structure and optical properties of the whole bacteriochlorophyll *a*. When the 3^1 acetyl group is in the porphyrin plane, the electronic conjugation of the main ring extends to the acetyl, while when the acetyl group is out of plane, the conjugation weakens. For both P_L and P_M, the addition of axial histidines induces a red-shift for both bands and especially for the Q_x absorption.

We turn now our attention to the effect of electronic coupling in the BChl *a* dimer of the BRC special pair. In Figure 5.8 the HOMO of P in comparison with the HOMO of P_L extracted from model **8** is shown. Clearly the HOMO of P is almost entirely localized on P_L and is hardly affected by the dimer formation. This strong localization of the HOMO appears to be in contrast with electron spin resonance data showing that electron spin in the radical cation state is delocalized on the two BChls *a* of P. [128, 129] Also the recent photo-CIDNP data show an electron spin density distribution between P_L and P_M of about 70:30 in favor of P_L. [115] The localization of the HOMO

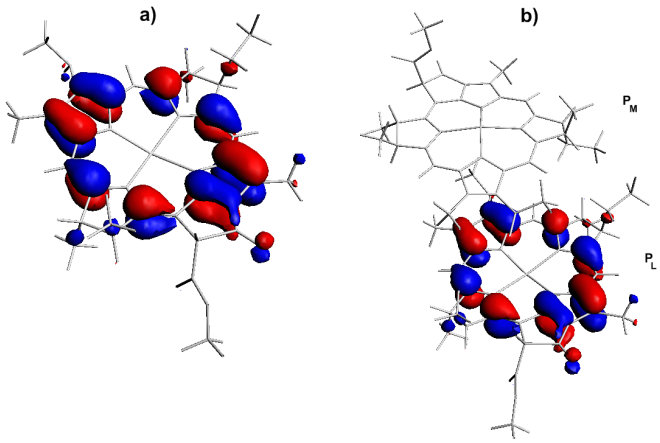

Figure 5.8: HOMO from a) P_L and b) P.

in the model **8** can be associated to the out of plane rotation of the acetyl group having a destabilizing effect on the HOMO of P_L with respect to the HOMO of P_M (see also Figure 5.6). However, when the P_L 3^1 acetyl group is rotated into the plane of bacteriochlorophyll *a* (model **10**) then both HOMO and LUMO appear to be delocalized onto the whole special pair, as presented in Fig. 5.9. Rotation of the acetyl group to a configuration close to planar increases the symmetry of the two fragments of the special pair and brings the HOMO of P_L and HOMO of P_M closer in energy, as presented in Fig. 5.10. Nevertheless, the HOMO has a larger localization on P_L, while the LUMO is more localized on P_M, indicating that a partial charge transfer character in the Q_y excitation is still present as suggested by experimental data. [63, 127]

The same calculations repeated for the special pair extracted from the 1QOV structure, which has the acetyl dihedral angle smaller, lead to similar results. Consistently with model **10**, the HOMO and LUMO orbitals were found to be delocalized over the entire special pair, but with the HOMO (LUMO) having more weight on P_L (P_M), respectively. The total quadrupole derived charges for P_L and P_M were 0.03 and -0.03, respectively. Thus, also the model of P extracted from the 1QOV structure shows an asymmetric charge distribution with P_M being more negatively charged. It can be concluded that models derived from different crystallographic structures are qualitatively con-

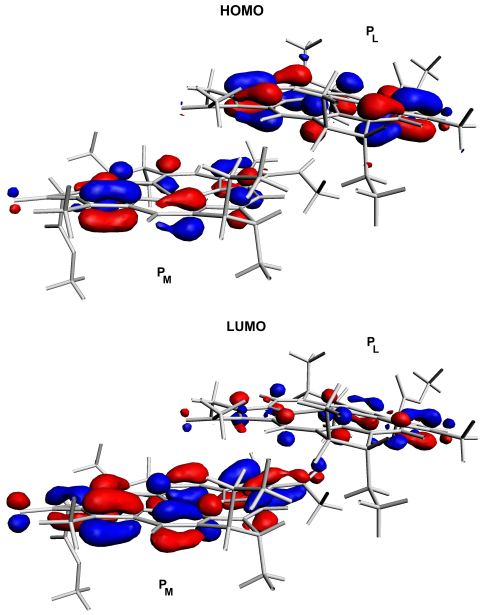

Figure 5.9: HOMO and LUMO of special pair from model **10**.

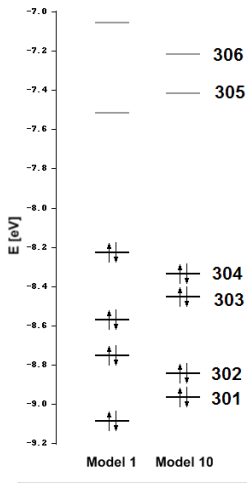

Figure 5.10: Orbital energies in special pair from models **1** and **10**.

sistent with each other, although quantitative differences are observed mostly due to the different acetyl orientation on P_L.

The absorption spectra for various models are presented in Fig. 5.11. It is evident that the Q_y band is now split due to exciton coupling in the special pair. The absorption bands consist now of several transitions with different weights as shown for model **1**. Within the supermolecule approach used here,

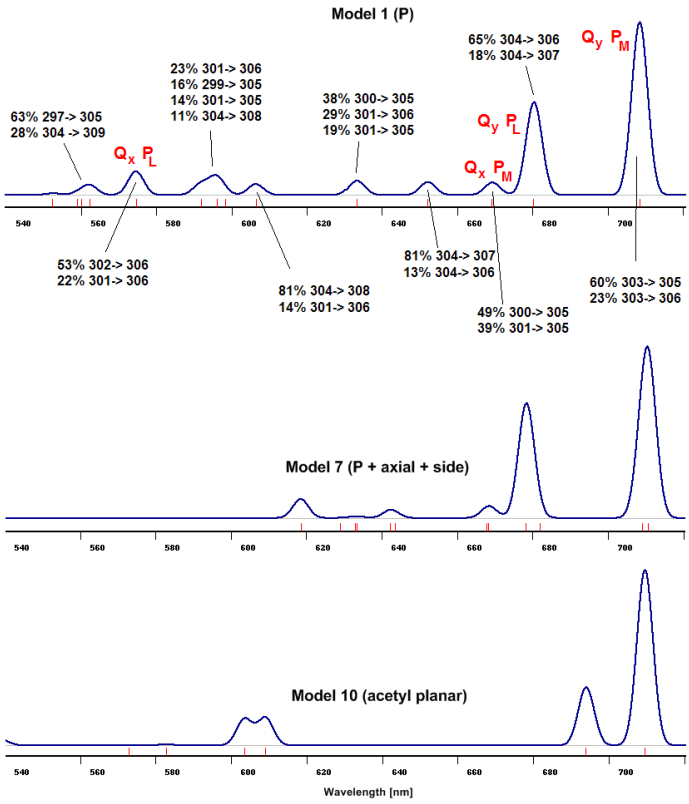

Figure 5.11: TDDFT absorption spectra of special pair models. The main contributions to the bands are indicated. Note that 304 is HOMO and 305 LUMO. The numbers indicate orbitals that mostly contribute to the transitions.

any monomeric excited state splits into two excited states upon chromophore dimerization, each with a different energy and transition dipole moment, as a direct result of exciton coupling and possibly also interchromophore charge transfer. An estimate of the exciton coupling can be calculated as the differ-

ence between the first two excitation energies. For model **1** an exciton coupling of 0.07 eV is obtained. The Q_y band splitting is only slightly increased when including the three histidines and phenylalanine (model **7**). In the model **10** containing the P_L 3^1 acetyl group rotated into the plane of bacteriochlorophyll *a*, the exciton coupling is reduced to 0.04 eV. The low-energy absorption band of the BRC is at 890 nm at 15 K and increases in energy to 860 nm at room temperature. [130] If one takes the 800 nm absorption of the monomeric BChl *a* as the value of the wavelength, at which the special pair would absorb without the pigment–pigment coupling, the shift to 890 nm corresponds to an energy shift of ≈0.15 eV. Thus, the present TDDFT calculations strongly underestimate the exciton coupling. There might be several reasons for this discrepancy, including the approximation in the functional, the neglect of long range interactions with the protein, a poor description of contributions due to charge transfer states. A detailed investigation of all these effects is beyond the scope of the present work. We refer to a recent paper by Thomas Renger and coworkers for a detailed analysis of the exciton coupling in BRC based on an effective two-state model Hamiltonian. [131]

5.4 Conclusions

An analysis of the electron charge difference between P_L and P_M bacteriochlorophylls *a* of the special pair was presented, together with a TDDFT study of the absorption properties. It is found that the electron asymmetry is an intrinsic feature of the special pair and is strongly modulated by the specific orientation of the 3^1 acetyl group, which is hydrogen bonded to His L168. Since the acetyl group can conjugate to the π electron system of BChl *a*, and this conjugation decreases in strength as the carbonyl group is rotated out of the macrocycle plane, the protein can tune the biophysical properties of the special pair by enforcing conformational changes to the acetyl. If its orientation is close to the plane of P_L, the electron density perturbation in the special pair and consequently the observed asymmetry is strongly reduced. These changes are also reflected in the absorption spectra and in the localization of the relevant molecular orbitals. When the acetyl is oriented out of

plane, significant blue shifts for the main absorption bands of bacteriochlorophyll *a* are predicted.

Although crystallographic data do not provide a precise determination of the acetyl rotation, some conclusions that are valid for models with different acetyl group orientation can be drawn: (i) both P_L and P_M BChl *a* carry a negative charge due primarily to electron charge donation by the axial histidines; (ii) the ground state electronic density is asymmetric with P_M being more negatively charged than P_L; (iii) the HOMO to LUMO electronic transition has a partial charge transfer character with electron charge moving from P_L to P_M in agreement with experimental data in the excited state; [63] (iv) increased dihedral angle for the acetyl group rotation enhances electronic asymmetry of the special pair and decreases delocalization of the molecular orbitals.

Chapter 6

General Discussion and Future Prospects: Asymmetry and Electron Transfer

The results presented in this work uncover a specific state of frustration for the Mg-coordinated histidines in the LH2 system, which is pushed closer to the corresponding BChl *a* molecule due to protein-induced steric and electrostatic stress. This results in a much larger charge transfer, which depends also on the relative orientation of the two molecules, and in an abnormal electronic configuration of the axial histidine. Differences in the relative orientation of the BChl *a*–His components between P_L-His L173 and P_M-His M202 are also responsible for an enhancement in the electron charge asymmetry in the special pair of the BRC. However, it is found that the charge asymmetry is an intrinsic property of the two bacteriochlorophylls *a* and originates from protein-induced structural distortions of the porphyrin rings and is strongly enhanced by out of plane orientation of the P_L 3^1 acetyl group. The specific orientation of the acetyl is controlled to a large extent by the hydrogen bond with His L168, although this interaction appears to be in competition with

other electrostatic and orbital energy terms. By changing the acetyl orientation the electronic, optical, and thus biophysical properties of the special pair can be tuned. It is also established that one of the four axial histidines present in the bacterial reaction center has a different electronic structure than the other three due to a hydrogen-bonded water at the N_π nitrogen. This interaction brings the coordinated histidine and the bacteriochlorophyll *a* closer.

Although the focus of this thesis was not in the electron transfer process, the presented results have interesting implications for an emerging electron transfer mechanism. It has been recently discovered that protein dynamics drives the first steps in photosynthetic charge separation [113, 114]. However, taking into account that the primary electron transfer happens on a very short time scale of ∼3 ps, there is not much time for the protein to undergo serious rearrangements. Certainly, 3 ps is enough to move one or even several protons around, leading to the concept of a proton-coupled electron transfer (PCET), where the transfer of a proton assists the electron transfer. Activation of small molecules, redox-driven proton pumps and radical initiation all involve the coupling of protons to electrons, which is the basic mechanism for bioenergetic conversion. [132] Generally, two types of PCET are distinguished: co-linear, in which both the proton and electron are transferred along the same direction and orthogonal PCET, where the proton and electron are transferred to disparate acceptors.

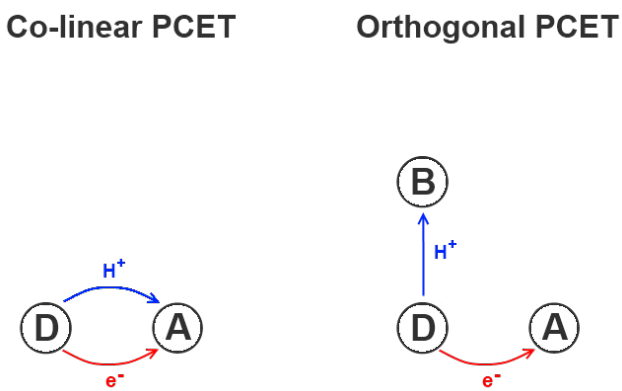

Figure 6.1: Two types of proton-coupled electron transfer.

It has been reported that the water molecule between His M202 and B_A is important for optimization of the primary electron transfer rate and that steric exclusion of that water in a mutant generates *ca.* an 8-fold decrease in the decay rate of the P* state. [133] Moreover, a hydrogen bond between the water molecule and the 13^1 carbonyl of B_A is observed in the oxidized special pair $P^{+\bullet}$ but deemed weak or nonexisting in the special pair neutral ground state. It is also suggested that a possible through-bond connection between the special pair and B_A facilitated by His M202 and the water molecule may exist. [133] Therefore, it can be temporarily assumed that the special histidine with the hydrogen bond to a water molecule found in chapter **4** is in fact His M202. If the proton transfer, or just a shift in the hydrogen bond equilibrium, had to occur first between His M202 and the associated water molecule, that histidine would gain partially anionic character and it would be stabilized by the presence of the magnesium ion. This would in turn change the relative geometry of His and BChl *a*, including shortening of the Mg–N_τ distance, and induce a larger charge transfer to the special pair (see Fig. 6.2). Interestingly,

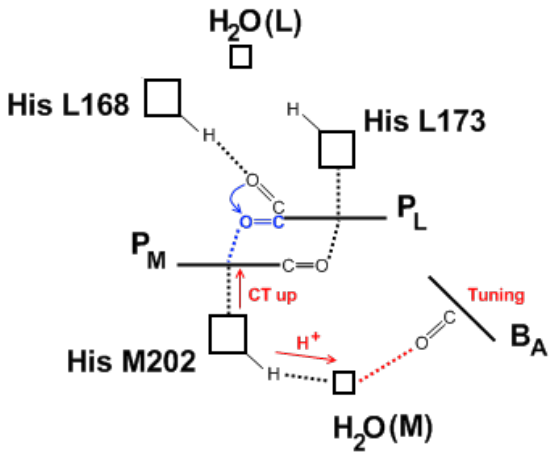

Figure 6.2: A schematic representation of the proposed proton-coupled electron transfer process in the bacterial reaction center. The red color indicates changes occurring after special pair excitation and before the electron transfer, while the blue color depicts changes taking place after the electron transfer and before the special pair reduction.

P_M is found to have more electron density than P_L both in the ground and

excited state. [63] The additional negative charge would facilitate the electron transfer from P*. On the electron acceptor, B_A, the 13^1 carbonyl is conjugated to the π electron system of its porphyrin ring. Therefore formation of a hydrogen bond with the water molecule (or H_3O^+) provides an opportunity to fine-tune the redox potential, making the accessory bacteriochlorophyll *a* easier to reduce and lowering the free energy of the $P^+B_A^-$ state. All together this would facilitate the electron transfer from P* to B_A.

In order to stabilize the positive charge on the special pair and to prevent charge recombination, the 3^1 acetyl of P_L could be rotated if enough driving force is available to break the hydrogen bond with His L168. Such a rotation will alter the electronic structure of the bacteriochlorophyll *a* dimer. Molecular dynamics simulations suggest that the acetyl rotates on oxidation, while coupled-cluster calculations on gas-phase energetics of that process indicate that *ca.* 7 kcal/mol driving force is provided by the preference of the charged BChl *a* Mg to be coordinated to the carbonyl rather than to the methyl group. [122, 134, 135] This energy is enough to break the hydrogen bond between P_L and His L168. In that respect the acetyl group would act as a valve to protect the system from too fast charge recombination. In all known reaction centers an electron moves at least one step down to acceptor chain before the oxidized primary donor is reduced.

The possibility of the above-mentioned through-bond connection between the primary electron donor and acceptor, the speculated proton transfer, and the 3^1 acetyl rotation to block recombination of the cation radical are intriguing suggestions and therefore their significance and realism should be further explored. Particularly a thorough investigation of the acetyl rotation profile and constraints, as well as the associated impact on the electronic structure of P before and after the primary electron transfer should be pursued. Finally, the proton transfer possibility and path should be addressed by employing more extensive models within the QM/MM approach.

Appendix A

Basis Set and Functional Tests

The Pople's notation is a notation most often used for Gaussian basis sets like 6–311++G(3df,3pd). The 'G' stands for Gaussian-type functions and divides the notation into two parts: functions for occupied atomic orbitals are described before 'G', while high angular momentum functions are given afterwards. '6' denotes that core orbitals are a contraction of six primitive, *i.e.* uncontracted, functions. The next three digits indicate a TZ valence split basis, in which valence orbitals are split into three functions, represented by three, one and one primitives, respectively. First '+' shows that diffuse functions are applied to the heavy atom and the second one informs that the same goes for hydrogens. In the parenthesis polarization functions are given, first for heavy atoms (three d-functions and one f-function) and then for hydrogen (three p-functions and a d-function).

Basis set tests were performed for the reference compounds (TMS, NH_3) in vacuum, using 6-311++G, 6-311++G(d,p), 6-311++G(2d,2p), 6-311++G(3df,3pd) and analogous double-zeta basis sets together with the 6-31G(d,p) without diffuse functions. The results are collected in Table A.1. Addition of diffuse functions has the largest effect on the nitrogen shielding (8.0 ppm) and influences ^{13}C and ^{1}H chemical shieldings by only 1.2 ppm and 0.6 ppm, respectively. The inclusion of polarization functions has also impor-

	NH_3		TMS	
	N	H	C	H
6-31G(d,p)	255.8	32.0	186.4	31.5
6-31++G	270.7	32.3	189.5	32.3
6-31++G(d,p)	263.8	31.4	187.6	31.4
6-31++G(2d,2p)	265.1	31.4	186.6	31.4
6-31++G(3df,3pd)	262.7	31.4	185.7	31.3
6-311++G	264.2	32.5	184.1	32.5
6-311++G(d,p)	254.8	31.8	178.6	31.7
6-311++G(2d,2p)	255.8	31.7	178.7	31.6
6-311++G(3df,3pd)	256.4	31.4	179.1	31.5

Table A.1: Basis set influence on the DFT/BLYP computed chemical shieldings [ppm] for the reference compounds.

tant effects: When going from the 6-311++G basis to the 6-311++G(d,p) basis, the chemical shieldings change by 9.4 ppm for nitrogen, 5.5 ppm for carbon and 0.8 ppm for hydrogen. Addition of polarization functions in the triple-zeta basis beyond the (d,p) set results in only small changes for all the atoms. Interestingly, the smallest basis set used here, namely 6-31G(d,p), produces values for ^{15}N close to those obtained with larger triple-zeta basis sets. This coincidence, however, may be attributed to a fortuitous error cancelation rather than to the accuracy of this particular basis.

The above-mentioned triple-zeta basis sets were also tested on histidine in all four possible protonation states of its imidazole ring and the results are reported in Table A.3. Similarly to the chemical shieldings of the reference compounds, convergence is essentially reached with the 6-311++G(d,p) basis set. Also in this case the inclusion of (d,p) polarization functions into the 6-311++G basis set has important effects, particularly for the unprotonated ring nitrogens where a chemical shift change of about 30 ppm is observed.

Table A.2 contains the chemical shifts for all the histidines using the B3LYP hybrid functional with the 6-311++G(d,p) basis set. These results show that the choice of this popular functional has a marginal effect on the chemical shifts when compared to BLYP.

	Cationic	Neutral$_\tau$	Neutral$_\pi$	Anionic
C	190.3	185.7	186.7	187.4
Cα	61.1	62.1	61.8	61.4
Cβ	34.9	40.9	32.6	48.1
Cγ	144.5	149.0	132.4	137.5
Cδ	124.0	117.2	135.6	133.4
Cε	135.9	138.6	139.3	154.2
N	47.9	49.2	53.1	36.2
Nπ	209.6	305.9	187.1	290.2
Nτ	186.1	173.8	301.9	290.8
Hδ	7.3	6.9	7.1	6.9
Hε	8.1	7.4	7.4	7.3
Hπ	14.2	–	9.1	–
Hτ	9.1	8.1	–	–
H(–Cα)	3.6	3.3	3.4	3.9
H(–Cβ)	3.2	2.9	2.9	3.4
H(–Cβ)	3.4	3.0	3.0	2.1
H(–N)	1.5	0.9	1.6	0.2
H(–N)	2.2	1.6	1.0	1.5
H(–O)	7.1	5.6	5.8	5.0

Table A.2: Histidine chemical shifts [ppm] in different protonation states calculated with B3LYP/6-311++G(d,p) level of theory. The ^{1}H and ^{13}C chemical shifts are referred to TMS, while the ^{15}N chemical shifts are related to NH_3.

	Cationic				Neutral$_\tau$				Neutral$_\pi$				Anionic			
	B1	B2	B3	B4	B1	B2	B3	B4	B1	B2	B3	B4	B1	B2	B3	B4
C	201.8	190.3	191.3	191.6	196.6	186.5	187.1	187.5	197.2	186.5	187.2	187.4	194.3	185.7	186.4	192.1
Cα	65.4	64.6	64.9	66.0	64.2	63.2	63.3	64.2	64.9	64.8	65.0	65.9	65.8	64.6	64.5	65.9
Cβ	39.7	37.2	37.2	38.2	44.4	42.5	42.0	43.4	34.5	34.3	34.0	35.3	53.3	51.7	51.3	48.9
Cγ	146.2	144.3	143.8	144.9	151.8	148.5	148.7	149.7	133.8	131.6	130.9	131.5	141.0	137.7	138.0	139.3
Cδ	125.4	122.6	121.6	122.6	120.1	117.9	116.8	116.4	137.2	134.5	134.8	135.4	136.4	133.4	133.2	131.0
Cε	135.3	132.9	131.8	132.3	139.4	136.0	135.9	137.3	140.8	137.3	137.0	138.0	159.3	154.0	154.5	154.2
N	60	54	54	53	46	44	44	44	69	62	63	62	48	42	42	51
Nπ	220	212	213	213	331	302	302	302	198	190	190	190	320	293	293	290
Nτ	195	188	188	188	182	175	176	175	332	303	302	302	323	295	294	292
Hδ	7.1	7.2	7.3	7.3	6.7	6.9	6.9	6.9	6.9	7.0	7.1	7.1	6.7	7.0	7.1	6.9
Hε	7.8	8.0	8.1	8.1	7.4	7.4	7.5	7.6	7.3	7.3	7.4	7.4	7.5	7.4	7.5	7.4
Hπ	13.1	14.2	14.9	15.3	–	–	–	–	8.6	8.9	9.2	9.3	–	–	–	–
Hτ	8.5	8.9	9.3	9.4	7.6	8.1	8.4	8.6	–	–	–	–	–	–	–	–
H(–Cα)	3.9	3.7	3.9	3.8	4.2	4.0	4.1	4.1	3.8	3.5	3.6	3.5	4.2	3.9	4.0	4.4
H(–Cβ)	3.4	3.3	3.3	3.3	3.4	3.2	3.2	3.2	3.1	3.0	3.1	3.0	3.7	3.6	3.7	3.7
H(–Cβ)	3.7	3.4	3.5	3.5	2.4	2.3	2.3	2.3	3.2	3.0	3.0	3.0	2.2	2.2	2.2	2.4
H(–N)	1.8	1.7	1.7	1.7	1.4	1.3	1.4	1.5	1.4	1.2	1.3	1.4	1.7	1.7	1.8	0.8
H(–N)	2.5	2.2	2.2	2.3	0.9	0.7	0.7	0.8	2.0	1.8	1.8	1.9	0.6	0.3	0.4	0.5
H(–O)	7.8	7.2	7.4	7.5	6.3	5.8	6.1	6.2	6.4	5.8	6.0	6.2	5.4	4.9	5.2	5.4

Table A.3: Histidine chemical shifts [ppm] in different protonation states calculated with DFT/BLYP and various basis sets. B1, B2, B3 and B4 correspond to 6-311++G, 6-311++G(d,p), 6-311++G(2d,2p) and 6-311++G(3df,3pd) basis set, respectively. The ^{1}H and ^{13}C chemical shifts are referred to TMS, while the ^{15}N chemical shifts to NH_3.

Summaries

Summary

When in 1780 the English chemist Joseph Priestley was performing his famous experiment with a mint plant and a burning candle enclosed in a glass jar, he was probably not aware of the importance of the process he was going to discover. Now, 230 years later, we know a lot more about photosynthesis, but still many details, like the origin of the functional asymmetry in bacterial reaction centers, remain unknown. A detailed understanding of those processes may provide a significant insight as to the nature and functioning mechanism of the solar energy conversion machinery. This knowledge will be beneficial for the development of artificial photosynthetic devices, which would facilitate the solution of the global energy problem. The work presented in this thesis focuses on the functional asymmetry and the role of bacteriochlorophylls *a*–protein interactions in the bacterial reaction center and light-harvesting complex II, providing a basis for building a model of the electron transfer process.

Specifically, the aim of this thesis is to investigate interactions between bacteriochlorophylls *a* and neighboring residues, mostly histidines, both in the LH2 and BRC systems in order to address the open questions regarding the nature of BChl *a*–His complexes and asymmetry of the special pair. The electronic structure of the special pair may be perturbed both in the ground and excited states by proximal histidines, facilitating thereby the asymmetric electron transfer along one of the protein branches. Since histidine properties and activity depend on the imidazole ring nitrogens, it is crucial to know their

exact protonation state, which is generally hard to derive from structural data. Also it is important to gain a deeper insight into the electronic structure of BChl *a*–His complexes, especially in view of recent experiments revealing a rather unusual behavior for the histidyl residues in the LH2 complex. To reach these goals molecular modeling tools based on quantum chemistry and in particular on density functional theory are used. An introduction to the theoretical approach is given in chapter **2**.

The study presented in chapter **3** revolves around NMR chemical shifts for various protonation states of histidine imidazole ring and presents an investigation of, among others, the neutral$_\pi$ and anionic species, which have not been widely studied so far. The bacteriochlorophyll *a*–histidine complexes in the LH2 system are also analyzed in detail. It is found that due to protein-induced steric and electrostatic stress, the Mg-coordinated histidines are pushed closer to the corresponding BChl *a* molecules, thereby inducing a much larger charge transfer. This charge transfer is found to depend on the distance between the two species and their relative orientation. As a result, the imidazole ring of the axial His residues is in a frustrated state much different from the formal neutral$_\pi$. These results clarify the unusual behavior observed experimentally for some histidyl residues in the LH2 complex.

The following two chapters shift the focus to the special pair of the bacterial reaction center. Since both bacteriochlorophylls *a* of the special pair form, similarly to LH2, a BChl *a*–His complex with the N$_\tau$ nitrogen of histidine, the knowledge of His protonation states is crucial. Therefore, chapter **4** concentrates on the protonation state assignment for the axial and non-axial histidines in BRC. It is established that the four axial ones are neutral with the N$_\pi$ atom protonated. Interestingly, one of them has a special electronic structure which is different from the other three due to the presence of a hydrogen-bonded water at the N$_\pi$ nitrogen. This interaction causes a reorganization of electron density within the imidazole ring, in turn inducing the coordinated histidine and bacteriochlorophyll *a* to come closer. Based solely on these results it is however difficult to establish whether His L173 or His M202 is the "special" one, as both have a water molecule in the vicinity of the N$_\pi$ nitrogen.

Finally, chapter **5** shows that the electronic asymmetry is an intrinsic property of the special pair and is strongly modulated by the specific orientation of the 3^1 acetyl group of P_L bacteriochlorophyll *a*. When out of plane, the bulky P_L acetyl group penetrates heavily the P_M electronic density inducing the asymmetry, which can be neutralized by rotation of the P_L acetyl into the bacteriochlorophyll *a* plane. The orientation of the group is forced and maintained by the hydrogen bond with His L168. Changes in the acetyl orientation are reflected in the absorption spectrum and in the localization of the relevant molecular orbitals and therefore, the biophysical properties of the special pair can be tuned in this way. It is also found that the P_M BChl *a* has consequently a larger electron density that P_L, and that the asymmetry is slightly enhanced by the axial histidines due to differences in their relative orientation with the respect to the corresponding bacteriochlorophylls *a*.

In chapter **6** the results described in the previous parts are used to propose a model for the primary electron transfer based on a proton-coupled electron transfer mechanism. It involves proton transfer or a shift in the hydrogen bond equilibrium between His M202 and the nearby water molecule, which would cause the histidine to attain a partially negative character. A new hydrogen bond between the water molecule and the 13^1 carbonyl of B_A would be then formed. Subsequent fine tuning of the B_A redox potential through the 13^1 carbonyl, as well as charge transfer and shortening of the His M202–P_M distance, would facilitate the electron transfer from P* to B_A. Next, as a consequence of the charged BChl *a* preference to be coordinated to the carbonyl rather than to the methyl group, the 3^1 acetyl of P_L would rotate breaking the hydrogen bond with His L168. This rotation would effectively stabilize the positive charge on the special pair and prevent charge recombination. In that respect the acetyl group would act as a valve for that process.

Samenvatting

Toen de Engels chemicus John Priestley in 1870 zijn beroemde experiment uitvoerde met een muntplant en een brandende kaars opgesloten in een glazen pot, was hij zich waarschijnlijk niet bewust van het belang van het proces dat

hij zou gaan ontdekken. Nu, 230 jaar later, weten we veel meer van de fotosynthese, maar nog steeds zijn er veel details onbekend, zoals de oorsprong van de functionele asymmetrie in bacteriele reactie centra. Een gedetailleerd begrip van die processen geeft mogelijk een belangrijk inzicht in de natuur en functie van de zonne-energie conversie machinerie. Deze kennis zal ten goede komen aan de ontwikkeling van kunstmatige fotosynthetische apparaten, wat de oplossing voor het globale energie probleem zou faciliteren. Het werk gepresenteerd in dit proefschrift is gericht op de functionele asymmetrie en de rol van de bacteriochlorofyll *a*–eiwit interacties in het bacteriele reactiecentrum en licht-antenne complex 2, om zo een basis te leggen voor een model voor het proces van electron overdracht.

In het bijzonder is het doel van dit proefschrift om interacties tussen bacteriochlorofyllen *a* en naburige residuen, met name histidines, te bestuderen in LH2 en BRC systemen, om zo de open vragen te beantwoorden aangaande de natuur van BChl *a*–His complexen en de asymmetrie van het speciale paar. De electronische structuur van het speciale paar zou verstoord kunnen zijn in zowel de grond- als in de aangeslagen toestanden door naburige histidines en zo de asymmetrische electron overdracht faciliteren langs één van de eiwit takken. Aangezien de eigenschappen en activiteit van histidines afhangen van de imidazool ring stikstoffen, is het cruciaal om hun exacte geprotoneerde toestand te weten, welke in het algemeen moeilijk te halen valt uit structurele data. Ook is het belangrijk om een beter inzicht te verkrijgen in de electronische structuur van BChl *a*–His complexen, vooral in het kader van recente experimenten die een nogal ongebruikelijk gedrag tonen voor de histidyl residuen in het LH2 complex. Om deze doelen te bereiken zijn moleculaire modelering-middelen toegepast, die gebaseerd zijn op de quantum chemie en in het bijzonder op dichtheids-functionaaltheorie. Een inleiding in de theoretische benadering wordt gegeven in hoofdstuk **2**.

De studie gepresenteerd in hoofdstuk **3** gaat over NMR chemische verschuivingen voor verschillende protonatietoestanden van de histidine imidazool ring en presenteert een onderzoek naar, onder andere, de neutral$_\pi$ en anionische variant, die tot dusver niet wijdverbreid onderzocht zijn. De bacteriochlorofyll *a*–histidine complexen in het LH2 systeem zijn ook in detail geana-

lyseerd. Er is gevonden dat door eiwit-geinduceerde en electrostatische stress, de Mg-gecoordineerde histidines dichter tegen de corresponderende BChl *a* moleculen aangedrukt worden, waardoor een veel grotere ladingsoverdracht ontstaat. Deze ladingsoverdracht blijkt af te hangen van de afstand tussen de twee species alsmede hun relatieve orientatie. Als resultaat bevindt de imidazool ring van de axiale His residueen zich in een gefrustreerde toestand die erg verschilt van de formele neutral$_\pi$. Deze resultaten verklaren het ongewone gedrag wat voor sommige histidyl residueen in het LH2 complex experimenteel is waargenomen.

De volgende twee hoofdstukken verschuiven het focus naar het speciale paar van het bacterieel reactiecentrum. Aangezien beide bacteriochlorofyllen *a* van het speciale paar een BChl *a*–His complex vormen met de N$_\tau$ stikstof van histidine, net als in LH2, is kennis van de His protonatie-toestanden cruciaal. Daarom concentreert hoofdstuk **4** zich op de toekenning van de protonatie-toestand van de axiale en non-axiale histidines in het BRC. Er is vastgesteld dat de vier axiale histidines neutraal zijn met het N$_\pi$ atoom geprotoneerd. Interessant is dat één van hen een speciale electronische structuur heeft, die afwijkt van de drie anderen, door de aanwezigheid van een waterstof-gebonden water aan de N$_\pi$ stikstof. Deze interactie veroorzaakt een reorganisatie van de electronendichtheid binnen de imidazool ring, waardoor vervolgens de gecoordineerde histidine en bacteriochlorofyll *a* dichter bij elkaar komen te zitten. Slechts op deze resultaten gebaseerd, is het moeilijk om vast te stellen of His L173 danwel His M202 de "speciale" histidine is, aangezien beide een water molecuul hebben in de buurt van de N$_\pi$ stikstof.

Hoofdstuk **5** tenslotte laat zien dat de electronische asymmetrie een intrinsieke eigenschap is van het speciale paar en sterk gemoduleerd wordt door de specifieke orientatie van de 3^1 acetyl groep van P$_L$ bacteriochlorofyll *a*. Wanneer hij uit het vlak ligt, dringt de omvangrijke P$_L$ acetyl groep zwaar door in de P$_M$ electronendichtheid, hierbij de asymmetrie veroorzakend, die geneutraliseerd kan worden door rotatie van de P$_L$ acetyl in het vlak van de bacteriochlorofyll *a*. De orientatie van de groep wordt geforceerd en onderhouden door de waterstof brug met His L168. Veranderingen in de rotatie van de acetyl zijn gereflecteerd in het absorptie spectrum en in de plaatsing

van de relevante moleculaire orbitalen. Daarom kunnen de biofysische eigenschappen van het speciale paar op deze manier afgestemd worden. Er is ook gevonden dat de P_M BChl *a* als gevolg hiervan een grotere electronendichtheid heeft dan P_L en dat de asymmetrie enigszins versterkt wordt door de axiale histidines, door verschillen in hun relatieve orientatie ten opzichte van de corresponderende bacteriochlorofyllen *a*.

In hoofdstuk **6** worden de resultaten beschreven in de vorige delen gebruikt om een model te presenteren voor de primaire electron overdracht, gebaseerd op een proton-gekoppeld electron-overdracht mechanisme. Het betreft proton overdracht of een verschuiving in het waterstof brug-evenwicht tussen His M202 en het nabij gelegen watermolecuul, waardoor de histidine een partieel negatief ladingskarakter krijgt. Daardoor wordt een nieuwe waterstof brug gevormd tussen het watermolecuul en de 13^1 carbonyl van B_A. De daaropvolgende fijn-afstemming van de B_A redox potentiaal door de 13^1 carbonyl, alsmede de ladingsoverdracht en het verkleinen van de His M202–P_M afstand, vergemakkelijken de electron overdracht van P* naar B_A. Vervolgens zal de 3^1 acetyl van P_L draaien en de waterstof brug met His L168 verbreken, vanwege de voorkeur van het geladen BChl *a* om gecoordineerd te zijn naar de carbonyl, meer dan naar de methyl groep. Deze rotatie zal effectief de positieve lading op het speciale paar stabiliseren en ladingsrecombinatie voorkomen. In dat opzicht zou de acetyl groep als een ventiel voor dat proces functioneren.

Streszczenie

Kiedy w 1780 roku angielski chemik Joseph Priestley przeprowadzał swoje pionierskie doświadczenie z gałązką mięty i zamkniętą w szklanym słoju palącą się świecą, najprawdopodobniej nie był świadomy znaczenia procesu który odkryje. Obecnie, 230 lat później, nasza wiedza o fotosyntezie jest znacznie większa, jednak wciąż wiele szczegółów, jak na przykład źródło pochodzenia funkcjonalnej asymetrii w fotosyntetycznym centrum reakcji bakterii (BRC), pozostaje nieznanych. Szczegółowe zrozumienie tych zagadnień może przenieść znaczący wgląd w naturę i mechanizm funkcjonowania procesu przemiany energii słonecznej. Ta wiedza przyczyni się do rozwoju urządzeń przeprowa-

dzających fotosyntezę w sposób sztuczny, co być może ułatwi rozwiązanie globalnego problemu energetycznego. Badania zawarte w niniejszej rozprawie są skupione na funkcjonalnej asymetrii i roli oddziaływań pomiędzy bakteriochlorofilem *a* (BChl *a*) a białkiem w centrum reakcji bakterii i w kompleksie LH2, dając podstawy do stworzenia modelu wyjaśniającego proces przeniesienia elektronu.

W szczególności celem niniejszej dysertacji jest zbadanie oddziaływań pomiędzy bakteriochlorofilem *a* i sąsiadującymi resztami aminokwasowymi, głównie histydynowymi, w kompleksach LH2 i BRC, w celu rozwiania wątpliwości dotyczących natury kompleksów BChl *a*–His i asymetrii specjalnej pary. Struktura elektronowa specjalnej pary może być zaburzona przez sąsiadujące reszty histydynowe zarówno w stanie podstawowym jak i w stanie wzbudzonym, ułatwiając w ten sposób asymetryczne przeniesienie elektronu wzdłuż jednej z dwóch gałęzi białka. Ponieważ aktywność i właściwości histydyny zależą od atomów azotu w pierścieniu imidazolowym, znajomość ich dokładnego stanu protonowego jest niezbędna. Jednakże zazwyczaj jest on trudny do określenia na podstawie danych strukturalnych. Ponadto, ważne jest, aby uzyskać dokładniejszy wgląd w strukturę elektronową kompleksów BChl *a*–His, zwłaszcza w świetle ostatnich doświadczeń pokazujących dość nietypowe zachowanie histydyn w kompleksie LH2. Do osiągnięcia powyższych celów wykorzystano metody modelowania molekularnego oparte na chemii kwantowej, a w szczególności na teorii funkcjonałów gęstości. Krótkie omówienie podejścia teoretycznego jest przedstawione w rozdziale drugim.

Badania zaprezentowane w rozdziale trzecim koncentrują się na przesunięciach chemicznych NMR różnych stanów protonacyjnych pierścienia imidazolowego histydyny, między innymi formy anionowej oraz neutralnej$_\pi$, które do tej pory nie były zbyt powszechnie badane. Szczegółowej analizie poddano również kompleksy bakteriochlorofilu *a* z histydyną w LH2. Okazuje się, że z powodu sterycznego i elektrostatycznego oddziaływania wywołanego sąsiadującym białkiem, histydyny skoordynowane z atomami magnezu są wypychane bliżej poszczególnych molekuł bakteriochlorofilu *a*, powodując tym samym większe przeniesienie ładunku. Jego wielkość zależy również od odległości pomiędzy tymi dwoma molekułami i od ich wzajemnej orientacji.

W rezultacie, pierścień imidazolowy osiowej histydyny jest w stanie zaburzonym, który różni się znacznie od formalnego stanu neutralnego$_\pi$. Wyniki te wyjaśniają nietypowe zachowanie niektórych histydyn w kompleksie LH2.

W kolejnych dwóch rozdziałach uwaga została skupiona na specjalnej parze centrum reakcji bakterii. Znajomość stanu protonacyjnego histydyn ma tutaj kluczowe znaczenie, ponieważ tworzą one kompleksy z bakteriochlorofilami *a* pary specjalnej przy udziale azotu N$_\tau$, podobnie jak ma to miejsce w kompleksie LH2. Dlatego też w rozdziale czwartym skoncentrowano się na ustaleniu stanów protonacyjnych osiowych i nieosiowych histydyn w centrum reakcyjnym bakterii. Okazuje się, że cztery osiowe histydyny znajdują się w stanie neutralnym, a protonowanym atomem jest atom azotu N$_\pi$. Co ciekawe, jedna z histydyn ma specjalny stan elektronowy, odmienny od pozostałych trzech, ze względu na obecność wiązania wodorowego pomiędzy atomem azotu N$_\pi$, a pobliską cząsteczką wody. To oddziaływanie wywołuje zmianę w rozkładzie gęstości elektronowej pierścienia imidazolowego, co z kolei powoduje zbliżenie histydyny i skoordynowanego z nią bakteriochlorofilu *a*. Jednakże bazując wyłącznie na tych wynikach trudno jest ustalić, która z histydyn, His L173 czy His M202, posiada ten specjalny stan elektronowy, ponieważ obie mają cząsteczkę wody w sąsiedztwie azotu N$_\pi$.

W rozdziale piątym pokazano, że asymetria elektronowa jest wewnętrzną właściwością pary specjalnej i jest silnie modulowana przez specyficzną orientację grupy 3^1 acetylowej P$_L$ bakteriochlorofilu *a*. Znajdując się poza płaszczyzną, obszerna grupa acetylowa P$_L$ znacząco penetruje gęstość elektronową P$_M$ powodując asymetrię, która może być zneutralizowana poprzez obrót grupy acetylowej P$_L$ do płaszczyzny bakteriochlorofilu *a*. Orientacja tej grupy jest wywołana i utrzymywana poprzez wiązanie wodorowe z His L168. Zmiany tej orientacji znajdują odzwierciedlenie w widmie absorpcyjnym oraz w położeniu stosownych orbitali molekularnych, umożliwiając tym samym regulację właściwości biofizycznych pary specjalnej. Okazuje się także, że P$_M$ bakteriochlorofil *a* ma większą gęstość elektronową niż P$_L$, a asymetria jest nieznacznie zwiększana przez osiowe histydyny z powodu różnic w ich położeniu względem odpowiadającym im bakteriochlorofilom *a*.

W rozdziale szóstym wyniki opisane w poprzednich rozdziałach zostały użyte do zaproponowania modelu pierwotnego przeniesienia elektronu, opartego na mechaniźmie transferu eletronu sprzężonego z przeniesieniem protonu. Według zaproponowanego modelu, przeniesienie protonu lub przesunięcie równowagi wiązania wodorowego pomiędzy His M202 a pobliską cząsteczką wody spowodowałoby przyjęcie przez histydynę częściowego ujemnego charakteru. Następnie powstałoby nowe wiązanie wodorowe pomiędzy ową cząsteczką wody a grupą 13^1 karbonylową B_A. Dostrojenie potencjału redox B_A poprzez grupę 13^1 karbonylową oraz przeniesienie ładunku i skrócenie odległości pomiędzy His M202 i P_M ułatwiłoby przeniesienie elektronu z P* do B_A. Ponieważ naładowany bakteriochlorofil *a* preferuje koordynacje z grupą karbonylową a nie metylową, grupa 3^1 acetylowa P_L obróciłaby się doprowadzając do zerwania wiązania wodorowego z His L168. Rotacja ta efektywnie ustabilizowałaby dodatni ładunek na parze specjalnej i zapobiegłaby jego rekombinacji. Tym samym grupa acetylowa odgrywałaby rolę zaworu w tym procesie.

Curriculum Vitae

In October 1999, after *cum laude* graduation from I Liceum Ogólnokształcące in Jastrzębie Zdrój I started chemistry studies at the University of Wrocław. Right from the beginning I chose to follow additional teacher training offered as optional integration into the chemistry programme. Starting from second year of studies, I was a researcher trainee under guidance of Dr. Sławomir Berski in the Theoretical Modeling of Chemical Processes Group led by Prof. Dr. Zdzisław Latajka. Also from the second year until graduation, I was receiving University of Wrocław Scientific Scholarship granted for study results. In winter 2002/2003 I spent five months in the Solid State Spectroscopy and Photochemistry group of Prof. Markku Räsänen as Socrates/Erasmus student, doing a research project under supervision of Doc. Dr. Jan Lundell on interactions between formic acid and argon. After coming back to Poland, I continued this work in the group of Prof. Latajka with Dr. Jarosław J. Panek and Doc. Dr. Jan Lundell as supervisors. The project evolved into three publications in scientific journals and Master Thesis *"Formic Acid Complex with Noble Gases: an Ab Initio Quantum Theory Approach"*. In June 2004, I defended the thesis and graduated from the University of Wrocław with M.Sc. degree in chemistry.

In October 2004 I started my Ph.D. project in the Solid-State NMR group at the Leiden University, under guidance of Dr. Francesco Buda and Prof. Dr. Huub J.M. de Groot. During this time I participated in a number of scientific and management courses. These include *"Photophysics, Photochemistry and Photobiology"* (2007) in Amsterdam; *"Winter School on Theoretical Chemistry and Spectroscopy"* (2004, 2005) in Han-sur-Lesse; *"Molecular*

Modeling and the workshop on Computational Photochemistry and Photobiology" (2005) in Amsterdam and *"Self-Organization and the Transition to Life"* (2004) in Leiden. I had lots of opportunities to be on the other side of a classroom as well, assisting in practica of *Molecular Modeling* (2005–2008) and various sorts of *Quantum Chemistry* (2005–2006) and *Computational Chemistry* (2006) courses. I had an opportunity to present my work on many international conferences and meetings through posters and oral communications. Notably, I was one of the speakers at *"Progress in ab initio modeling of biomolecules: methods and applications"* workshop held in 2006 in Leiden and *"Winter School on Theoretical Chemistry and Spectroscopy 2005"* in Han-sur-Lesse. The poster presentations include among others the meetings: *"CBB Workshop Clean Solar Fuels"* (2008) in Amsterdam; *"Solar Energy and Artificial Photosynthesis"* (2007) in London and *"Multi-scale modeling: Electrons, Molecules and (Bio)Materials"* (2006) in Amsterdam. I had also pleasure to be the chairman of SSNMR group seminar series (2007–2008) and Ph.D. representative for the group staff board (2008–2009).

List of Publications

"Origin of Asymmetry in the Special Pair of Bacterial Reaction Center"
P.K. Wawrzyniak, M. Beerepoot, H.J.M. de Groot, F. Buda
manuscript submitted to Phys. Chem. Chem. Phys.

"Hydrogen-bonded water enhances the electron charge donation in bacteriochlorophyll-histidine complexes of bacterial reaction centers"
P.K. Wawrzyniak, H.J.M. de Groot, F. Buda
manuscript submitted to Photosynth. Res.

"NMR secondary shifts of a light-harvesting 2 complex reveal local backbone perturbations induced by its higher-order interactions"
A. Pandit, P.K. Wawrzyniak, A.J. van Gammeren, F. Buda, S. Ganapathy, H.J.M. de Groot
Biochem., 2010, 49, 478–486

"Differential charge polarization of axial histidines in bacterial reaction centers balances the asymmetry of the special pair"
A. Alia, P.K. Wawrzyniak, G.J. Janssen, F. Buda, J. Matysik, H.J.M. de Groot
J. Am. Chem. Soc., 2009, 131, 9626–9627

"Zinc chlorins for artificial light-harvesting, self-assemble into antiparallel stacks forming a microcrystalline solid-state material"
S. Ganapathy, S. Sengupta, P.K. Wawrzyniak, V. Huber, F. Buda, U. Baumeister, F. Würthner, H.J.M. de Groot
Proc. Natl. Acad. Sci. USA, 2009, 106, 11472–11477

"Alternating syn-anti bacteriochlorophylls form concentric helical nanotubes in chlorosomes"
S. Ganapathy, G.T. Oostergetel, P.K. Wawrzyniak, M. Reus, A. Gomez Maqueo Chew, F. Buda, E.J. Boekema, D.A. Bryant, A.R. Holzwarth, H.J.M. de Groot
Proc. Natl. Acad. Sci. USA, 2009, 106, 8525–8530

"Protein-induced geometric constraints and charge transfer in bacteriochlorophyll-histidine complexes in LH2"
P.K. Wawrzyniak, A. Alia, R.G. Schaap, M.M. Heemskerk, H.J.M. de Groot, F. Buda
Phys. Chem. Chem. Phys., 2008, 10, 6971–6978

"Electronic structure of axial histidines in photosynthetic reaction centres of Rhodobacter sphaeroides"
A. Alia, P.K. Wawrzyniak, F. Buda, J. Matysik, H.J.M. de Groot
Photosynth. Res., 2007, 91, 146–147 (Proceedings of the 14^{th} International Congress of Photosynthesis, Glasgow, UK, July 2007)

"Interaction energy decomposition analysis for formic acid complexes with argon and krypton atoms"
J.J. Panek, P.K. Wawrzyniak, Z. Latajka, J. Lundell
Chem. Phys. Lett., 2006, 417, 100–104

"Molecular simulations of formic acid"
J. Lundell, S. Jolkkonen, M. Saarelainen, P.K. Wawrzyniak, J. Panek, Z. Latajka

CSC Report on Scientific Computing in Finland 2004–2005, Fagerholm, Puska, Åström, Blomqvist, Forsström, Jukka, Kotila, Laine, Miettinen, Tarus and Tissari (Eds.); CSC, 2005, pp. 101–105
ISBN: 952-5520-04-8 (Print), 952-5520-05-6 (PDF)

"On the nature of bonding in HCOOH...Ar and HCOOH...Kr complexes"
P.K. Wawrzyniak, J. Panek, J. Lundell, Z. Latajka
J. Mol. Model., 2005, 11, 351–361

"Theoretical study of the complex between formic acid and argon"
P.K. Wawrzyniak, J. Panek, Z. Latajka, J. Lundell
J. Mol. Struct., 2004, 691, 115–122 and J. Mol. Struct., 2004, 704, 297–304

Afterword

Here I am, sitting in the library in the night writing the last words to the thesis. When I look back in time over those years spent in Leiden, I clearly see how blind I was. During that tremendous journey, with lots of turns, ups and downs and detours, I have been confronted with many challenges of various nature. From today's perspective I see clearly a shortcut, a straight line connecting then and now. But I guess this is the purpose of a Ph.D. — to learn about the world, people and yourself. I am convinced I have learnt a lot and that time, albeit difficult, has not been wasted.

This thesis would not have been written without a constant support of my beloved wife Marzena. Your understanding, patience and warm words gave me the necessary hope in the worst moments of resignation and doubts. I also appreciate your cheerful joy which you shared with me for each good news I was bringing home. Thank you so much for everything you have done for me, this thesis is largely your merit. Next warm words go to our daughter Julia, who being only 2 years old cannot read them now, but I am pretty sure will enjoy them one day. Julia, I feel guilty I sometimes had to stay at work until late and could not kiss you for good night or that I was not in a mood to play. I very much admire your understanding and your efforts to make me smiling. I promise you that when all this is over, all three of us will take a long holidays to enjoy time together.

Then my thoughts go to my parents and sister. Mamo, Tato, dziękuję Wam za Waszą miłość i wsparcie. Pomimo dzielącego nas dystansu tysiąca kilometrów byliście obecni w naszym życiu i mogliśmy razem z Wami wspólnie przeżywać radości i smutki, a to jest bardzo ważne. Dziękuję również za

wszystkie pomocne rady i Waszą troskę. Ania, thanks for your love and friendship. I am glad that we can share our life with you and I am very grateful for all your help and frequent visits, even though you are very busy with your own Ph.D. You are the best sister ever. Kocham Was bardzo!

I would not be here right now without my curiosity for exploring the surrounding world. This interest, and especially the interest in chemistry, originates from the extraordinary attitude of my parents that have put a lot of energy into my uprising. Also, several other people helped to cultivate this gift and I would like to thank them here.

Chciałbym podziękować nauczycielom z lat szkolnych i uniwersyteckich za wiedzę i umiejętności, które mi przekazali. Jestem szczególnie wdzięczny Barbarze Kołton oraz Stanisławie Jeż za rozwój mojego zainteresowania chemią, Marzenie Tyszeckiej za wspaniałe lekcje życia i stymulację w realizacji marzeń oraz Lechowi Bernasiowi za wkład w moją edukację informatyczną.

Obviously, I cannot forget about the great friends Łukasz and Arek who accompanied my university times. We had hundreds ideas per second and together we made many crazy things, having fun but also establishing some unusual traditions at our department. That was extremely enjoyable time and that is why I miss every second of the student life. But more importantly, our discussions in Jaszczurka supported by large amounts of beer and subsequent tradition of the Thursday's Dinners with additional presence of Kuba, kept the excitement with science on a high level.

My adventure with the professional science started with the theoretical group at the University of Wrocław, which adopted me almost at the beginning of my studies. I would like to express my gratitude, especially to Jarek, Aneta, Andrzej, Sławek, Krzysiek, Agnieszka and Prof. Latajka, for all the valuable advices packed additionally with incredible amount of humor. Thank you for this opportunity; it was a very remarkable time for me. Then a milestone point was my stay in Helsinki, where I met Jan and Ermelinda. Jan, I am very grateful for your coaching, patience, generosity and all the other good things that I have experienced. Ermelinda, thanks for your discussions, advices and all the fun we have had. All together you helped me to make a final decision to pursue the Ph.D. studies.

During my first days in Leiden I was confronted with rainy and windy Dutch weather but also with kind hospitality of Ania and Tomek, who helped me to feel like at home. Being initially accommodated at the 400-years old house of Mrs. Tweehuysen, a very generous and helpful lady, I had a great opportunity not only to feel welcome but also to learn about the Dutch culture and history. At the university the friendly and vigorous company of Anna, Swapna, Shipra, Prashant, Geerten, Esha, Eugenio and Rob blended me quickly into the social life of the group. Thanks for making my first months here so nice.

Francesco, your professionalism and knowledge but also understanding and empathy helped me to successfully arrive to the end and saved the research from ending in a blind street. I very much appreciate your scientific curiosity, which makes you a true scientist who enjoys what he does and does what he enjoys. This is how I always envision science - as a passionate journey of a passionate man to understand the world we live in. It is actually a pity that there are not so many of those left in today's world. Huub, your valuable comments regarding all the manuscripts and this thesis have been of great help. I appreciate your constant commitment to improve the quality and impact of our work.

Especially, working with Swapna and Anjali gave me lots of fun. I enjoyed our discussions and the thrill of excitement as new parts of stories were unfolding. Additionally, I am grateful that Anjali agreed to translate the thesis summary into Dutch. I am also glad to had such good students. Mattijs, Roland and Maarten — you all worked very hard and gave a significant contribution to my project. I am very happy and proud that your names appear already in research papers. An important support has also came from Mark and Roar of the theoretical group, who were solving technical issues on the computing clusters in minute time. Finally, I would like to acknowledge Jörg for the possibility of observing him in a classroom. That was a very stimulating experience to learn from such a remarkable teacher.

Working in the multicultural and diverse environment of the SSNMR and BOF groups, the NMR and TOA units, and the undergraduate students was a true experience. Every single person (too many to list all of them here)

has its own contribution to my memories and all together, the present and former members, created an interesting group of people. I have spent most of the time at the department with Karthick and Thierry in our LCP 2 office. It was great to share various tips, talk about hobbies and future plans or just simply enjoy our magic drawer full of sweets. I liked very much our drinking sessions and jokes, as this resembled me the university times. And despite the office being off the main pathway, Niels used to visit us frequently, what was a great addition to the team. Niels, we have spent many hours on memorable and interesting discussions about nearly everything and they were very stimulating. It was also handful to exchange our experiences, frustrations and victories, and to support each others on the way towards the degree.

As in each profession, also in science bureaucracy and administration occupies a significant position. Going through number of forms and procedures was relatively easy due to the help of Liesbeth and Esther. I was amazed with your ability to handle the things and to push them quickly over the counter. Also many things were possible because of the help from Trudie, Arjan and Paul who were always smiling and positive about the future. Separate acknowledgements go to Jan for introducing me to a wonderful world of IVAO.aero. This has definitely elevated my interest in aviation to a new dimension. I hope we will still meet many times on the European sky and traditionally I wish you an equal number of take-offs and landings.

Last but not least, I would like to thank all my friends from the "outside" of the university. I especially owe big thanks to Przemek for keeping me alive by constantly updating me about lots and lots of interesting topics, which went a bit aside during my work here. Throughout our long friendship you were always able to provide simple solutions for difficult problems and your ability to see things from different than mine perspective was very useful during some of the hard moments here. I am grateful for your support and interest, and I do hope that ND will come back to its glory one day. Also Edyta and Karol were a sure source of a nice company and we have spent some valuable time with you, loaded with tons of jokes and laugh. Lots of inspiration comes as well from the family of Renata, Piotrek and Maciek. Thanks for all the good time together.

Bibliography

[1] L. Stryer *Biochemistry;* W.H. Freeman and Co.: New York, 1998.

[2] A.J. Hoff, J. Deisenhofer *Phys. Reports* **1997,** *287,* 1.

[3] R.E. Blankenship *Molecular Mechanisms of Photosynthesis;* Wiley-Blackwell: Oxford, 2002.

[4] D.A. Bryant, Ed.; *The Molecular Biology of Cyanobacteria;* Kluwer Academic Press: Dordrecht, 1994.

[5] R.E. Blankenship, M.T. Madigan, C.E. Bauer, Eds.; *Anoxygenic Photosynthetic Bacteria;* Kluwer Academic Press: Dordrecht, 1995.

[6] S.A. Krupenko, A.P. Vlasov, C. Wagner *J. Biol. Chem.* **2001,** *276,* 24030.

[7] L. Banci, M. Benedetto, I. Bertini, R. Del Conte, M. Piccioli, M.S. Viezzoli *Biochem.* **1998,** *37,* 11780.

[8] C.N. Fuhrmann, B.A. Kelch, N. Ota, D.A. Agard *J. Mol. Biol.* **2004,** *338,* 999.

[9] L.E. Dardenne, A.S. Werneck, M.D. Neto, P.M. Bisch *Proteins-Structure Function and Genetics* **2003,** *52,* 236.

[10] B. Vallone, K. Nienhaus, A. Matthes, M. Brunori, G.U. Nienhaus *Proc. Natl. Acad. Sci. USA* **2004,** *101,* 17351.

[11] A.V. Giri, S. Anishetty, P. Gautam *BMC Bioinf.* **2004,** *5,* 127.

[12] A.S. Lipton, R.W. Heck, P.D. Ellis *J. Am. Chem. Soc.* **2004,** *126,* 4735.

[13] Z.D. Zhang, E.A. Komives, S. Sugio, S.C. Blacklow, N. Narayana, N.H. Xuong, A.M. Stock, G.A. Petsko, D. Ringe *Biochem.* **1999,** *38,* 4389.

[14] A.G. Harrison *Mass Spectrom. Rev.* **1997,** *16,* 201.

[15] W.F. Reynolds, I.R. Peat, M.H. Freedman, J.R. Lyerla *J. Am. Chem. Soc.* **1973,** *95,* 328.

[16] T.H. Huang, W.W. Bachovchin, R.G. Griffin, C.M. Dobson *Biochem.* **1984,** *23,* 5933.

[17] A. Ramamoorthy, C.H. Wu, S.J. Opella *J. Am. Chem. Soc.* **1997,** *119,* 10479.

[18] Y.F. Wei, A.C. de Dios, A.E. McDermott *J. Am. Chem. Soc.* **1999,** *121,* 10389.

[19] T. Gajda, B. Henry, J.J. Delpuech *J. Chem. Soc. Perkin Trans* **1994,** *2,* 157.

[20] N. Shimba, H. Takahashi, M. Sakakura, I. Fujii, I. Shimada *J. Am. Chem. Soc.* **1998,** *120,* 10988.

[21] N.T. Saraswathi, M. Vijayan *Acta Cryst.* **2001,** *B57,* 842.

[22] R.M. Day, C.J. Thalhauser, J.L. Sudmeier, M.P. Vincent, E.V. Torchilin, D.G. Sanford, C.W. Bachovchin, W.W. Bachovchin *Protein Sci.* **2003,** *12,* 794.

[23] W.W. Bachovchin, J.D. Roberts *J. Am. Chem. Soc.* **1978,** *100,* 8041.

[24] W.W. Bachovchin *Proc. Natl. Acad. Sci. USA* **1985,** *82,* 7948.

[25] J.L. Sudmeier, E.M. Bradshaw, K.E. Coffman Haddad, R.M. Day, C.J. Thalhauser, P.A. Bullock, W.W. Bachovchin *J. Am. Chem. Soc.* **2003,** *125,* 8430.

[26] Alia, J. Matysik, C. Soede-Huijbregts, M. Baldus, J. Raap, J. Lugtenburg, P. Gast, H.J. van Gorkom, A.J. Hoff, H.J.M. de Groot *J. Am. Chem. Soc.* **2001,** *123,* 4803.

[27] M.S. Solum, K.L. Altmann, M. Strohmeier, D.A. Berges, Y.L. Zhang, J.C. Facelli, R.J. Pugmire, D.M. Grant *J. Am. Chem. Soc.* **1997,** *119,* 9804.

[28] J. Elguero, C. Marzin, A. Katritzky, P. Linda *The Tautomerism of Heterocycles;* Academic Press: New York, 1976.

[29] M. Munowitz, W.W. Bachovchin, J. Herzfeld, C.M. Dobson, R.G. Griffin *J. Am. Chem. Soc.,* **1982,** *104,* 1192.

[30] F. Blomberg, W. Maurer, H. Rüterjans *J. Am. Chem. Soc.* **1977,** *99,* 8149.

[31] S. Farr-Jones, W.Y.L. Wong, W.G. Gutheil, W.W. Bachovchin *J. Am. Chem. Soc.* **1993,** *115,* 6813.

[32] G.F. Signorini, R. Chelli, P. Procacci, V. Schettino *J. Phys. Chem. B* **2004,** *108,* 12252.

[33] H. Günther *NMR-Spektroskopie;* Georg Thieme Verlag: Stuttgart, 1992.

[34] D. Canet *NMR-Konzepte und Methoden;* Springer-Verlag: Berlin, 1994.

[35] J. Evans *Biological NMR Spectroscopy;* Oxford University Press: Oxford, 1995.

[36] V. Cherezov, J. Clogston, M.Z. Papiz, M. Caffrey *J.Mol.Biol.* **2006,** *357,* 1605.

[37] M.Z. Papiz, S.M. Prince, T. Howard, R.J. Cogdell, N.W. Isaacs *J. Mol. Biol.* **2003,** *326,* 1523.

[38] G. McDermott, S.M. Prince, A.A. Freer, A.M. Hawthornthwaite-Lawless, M.Z. Papiz, R.J. Cogdell, N.W. Isaacs *Nature* **1995,** *374,* 517.

[39] Alia, J. Matysik, I. de Boer, P. Gast, H.J. van Gorkom, H.J.M. de Groot *J. Biol. NMR* **2004,** *28,* 157.

[40] S.S. Kidambi, D.K. Lee, A. Ramamoorthy *Inorg. Chem.* **2003,** *42,* 3142.

[41] G.D. Scholes, I.R. Gould, R.J. Cogdell, G.R. Fleming *J. Phys. Chem. B* **1999,** *103,* 2543.

[42] X. Hu, K. Schulten *Phys. Today* **1997,** 28.

[43] X Hu, A. Damjanovic, T. Ritz, K. Schulten *Proc. Natl. Acad. Sci. USA* **1998,** *95,* 5935.

[44] V. Novoderezhkin, M. Wendling, R. van Grondelle *J. Phys. Chem. B* **2003,** *107,* 11534.

[45] V.I. Novoderezhkin, D. Rutkauskas, R. van Grondelle *Biophys. J.* **2006,** *90,* 2890.

[46] W. Nitschke, A.W. Rutherford *Trends Biochem. Sci.* **1991,** *16,* 241.

[47] R.E. Blankenship *Photosynth. Res.* **1992,** *33,* 91.

[48] T.O. Yeates, H. Komiya, A. Chirino, D.C. Rees, J.P. Allen, G. Feher *Proc. Natl. Acad. Sci. USA* **1988,** *85,* 7993.

[49] U. Ermler, G. Fritzsch, S.K. Buchanan, H. Michel *Structure* **1994,** *2,* 925.

[50] A. Camara-Artigas, D. Brune, J.P. Allen *Proc. Natl. Acad. Sci. USA* **2002,** *99,* 11055.

[51] M.C. Wakeham, M.R. Jones *Biochem. Soc. Trans.* **2005,** *33,* 851.

[52] J.L. Martin, J. Breton, A.J. Hoff, A. Migus, A. Antonetti *Proc. Natl. Acad. Sci. USA* **1986,** *83,* 957.

[53] S. Prakash, Alia, P. Gast, H.J.M. de Groot, G. Jeschke, J. Matysik *Biochem.* **2007,** *46,* 8953.

[54] M. Volk, G. Aumeier, T. Langenbacher, R. Feick, A. Ogrodnik, M.E. Michel-Beyerle *J. Phys. Chem. B* **1998,** *102,* 735.

[55] A. Holzwarth, M. Muller *Biochem.* **1996,** *35,* 11820.

[56] A. Ogrodnik, W. Keupp, M. Volk, G. Aumeier, M.E. Michel-Beyerle *J. Phys. Chem.* **1994,** *98,* 3432.

[57] A.G. Yakovlev, A.C. Shkuropatov, V.A. Shuvalov *FEBS Lett.* **2000,** *466,* 209.

[58] O.A. Gopta, D.A. Cherepanov, W. Junge, A.Y. Mulkidjanian *Proc. Natl. Acad. Sci. USA* **1999,** *96,* 13159.

[59] W. Zinth, J. Wachtveitl *Chem. Phys. Chem.* **2005,** *6,* 871.

[60] E. Daviso *The solid state photo-CIDNP effect,* Thesis, Leiden University, 2008.

[61] H. Yamasaki, H. Nakamura, Y. Takano *Chem. Phys. Lett.* **2007,** *447,* 324.

[62] H. Yamasaki, Y. Takano, H. Nakamura *J. Phys. Chem. B* **2008,** *112,* 13923.

[63] L.J. Moore, H.L. Zhou, S.G. Boxer *Biochem.* **1999,** *38,* 11949.

[64] F. Lendzian, M. Huber, R.A. Isaacson, B. Endeward, M. Plato, B. Bönigk, K. Möbius, W. Lubitz, G. Feher *Biochim. Biophys. Acta* **1993,** *1183,* 139.

[65] T.A. Mattioli, A. Hoffmann, B. Robert, B. Schrader, M. Lutz *Biochem.* **1991,** *30,* 4648.

[66] E.A.M. Schulten, J. Matysik, Alia, S. Kiihne, J. Raap, J. Lugtenburg, P. Gast, A.J. Hoff, H.J.M. de Groot *Biochem.* **2002,** *41,* 8708.

[67] J. Rautter, F. Lendzian, W. Lubitz, S. Wang, J.P. Allen *Biochem.* **1994,** *33,* 12077.

[68] W. Lubitz, F. Lendzian, R. Bittl *Acc. Chem. Res.* **2002,** *35,* 313.

[69] V. Palaniappan, P.C. Martin, V. Chynwat, H.A. Frank, D.F. Bocian *J. Am. Chem. Soc.* **1993,** *115,* 12035.

[70] M.G. Zysmilich, A. McDermott *J. Am. Chem. Soc.* **1994,** *116,* 8362.

[71] M.G. Zysmilich, A. McDermott *J. Am. Chem. Soc.* **1996,** *118,* 5867.

[72] R.G. Parr, W. Yang *Density-Functional Theory of Atoms and Molecules;* Oxford University Press: USA, 1994.

[73] A.D. Becke *Phys. Rev. A* **1988,** *38,* 3098.

[74] J.P. Perdew *Phys. Rev. B* **1986,** *33,* 8822.

[75] C.T. Lee, W.T. Yang, R.G. Parr *Phys. Rev. B* **1988,** *37,* 785.

[76] B. Miehlich, A. Savin, H. Stoll, H. Preuss *Chem. Phys. Lett.* **1989,** *157,* 200.

[77] A.D. Becke *J. Chem. Phys.* **1993,** *98,* 5648.

[78] M.A.L. Marques, C.A. Ullrich, F. Nogueira, A. Rubio, K. Burke, E.K.U. Gross, Eds.; *Time-Dependent Density Functional Theory;* Springer: Berlin, 2006.

[79] A. Diller, E. Roy, P. Gast, H.J. van Gorkom, H.J.M. de Groot, C. Glaubitz, G. Jeschke, J. Matysik, A. Alia *Proc. Natl. Acad. Sci. USA* **2007,** *104,* 12767.

[80] M.J. Frisch, G.W. Trucks, H.B. Schlegel, G.E. Scuseria, M.A. Robb, J.R. Cheeseman, J.A. Montgomery Jr., T. Vreven, K.N. Kudin, J.C. Burant, J.M. Millam, S.S. Iyengar, J. Tomasi, V. Barone, B. Mennucci, M. Cossi, G. Scalmani, N. Rega, G.A. Petersson, H. Nakatsuji, M. Hada, M. Ehara, K. Toyota, R. Fukuda, J. Hasegawa, M. Ishida, T. Nakajima, Y. Honda, O. Kitao, H. Nakai, M. Klene, X. Li, J.E. Knox, H.P. Hratchian, J.B. Cross, C. Adamo, J. Jaramillo, R. Gomperts, R.E. Stratmann, O. Yazyev, A.J. Austin, R. Cammi, C. Pomelli,

J.W. Ochterski, P.Y. Ayala, K. Morokuma, G.A. Voth, P. Salvador, J.J. Dannenberg, V.G. Zakrzewski, S. Dapprich, A.D. Daniels, M.C. Strain, O. Farkas, D.K. Malick, A.D. Rabuck, K. Raghavachari, J.B. Foresman, J.V. Ortiz, Q. Cui, A.G. Baboul, S. Clifford, J. Cioslowski, B.B. Stefanov, G. Liu, A. Liashenko, P. Piskorz, I. Komaromi, R.L. Martin, D.J. Fox, T. Keith, M.A. Al-Laham, C.Y. Peng, A. Nanayakkara, M. Challacombe, P.M.W. Gill, B. Johnson, W. Chen, M.W. Wong, C. Gonzalez, J.A. Pople Gaussian 03, Revision C.02, Gaussian, Inc., Wallingford CT, 2004.

[81] J.C. Facelli *J. Phys. Chem. B* **1998,** *102,* 2111.

[82] R. McWeeny *Phys. Rev.* **1962,** *126,* 1028.

[83] R. Ditchfield *Mol. Phys.* **1974,** *27,* 789.

[84] K. Wolinski, A.J. Sadlej *Mol. Phys.* **1980,** *41,* 1419.

[85] K. Wolinski, J.F. Hinton, P. Pulay *J. Am. Chem. Soc.* **1990,** *112,* 8251.

[86] T. Michael Duncan *Principal Components of Chemical Tensors: A Compilation;* Farragut Press: 1997.

[87] G. te Velde, F.M. Bickelhaupt, S.J.A. van Gisbergen, C. Fonseca Guerra, E.J. Baerends, J.G. Snijders, T. Ziegler *J. Comput. Chem.* **2001,** *22,* 931.

[88] C. Fonseca Guerra, J.G. Snijders, G. te Velde, E.J. Baerends *Theor. Chem. Acc.* **1998,** *99,* 391.

[89] ADF2007.01, SCM, Theoretical Chemistry, Vrije Universiteit, Amsterdam, The Netherlands, http://www.scm.com.

[90] N.T. Saraswathi, M. Vijayan *Acta Cryst.* **2002,** *B58,* 734.

[91] V.H. Vilchiz, R.E. Norman, S.C. Chang *Acta Cryst.* **1996,** *C52,* 696.

[92] P. Edington, M.M. Harding *Acta Cryst.* **1974,** *B30,* 204.

[93] K.L. Anderson-Altmann, C.G. Phung, S. Mavromoustakos, Z.W. Zheng, J.C. Facelli, C.D. Poulter, D.M. Grant *J. Phys. Chem.* **1995,** *99,* 10454.

[94] J.C. Facelli, R.J. Pugmire, D.M. Grant *J. Am. Chem. Soc.* **1996,** *118,* 5488.

[95] J.Z. Hu, J.C. Facelli, D.W. Alderman, R.J. Pugmire, D.M. Grant *J. Am. Chem. Soc.* **1998,** *120,* 9863.

[96] M.B. Ferraro, V. Repetto, J.C. Facelli *Solid State NMR* **1998,** *10,* 185.

[97] J.C. Facelli *J. Biomolec. Struct. & Dynamics* **1998,** *3,* 619.

[98] C.R. Jacob, L. Visscher *J. Chem. Phys.* **2006,** *125,* 194104.

[99] J. Schmidt, A. Hoffmann, H.W. Spiess, D. Sebastiani *J. Phys. Chem. B* **2006,** *110,* 23204.

[100] S. Komin, C. Gossens, I. Tavernelli, U. Rothlisberger, D. Sebastiani *J. Phys. Chem. B* **2007,** *111,* 5225.

[101] L. Limantara, S. Sakamoto, Y. Koyama, H. Nagae *Photochem. Photobiol.* **1997,** *65,* 330.

[102] J. Neugebauer *J. Phys. Chem. B* **2008,** *112,* 2207.

[103] A. Pandit, P.K. Wawrzyniak, A.J. van Gammeren, F. Buda, S. Ganapathy, H.J.M. de Groot *manuscript in preparation* .

[104] J.P. Allen, J.M. Cordova, C.C. Jolley, T.A. Murray, J.W. Schneider, N.W. Woodbury, J.C. Williams, J. Niklas, G. Klihm, M. Reus, W. Lubitz *Photosynth. Res.* **2009,** *99,* 1.

[105] P. Kanchanawong, M.G. Dahlbom, T.P. Treynor, J.R. Reimers, N.S. Hush, S.G. Boxer *J. Phys. Chem. B* **2006,** *110,* 18688.

[106] J.O. Goldsmith, B. King, S.G. Boxer *Biochem.* **1996,** *35,* 2421.

[107] A.R. Khatypov, A.Y. Khmelnitskiy, M.M. Leonova, L.G. Vasilieva, V.A. Shuvalov *Photosynth. Res.* **2008,** *98,* 81.

[108] P.K. Wawrzyniak, A. Alia, R.G. Schaap, M.M. Heemskerk, H.J.M. de Groot, F. Buda *Phys. Chem. Chem. Phys.* **2008,** *10,* 6971.

[109] Z. Chen, C.S. Wannere, C. Corminboeuf, R. Puchta, P. von Ragué Schleyer *Chem. Rev.* **2005,** *105,* 3842.

[110] A.W. Roszak, A.T. Gardiner, N.W. Isaacs, R.J. Cogdell *Biochem.* **2006,** *46,* 2909.

[111] D. Spiedel, A.W. Roszak, K. McKendrick, K.E. McAuley, P.K. Fyfe, E. Nabedryk, J. Breton, B. Robert, R.J. Cogdell, N.W. Isaacs, M.R. Jones *Biochim. Biophys. Acta* **2002,** *1554,* 75.

[112] A. Ivancich, T.A. Mattioli, K. Artz, S. Wang, J.P. Allen, J.C. Williams *Biochem.* **1997,** *36,* 3027.

[113] H. Wang, S. Lin, J.P. Allen, J.C. Williams, S. Blankert, C. Laser, N.W. Woodbury *Science* **2007,** *316,* 747.

[114] H. Lee, Y.C. Cheng, G.R. Fleming *Science* **2007,** *316,* 1462.

[115] E. Daviso, S. Prakash, A. Alia, P. Gast, J. Neugebauer, G. Jeschke, J. Matysik *Proc. Natl. Acad. Sci. USA* **2009,** *106,* 22281.

[116] S. Ganapathy, S. Sengupta, P.K. Wawrzyniak, V. Huber, F. Buda, U. Baumeister, F. Würthner, H.J.M. de Groot *Proc. Natl. Acad. Sci. USA* **2009,** *106,* 11472.

[117] K.E. McAuley, P.K. Fyfe, J.P. Ridge, N.W. Isaacs, R.J. Cogdell, M.R. Jones *Proc. Natl. Acad. Sci. USA* **1999,** *96,* 14706.

[118] M. Swart, P.Th. van Duijnen, J.G. Snijders *J. Comp. Chem.* **2001,** *22,* 79.

[119] P.R.T. Schipper, O.V. Gritsenko, S.J.A. van Gisbergen, E.J. Baerends *J. Chem. Phys.* **2000,** *112,* 1344.

[120] O.V. Gritsenko, P.R.T. Schipper, E.J. Baerends *Chem. Phys. Lett.* **1999,** *302,* 199.

[121] O.V. Gritsenko, P.R.T. Schipper, E.J. Baerends *Int. J. Quantum Chem.* **2000,** *76,* 407.

[122] J.M. Hughes, M.C. Hutter, J.R. Reimers, N.S. Hush *J. Am. Chem. Soc.* **2001,** *123,* 8550.

[123] J. Rautter, F. Lendzian, C. Schulz, A. Fetsch, M. Kuhn, X. Lin, J.C. Williams, J.P. Allen, W. Lubitz *Biochem.* **1995,** *34,* 8130.

[124] H.A. Murchison, R.G. Alden, J.P. Allen, J.M. Peloquin, A.K.W. Taguchi, N.W. Woodbury, J.C. Williams *Biochem.* **1993,** *32,* 3498.

[125] T.A. Mattioli, J.C. Williams, J.P. Allen, B. Robert *Biochem.* **1994,** *33,* 1636.

[126] E. Gudowska-Nowak, M.D. Newton, J. Fajer *J. Phys. Chem.* **1990,** *94,* 5795.

[127] D.J. Lockhart, S.G. Boxer *Proc. Natl. Acad. Sci. USA* **1988,** *85,* 107.

[128] J.R. Norris, R.A. Uphaus, H.L. Crespi, J.J. Katz *Proc. Natl. Acad. Sci. USA* **1971,** *68,* 625.

[129] J.R. Norris, H. Scheer, M.E. Druyan, J.J. Katz *Proc. Natl. Acad. Sci. USA* **1974,** *71,* 4897.

[130] H. Huber, M. Meyer, M. Scheer, W. Zinth, J. Wachtveitl *Photosynth. Res.* **1998,** *55,* 153.

[131] M. El-Amine Madjet, F. Muh, T. Renger *J. Phys. Chem. B* **2009,** *113,* 12603.

[132] S. Hammes-Schiffer *Acc. Chem. Res.* **2009,** *42,* 1881.

[133] J.A. Potter, P.K. Fyfe, D. Frolov, M.C. Wakeham, R. van Grondelle, B. Robert, M.R. Jones *J. Biol. Chem.* **2005,** *280,* 27155.

[134] I. Muegge, J. Apostolakis, U. Ermler, G. Fritzsch, W. Lubitz, E.W. Knapp *Biochem.* **1996,** *35,* 8359.

[135] J. Apostolakis, I. Muegge, U. Ermler, G. Fritzsch, E.W. Knapp *J. Am. Chem. Soc.* **1996,** *118,* 3743.